

# Spectral analysis and inverse modeling of satellite data and aeromagnetic data

Dissertation

zur Erlangung des akademischen Grades

eines Doktors der Naturwissenschaften (Dr. rer. nat.)

der Mathematisch-Naturwissenschaftlichen Fakultät

der Christian-Albrechts-Universität zu Kiel

vorgelegt von

**Yixiati Dilixiati**

Kiel, September 2021

Institut für Geowissenschaften

Erster Gutachter: Prof. Dr. Jörg Ebbing

Zweiter Gutachter: Dr. Rick Saltus

Tag der mündlichen Prüfung: 06.12.2021

Zum Druck genehmigt: \_\_\_\_\_

Der Dekan

## Declaration

I declare that this thesis has not been previously submitted or accepted for any degree at this or another institution. I hereby certify that this thesis is my own independent work, except where otherwise stated. The German abstract (Zusammenfassung) was translated by Peter Haas. All sources have been acknowledged, and my contribution to the thesis is clearly identified. I certify that the work has been undertaken in compliance with the rules of good academic practice of the German Research Foundation.

## Abstract

A series of Earth observation satellite missions has opened a new era for the study of Earth's magnetic field. Due to the homogeneous global coverage and high accuracy of satellite data, magnetic models derived from those provide reliable estimates of the long-wavelength components of the crustal magnetic field. How such satellite magnetic models can contribute to our understanding of the characteristic of the crustal structures is the main topic of this thesis. First, a comparison of conventional filtering methods was made and a new method for regional spherical harmonic analysis is presented and a thorough discussion is provided by considering the case study of the Australian continent. Next, together with reduction to the pole of satellite data and long-wavelength corrected aeromagnetic compilations, correlated tectonic signatures over the neighboring continents in a Gondwana framework are shown. Finally, a positivity constraint was applied to the global magnetic susceptibility inversion and a globally inverted susceptibility model for a reconstructed Gondwana framework is presented and discussed.

Satellite data and aeromagnetic compilations reflect the same magnetic sources within Earth's crust. Although aeromagnetic surveys provide detailed short-wavelength information, the long-wavelength part of aeromagnetic compilations is not reliable due to the data processing and grid merging techniques. By contrast, satellite data can provide accurate long-wavelength signal on a global scale. To combine these two types of data sets, a new method was developed for regional spherical harmonic analysis. The method uses an equivalent dipole layer and spherical harmonic expansion of dipoles to decompose magnetic data from space domain into spherical harmonic domain. Spectral consistency between a satellite derived magnetic model (LCS-1) and magnetic anomaly compilations of Australia illustrates how satellite data is helpful for providing reliable long-wavelength components.

Magnetic data is acknowledged as a useful tool and broadly used to map multi-scale geological features. In local-scale studies, magnetic anomalies and geological units can often be directly correlated, as the variations of the main field direction can be neglected. However, for regional-scale studies the variations in main field direction should be considered. To remove the dependency of the crustal magnetic field on the main field direction, a two-step technique was used to carry out global reduction to the pole transformation for the satellite derived magnetic model (LCS-1) in a tile-wise manner. As a result, together with long-wavelength corrected regional magnetic data, they allow interpretation of regional tectonic settings, which is illustrated for a Gondwana framework.

Another important aspect of the usage of magnetic data is magnetic susceptibility inversion. Magnetic data alone without inversion can only provide a qualitative knowledge about source location and relative contrast of surrounding geologic bodies. Thus, it is preferable to retrieve the subsurface magnetic properties quantitatively by inversion. However, conventional inversion methods quite often

result in negative susceptibility values, which contradict the positive susceptibilities of iron-bearing minerals, which dominate the magnetic properties of geological materials. Therefore, a non-negative constrained inversion method was adopted to ensure positive susceptibility solutions. Together with a-priori vertical integrated susceptibility model, a global reference susceptibility model is calculated and results are again shown for a Gondwana framework.

## Zusammenfassung

Eine Reihe von Satellitenmissionen der Erdbeobachtung hat eine neue Ära für Untersuchungen des Erdmagnetfelds eingeläutet. Aufgrund ihrer global homogenen Abdeckung und hohen Genauigkeit tragen magnetische Modelle, die aus Satellitendaten abgeleitet werden, zur verlässlichen Bestimmung der langwelligen Komponenten des krustalen Magnetfelds bei. Wie genau solche magnetischen Modelle zum Verständnis von Krustenstrukturen beitragen können, ist Hauptgegenstand dieser Arbeit. Zunächst wurde ein Vergleich von konventionellen Filtermethoden gezogen und eine neue Methode für regionale Kugelflächenfunktionsanalyse präsentiert. Die daraus abgeleiteten Ergebnisse werden anhand einer Fallstudie für den australischen Kontinent gründlich diskutiert. Als nächstes wurden polreduzierte Satellitendaten und langwellig korrigierte aeromagnetische Datensammlungen miteinander korreliert und zusammen mit tektonischen Signaturen in einer Rekonstruktion des Urkontinents Gondwana gezeigt. Schließlich wurde eine globale Inversion der magnetischen Suszeptibilität mit einer Positivitäts-Randbedingung durchgeführt. Die so erhaltenen Suszeptibilitäten werden ebenfalls in einer Rekonstruktion des Gondwana-Urkontinents präsentiert und diskutiert.

Satellitendaten und magnetische Kompilationen spiegeln die gleichen magnetischen Quellen in der Erdkruste wider. Obwohl aeromagnetische Messungen detaillierte Informationen über den kurzwelligen Anteil liefern, ist der langwellige Anteil von aeromagnetischen Kompilationen nur unzureichend bestimmt, was von Datenverarbeitung und dem Fusionieren verschiedener Datenraster hervorgerufen wird. Im Gegensatz dazu können Satellitendaten das langwellige Signal auf globaler Ebene besser abbilden. Um die Charakteristika dieser beiden Datentypen zu kombinieren, wurde eine neue Methode zur regionalen Kugelflächenfunktionsanalyse entwickelt. Diese Methode nutzt einen Equivalent Layer aus Dipolen und eine Kugelflächenfunktionsentwicklung dieser Dipole. Damit werden die magnetischen Daten von der Raum- in die Kugelflächenfunktionsbereich transformiert. Die spektrale Konsistenz von einem auf Satellitendaten basierten magnetischen Modell (LCS-1) und aeromagnetischen Kompilationen von Australien verdeutlicht, dass Satellitendaten zuverlässige langwellige Komponenten liefern.

Magnetische Daten sind nützlich, um heterogene geologische Formationen abzubilden. Für kleinskalige Studien können magnetische Anomalien direkt mit geologischen Einheiten korreliert werden, da hier die Variation der Richtung des Hauptmagnetfelds vernachlässigbar ist. Für regionale Studien müssen diese Variationen jedoch berücksichtigt werden. Damit das Magnetfeld der Kruste unabhängig von der Richtung des Hauptmagnetfelds betrachtet werden kann, wurde eine zweiteilige Technik angewendet. Hierbei wird das satellitenbasierte magnetische Modell LCS-1 in einem tile-wise Ansatz transformiert und polreduziert. Dies ermöglicht zusammen mit langwellig korrigierten

regionalen magnetischen Daten eine Interpretation des regionalen tektonischen Settings, was in einer Rekonstruktion des Urkontinent Gondwana dargestellt wird.

Eine weitere wichtige Anwendung von Magnetikdaten ist die Inversion der magnetischen Suszeptibilität. Ohne das Anwenden von Inversionsmethoden kann anhand von magnetischen Daten lediglich eine qualitative Aussage über die Quellregion und den relativen Kontrast benachbarter geologischer Körper getroffen werden. Inversionsmethoden sind daher von Vorteil, wenn die magnetischen Eigenschaften des Untergrundes quantitativ abgebildet werden sollen. Konventionelle Inversionsmethoden können häufig negative Suszeptibilitäten hervorrufen und stehen damit im Gegensatz zur positiven Suszeptibilität von eisenhaltigen Mineralen, die die magnetischen Eigenschaften von Gesteinen dominieren. Als Lösungsansatz wird in dieser Arbeit eine Inversionsmethode mit nicht-negativer Randbedingung eingeführt, um positive Suszeptibilitäten zu gewährleisten. Zusammen mit einem a priori VIS-Modell wird eine globale Referenzsuszeptibilität berechnet und deren Ergebnisse für eine Rekonstruktion des Urkontinents Gondwana gezeigt.

## Acknowledgements

Let us drink three	ottuz iqip kīkrālīm	أَتْرُ اجِبْ فِقْرَالِيمْ
Let us stand up and shout	yōqar qopup səkrəlīm	يُقَارُ قُبُّ سَكْرَلِيمْ
Let us roar like a lion	arşlanlayu kəkrəlīm	أَرْسَلْنَ لَيُو كُكْرَلِيمْ
Let us rejoice that care has fled from us	qaqtī saqīnq səvnəlim	قَجْتِي سَقْنِجْ سَقْنَلِيمْ

— Mahmud Kashgari, *Turki Tillar Diwani (Compendium of the languages of the Turks)*

Over the past four years I have relied on so many brilliant and generous people. The successful completion of this thesis would not have been possible without your support and assistance. I take this opportunity to express my sincere gratitude to all of you who helped me either morally, financially, and physically.

First and foremost, I would like to express my deepest appreciation to my *Doktorvater* Prof. Dr. Jörg Ebbing who is a wonderful supervisor with great leadership and a level of emotional intelligence in an ever-smiling personality. If you did not bring me into this team, I would have been recording Earth's magnetic field and raising chickens for possible earthquake prediction in a remote village. I am so grateful that you never gave up on me, even when there was zero progress in my PhD project. Thank you so much for providing with me the academic guidance and financial support during this PhD journey.

Next, I would like to thank all the members of the Satellite and Airborne Geophysics group for a pleasant working environment during my time here at CAU. You are always nice and supportive. I feel extremely fortunate to be part of this team and I have learned so much from working with you. Special thanks to Peter Haas, my former officemate, for your hidden expertise of *Zusammenfassung* translation. Thanks should also go to Agnes Wansing, Johanna Lehr, Peter Haas and Ran Issachar for constructive criticism of the thesis.

Writing is painful when your language ability is not well developed to express what you really want to say. Therefore, I would like to acknowledge all the papers I read which provided me the useful hints about scientific writing.

I also wish to thank my parents, my wife and my friends for being caring. Without your love, I wouldn't be the person I am today.

Finally, I would like to thank myself for hardworking when it was not gratifying, I would like to thank myself for believing in me when there was no guaranty, I would like to thank myself for not giving up when things get tough.

# Contents

Declaration .....	ii
Abstract .....	iii
Zusammenfassung.....	v
Acknowledgements.....	vii
Chapter 1 Introduction.....	1
1.1. Background.....	1
1.2. Scientific problems and Motivations.....	3
1.3. Thesis structure .....	4
1.4. Author contributions .....	5
Chapter 2 .....	6
2.1. Introduction.....	6
2.2. Filtering methods .....	7
2.2.1. Spherical Harmonics.....	7
2.2.2. Slepian functions .....	8
2.2.3. Fourier domain filtering.....	9
2.3. Results .....	11
2.3.1. SH filtering compared to Fourier domain filtering .....	11
2.3.2. SH filtering compared to Slepian filtering .....	14
2.3.3. Slepian filtering compared to Fourier domain filtering.....	19
2.3.4. Comparison of the three filtering approaches .....	20
2.4. Conclusions.....	21
Chapter 3 Paper I.....	23
3.1. Introduction.....	23
3.2. Magnetic Models and Aeromagnetic Data.....	25
3.3. Methods .....	27
3.3.1. Inversion of the equivalent dipole layer.....	27
3.3.2. Spectral representation of a dipole field.....	28
3.4. Results .....	29

3.4.1.	Regional SH reconstruction of the data from the magnetic models.....	29
3.4.2.	Power spectrum of data sets of Australia .....	33
3.5.	Discussion .....	37
3.6.	Conclusion .....	38
Chapter 4	.....	39
4.1.	Introduction.....	39
4.2.	Methods .....	40
4.3.	Results .....	41
4.3.1.	Test inversion for local area .....	41
4.3.2.	Global tile-wise inversion .....	44
4.4.	Conclusion .....	52
Chapter 5	Paper II.....	54
5.1.	Introduction.....	54
5.2.	Conforming satellite magnetic and aeromagnetic data.....	56
5.3.	Discussion .....	61
5.4.	Conclusions.....	62
5.5.	Data and Methods.....	63
5.6.	Conforming aeromagnetic compilation to satellite model .....	66
5.7.	Data Availability.....	67
5.8.	Plate-tectonic illustrations .....	67
5.9.	Acknowledgements .....	67
5.10.	Author Contributions.....	67
Chapter 6	Paper III.....	68
6.1.	Introduction.....	68
6.2.	Methodology .....	70
6.2.1.	Tesseroid Forward Field .....	70
6.2.2.	Spherical Harmonic Model .....	71
6.2.3.	Projected Gradient Inversion .....	71
6.3.	Data .....	72

6.3.1.	Model Geometry .....	72
6.3.2.	Magnetization Direction and Susceptibility .....	73
6.3.3.	Lithospheric Magnetic Field Models .....	74
6.4.	Results .....	76
6.4.1.	Synthetic Test .....	76
6.4.2.	Inversion of LCS-1 .....	78
6.5.	Discussion .....	79
6.5.1.	Performance of Inversion .....	79
6.5.2.	Use of a-Priori Model .....	79
6.5.3.	Layering of the Model .....	81
6.5.4.	Regularization.....	81
6.5.5.	Application to Airborne Data—Proof of Concept.....	81
6.6.	Conclusions.....	82
Chapter 7	.....	84
7.1.	Introduction.....	84
7.2.	Data and Methods.....	85
7.3.	Results .....	86
7.4.	Discussion .....	91
7.5.	Conclusions.....	93
Chapter 8	Conclusions and Outlook.....	94
8.1.	Summary.....	94
8.2.	Possible future tasks.....	96
Appendix	.....	97
Appendix I	.....	97
Appendix II	.....	100
References	.....	104

# Chapter 1 Introduction

## 1.1. Background

The Earth's magnetic field consists of internal and external fields. The external field is due to the interaction between the internal field and the activity of the Sun. The internal field is dominated by the core field which is generated in the liquid core by the geodynamo process (Roberts and Glatzmaier 2000). In addition to the core field, the main contribution to the internal field comes from the Earth's crust.

Magnetic methods have become important tools for inferring the magnetization of the crust related to subsurface geology, and aiding to locate the natural resources and exploring the geodynamo process (Roberts and Glatzmaier 2000; Nabighian et al. 2005). Therefore, a large amount of magnetic data has been collected for investigating the inner structure of the solid Earth from the crust to the core. Nowadays, such data sets are available from both satellite and terrestrial or near surface measurements. Near-surface and satellite magnetic data are widely used to study the crustal structures or even to estimate the Curie isotherm (e.g. Briais et al. 1993; Searle et al. 1998; Li et al. 2017; Ferre et al. 2014; Núñez Demarco et al. 2021). Near-surface data are more sensitive to the small-scale structures and dominated by short-wavelengths of the magnetic field as they are acquired close to the sources. Due to the greater attenuation of the shorter wavelengths with respect to the observation height, satellite data are dominated by long wavelength components of magnetic response of the sources.

The number of near-surface magnetic surveys, airborne and shipborne, has grown rapidly since the 1930s, both for mineral exploration and military applications (Heiland 1942; Fromm 1952). Continuous improvement in magnetic instrumentation formed an era of high activity in exploration and mapping surface geology (Reford and Sumner 1964; Paterson and Reeves 1985). The implementation of GPS as location reference for aeromagnetic surveys significantly improved the location accuracy compared to more complicated and costly pre-GPS positioning systems (Brozena et al. 1989). The availability of GPS and magnetometers with high sensitivity and accuracy enabled the development of high-resolution aeromagnetic survey systems. Because of this technical evolution, low-altitude magnetic surveys became a cost-effective tool for exploration.

Many national and multinational initiatives have compiled systematic aeromagnetic surveys for large areas of the Earth (e.g. Australia, South Africa, Arctic and Antarctic area) as an aid to both surface geological mapping and magnetic mineral exploration (e.g. Milligan and Nakamura 2015; Stettler et al. 2000; Gaina et al. 2011; Golynsky et al. 2018).

The development of new technologies together with satellite missions has opened a new phase in magnetic measurements from space. Airborne compilations are nowadays complemented by satellite measurements, that offer the advantage of global coverage. Measurements of the Earth's magnetic field from space began about 50 years ago. The first global scale magnetic model was derived from the *POGO* satellite mission (1965-1971) which measured the scalar magnetic data and provided crustal magnetic field models up to spherical harmonic (SH) degree 30 ([Cain and Sweeney 1973](#); [Langel 1990](#); [Stockmann et al. 2015](#)). The *POGO* mission consisted of three satellites, *OGO-2*, *OGO-4* and *OGO-6*, which orbited at altitudes from 400-1510 km. That was followed by the *MAGSAT* satellite mission that lasted for a period of eight months from September 1979 to June 1980. The orbit was initially at 352 km perigee and 561 km apogee which decayed to a more circular orbit of 400 km at the end. The *MAGSAT* satellite itself was equipped with the first vector magnetometer in space and with the measurements the crustal magnetic field up to SH degree 63 could be estimated ([Cain et al. 1989](#)).

The launch of the satellites *Ørsted* and *CHAMP*, which were equipped with more sensitive scalar and vector magnetometers, increased the spatial resolution of the crustal magnetic field to 333 km corresponding to SH degree 120 ([Maus et al. 2008](#)). *Ørsted* was launched in February 1999 into a near polar orbit with perigee at 649 km and apogee at 865 km ([Neubert et al. 2001](#)). Although it was still on orbit, the *Ørsted* mission was halted in 2014 ([Sabaka et al. 2020](#)). As a second-generation magnetic satellite, its instrumentation became a general model for later missions. Following closely behind the *Ørsted* launch, the *CHAMP* satellite was launched in July 2000 into a near polar orbit with an initial altitude of 454 km which decayed to 300 km during a full decade life-span ([Kunagu et al. 2013](#)). Due to the good condition of the satellite, the original 5-year mission was extended to ten years and made it the most productive magnetic satellite mission until the ongoing Swarm satellite mission.

In late 2013, the *Swarm* satellite mission was launched by European Space Agency (ESA). The mission consists of three identical satellites, with two of them, Swarm Alpha and Swarm Charlie, at an initial altitude of 462 km flying side by side to measure the East-West gradient and together with the third satellite Swarm Bravo providing North-South gradient data at a higher orbit of 511 km.

A satellite-only magnetic model, the global lithospheric field model LCS-1 (Lithospheric model derived from *CHAMP* and *Swarm* satellite data, **version 1**) was released in 2017 ([Olsen et al. 2017](#)). The *Swarm* satellite constellation provides gradient information of the magnetic field which helps suppressing unwanted contributions from the external magnetic field sources and the core field, in order to enhance the crustal signal. As a result, LCS-1 provides spherical harmonic coefficients up to degree 185 corresponding to the horizontal resolution down to ~220 km which is a significant improvement to previous global crustal models even though the quality of the higher degree coefficients is doubtful.

Combining satellite and near-surface data, the Digital Magnetic Anomaly Map of the World (WDMAM) is the results from an international effort to build a high-resolution global magnetic model. Since new data sets had been available, the new version of WDMAM was updated. The new magnetic compilation map was derived from more than 50 years of aeromagnetic and shipborne surveys, observations from earth-orbiting satellites, supplemented by anomaly values derived from oceanic crustal ages ([Lesur et al. 2016](#)). Marine and continental data sets were handled in different strategies due to the sparse data coverage over the oceanic areas compared to the continental areas. A sophisticated forward model was developed to provide magnetic anomalies caused by seafloor spreading. As a result, this model was used to fill the data gap over the oceanic areas. In the data processing of the continental part, individual data sets were merged through the overlapping boundaries using weighted average to ensure a smooth transition between adjacent boundaries ([Hamoudi et al. 2007](#)). Finally, the long-wavelengths of the magnetic model were constrained by the GRIMM\_L120 satellite model and an iterative inversion method with regularization parameters was used to derive spherical harmonic coefficients of the model (for details see [Lesur et al. 2016](#)).

## 1.2. Scientific problems and Motivations

To investigate the distribution of the crustal magnetic sources and interpret geological features, reliable magnetic signals of the crust are required both for long- and short-wavelengths. Despite the recent discussion whether the upper mantle can be magnetic too, I regard the base of the crust as lower boundary for magnetization in this thesis.

Due to the global coverage and continuous data collection in space domain, the satellite models are considered as a reference for the long-wavelength portion of the magnetic crust. In addition, near-surface data can provide detailed information of the magnetic crust because they are close to the magnetic sources. Qualitatively speaking, however, the long-wavelength part of the near-surface data is problematic. It is obvious that a single path of magnetic survey cannot reveal the long-wavelength signals which are greater than its survey dimension. In practice, a number of individual surveys are merged together into a large-scale magnetic compilation. However, the long-wavelength component of a magnetic compilation is usually distorted. The reason for this issue is twofold: the systematic inconsistency of measured data (different instruments, positioning error) and processed data (different reference main field, insufficient diurnal correction, levelling, continuation to same height) between individual surveys, which result in discontinuous transition between grid boundaries. To have a continuous grid boundary, grids are stitched together through overlapping boundaries by using some smoothing algorithms. As a result, the short-wavelengths of the compilation are quite consistent but still leave the long-wavelength components uncorrected. Therefore, question 1 arises as to whether, and to what extent, the long-wavelength components of a magnetic compilation can be improved.

- *Q1: Since the satellite data/models can provide a reference for reliable long-wavelength component of the crustal magnetic field, how can we make use of them to analyze and improve the long-wavelength part of the aeromagnetic compilations?*

There is a large amount of observations from geology, geoscience and paleontology supporting the concept of plate tectonics. Furthermore, it would be of great interest to scientists to know how the present-day continents are linked together at geological time-scale. As an important geophysical tool, magnetic data can reflect large-scale geological features which might have “survived” during millions of years of geological processes. Therefore, question 2 arises as

- *Q2: Since the satellite data/models can provide a global-scale coverage of magnetic data, how can the present-day data help us to link the continents at geological time-scale?*

Although the magnetic crustal field correlates with the magnetic source distribution, it is the joint effect of inducing field (Earth’s core field) and magnetic susceptibility. Only the magnetic susceptibility directly reflects the physical property of the crustal layer. Therefore, magnetic inversion is required to derive the magnetic susceptibility from the magnetic crustal field. Lastly, question 3 arises as

- *Q3: How can we derive a meaningful magnetic susceptibility distribution of the crust from the satellite data/models?*

### 1.3. Thesis structure

The content of this thesis can be categorized into two parts, data processing and magnetic inversion, which is illustrated in the flow chart below.

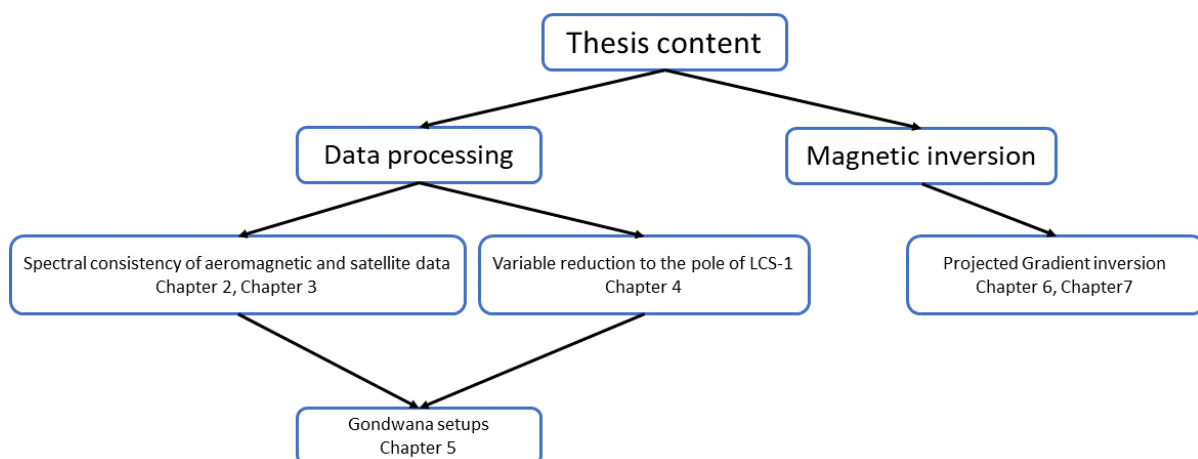


Figure 1.1: Thesis Flow Chart

- *Chapter 2:* is dedicated to comparison of three filtering methods (Fourier domain, Slepian and spherical harmonic) for spectral consistency between filtered data and input synthetic magnetic model which combines the WDMAM model and a statistical power spectrum model in regional area. Classical Fourier domain and Slepian filtering methods fail to extract same spectral

information with respect to the SH filtering method. This result motivates me to develop a new method for regional SH filtering.

- *Chapter 3*: describes a new method for decomposing the magnetic signals into SH domain in regional area. The method is validated by two magnetic models (LCS-1 and WDMAM) and applied to three consecutive editions of the Magnetic Anomaly Map of Australia to analyze the spectral consistency between LCS-1 satellite model.
- *Chapter 4*: presents a result of variable reduction to the pole of the LCS-1 model, which removes the crustal field's dependency on variable main field direction.
- *Chapter 5*: provides a new insight on links between Antarctica and its neighbors within the Gondwana framework via magnetic data which are processed using the methods described in previous two chapters.
- *Chapter 6*: shows the susceptibility inversion of LCS-1 model in 2-degree resolution using tesseroids for forward calculation and Projected Gradient method for inversion.
- *Chapter 7*: adopts a similar strategy like the previous chapter but increases the resolution to 1-degree in an equidistant manner. The inversion results focus on Australia, Antarctica and Southern Africa to maintain consistency with chapter 5.
- *Chapter 8*: summarizes the main conclusions of this thesis and outlines some possible future studies.

#### 1.4. Author contributions

There are three already published or submitted papers included in the thesis.

**Paper I:** *"Spectral consistency of satellite and airborne data: Application of an Equivalent dipole layer for combining satellite and aeromagnetic data sets"*

is included in chapter 3. This paper has been submitted to *Geophysics*. I developed the method and did all the calculations and analysis. I compiled the initial version of the manuscript. All authors discussed the results and contributed to the submitted manuscript.

**Paper II:** *"East Antarctica magnetically linked to its ancient neighbours in Gondwana"*

is included in chapter 5. This paper has been published in *Scientific Reports 11, 5513 (2021)*; <https://doi.org/10.1038/s41598-021-84834-1>. I fully developed the data processing and contributed to the final version of the manuscript.

**Paper III:** *"Global high-resolution magnetic field inversion using spherical harmonic representation of tesseroids as individual sources"*

is included in chapter 6. This paper has been published in *Geosciences, 10(4), 147*; <https://doi.org/10.3390/geosciences10040147>. I tested and validated the inversion method used in this paper. I wrote the methodology of the inversion part in this paper.

## Chapter 2

# Spectral consistency of satellite and airborne data: Comparison of classical filtering methods

### 2.1. Introduction

Short and long-wavelength components of the crustal magnetic field are generally associated with shallow and deep magnetic sources, respectively. However, long wavelength anomalies (>200 km wavelength) that reflect the deep magnetic sources in the lower crust and upper mantle are not measured sufficiently by near surface datasets (Pilkington and Roest 1996; Tarlowski et al. 1996; Ravat et al. 2003; Minty et al. 2003; Ravat and Korhonen 2010). Firstly, the size of an aeromagnetic survey prohibits measuring wavelength larger than its extent. A typical large-scale aeromagnetic survey has a size of about 300 x 300 km only, with a line spacing down to 100 m (Percival 2013). Secondly, merging individual datasets of adjacent areas often introduces unreliable or distorted long wavelength components. Large magnetic grids are a patchwork of different surveys that are conducted in different years and might have different survey heights, resolutions and dimensions. Accordingly, significant disagreement across the boundary and/or overlapping areas can be detected because of inconsistency between survey heights and tilts. To minimize the differences, merging techniques often employ a weighted average of different-order polynomial surfaces to merge the nearby surveys to a continuous grid (Hemant et al. 2007). As a result, the long-wavelengths are not mapped consistently over individual surveys and long wavelength distortions are unavoidable.

For applications like estimating the Curie isotherm, the intermediate to long-wavelength range is of particular interest. Thus, there is a practical need for correcting long wavelength distortion of the aeromagnetic data, although it is a challenging task.

In theory, near surface and satellite data should contain the identical long-wavelength components over a same specific region since both data are attributed to the same crustal anomaly sources. However, due to the long wavelength distortion caused by data processing of near surface data, the spectral consistency between satellite and near surface data cannot be guaranteed. In this case, satellite data might provide the undistorted long-wavelength components. Nowadays, using satellite data to improve the long-wavelength components of near surface magnetic data is a common routine. The essence of the spectral consistency is to project two signals to the same basis functions to analyze whether the “coordinates” on same basis functions or “axes” are comparable. In other words, if two signals can be decomposed into same basis functions, the spectral components can be directly compared as a set of coefficients of basis functions. In our case, the two signals are magnetic anomaly data at different height.

To analyze the spectral consistency, the conventional approach to merge satellite and near surface data is combining spherical harmonic filtering and Fourier filtering (e.g. [Maus et al. 2009](#); [Gaina et al. 2011](#)). Thereby, the satellite data is expanded in spherical harmonics (SH) to degree  $n$  which represents the long wavelength part of the crustal anomalies. Fourier low pass filtering is applied to the near surface data filtering out the short wavelengths to get the same spectral components associated with degree  $n$ . Then, the low pass filtered near surface data is substituted with its satellite counterpart.

However, the two filtering approaches perform in two different spectral spaces. SH is defined in the basis function of the spherical harmonics  $Y$ , while Fourier representation uses sine-cosine waves. As a rule of thumb, signals represented in SH basis and Fourier basis are not consistent. Consequently, the actual filtered results do not reflect the same spectral range because of using different basis functions.

SH, as the solution of Laplace equation, are the most powerful tool to analysis the spectral components of the magnetic data. But its orthogonality restricts its application to regional area so that regional data cannot be reconstructed in SH basis functions.

Slepian functions perform like spherical harmonics globally and are also locally orthogonal ([Simons and Dahlen 2006](#)). In this regard, it might be a promising tool for spectral consistency analysis to compare consistent long wavelength components of satellite and near surface data sets.

For consistent merging of satellite and near surface magnetic data, three spectral filtering methods which are SH filtering, FFT filtering and Slepian filtering over Australia were tested, where high-resolution magnetic data are available. The spectral consistency of different methods was demonstrated using both synthetic and real data sets.

## 2.2. Filtering methods

### 2.2.1. Spherical Harmonics

The Spherical Harmonic (SH) expansion is well-known and a common approach for analyzing potential field data. The global magnetic potential field  $V$  is expanded in spherical harmonics, and the vector components of the magnetic field  $\vec{T}$  can be calculated using its gradient, which are expressed as

$$V(\varphi, \theta, r) = a \sum_{n=1}^{\infty} \sum_{m=0}^n \left(\frac{a}{r}\right)^{n+1} [g_n^m \cos(m\varphi) + h_n^m \sin(m\varphi)] S_n^m(\cos \theta) \quad (2.1)$$

$$\vec{T} = -\nabla V$$

where  $a$  is the radius of the Earth,  $r$  is the radial distance of the observation point from the center of the earth,  $\varphi$  denotes longitude and  $\theta$  colatitude respectively;  $S_n^m$  the Schmidt quasi-normalized associated Legendre functions of degree  $n$  and order  $m$  together with Gauss coefficients  $g_n^m$ ,  $h_n^m$  determine the potential field.

SH are perfectly localized in the frequency domain but their spatial energy is geographically distributed over the entire globe (global supported function). Information about the field contained in a single spherical-harmonic coefficient is ultimately derived from a signal that would not originate from a single location (Sneeuw and van Gelderen 1997). In other words, spherical harmonics are well suited for the representation and analysis of magnetic fields globally, but fail to analyze local nature of the geological sources.

To analyze regional data, several methods have been developed to model regional signals, such as harmonic splines, Rectangular Harmonic Analysis (RHA), Spherical Harmonic Cap Analysis (SHCA) and Revised Spherical Cap Harmonic Analysis (R-SCHA) (Allredge 1981; Haines 1985; E. Thébaud et al. 2006). Each method has advantages over global SH analysis for local regions. However, none of the above techniques attempts to recover the magnetic fields over arbitrary regions. In this respect, the approach by Slepian functions is unique and suited for the problem of representing the magnetic data that arise from distinct geographic regions (Simons et al. 2006).

### 2.2.2. Slepian functions

The Slepian method originated from the polar gap problem, which is an antipodal pair of axisymmetric polar caps without any data coverage (Simons and Dahlen 2006). Slepian functions have been designed as a particular linear combination of spherical harmonics, which are not only orthogonal over the entire sphere, but also orthogonal over the specific area. Slepian functions  $G$  are weighted sum of spherical harmonics  $Y$  (Simons et al. 2006).

$$G(\vec{r}) = \sum_{n=0}^N \sum_{m=-n}^n g_{nm} Y_{nm}(\vec{r}) = \mathbf{y}^T \mathbf{g} \quad (2.2)$$

To calculate the weighting coefficients  $g_{nm}$ , Slepian functions maximize their spatial energy over a certain spatial region of interest, preserving orthogonality over the entire sphere  $\Omega$  as well as over the chosen spatial domain  $R$ .

$$\lambda = \max_{\mathbf{g}} \frac{\int_R G^2(\vec{r}) d\Omega}{\int_{\Omega} G^2(\vec{r}) d\Omega} = \max_{\mathbf{g}} \frac{\mathbf{g}^T \mathbf{D} \mathbf{g}}{\mathbf{g}^T \mathbf{g}} \quad (2.3)$$

$$\mathbf{D} = \int_R \mathbf{y} \mathbf{y}^T d\Omega$$

The stationary solutions of maximum energy  $\lambda$  are the eigenvectors  $g_1 \dots g_{\alpha} \dots g_{(N+1)^2}$  that constitute an orthogonal coefficient matrix

$$\mathbf{G} = (g_1 \dots g_{\alpha} \dots g_{(N+1)^2}), \mathbf{G}^T \mathbf{G} = \mathbf{G} \mathbf{G}^T = \mathbf{I} \quad (2.4)$$

defined by the eigenvalue problem

$$DG = G \Lambda \quad (2.5)$$

Each eigenvalue  $\lambda_\alpha$  represents the amount of energy over the regional area  $R$  compared to the surface  $\Omega$  of the entire sphere. The potential function can be represented by the Slepian-function coefficients  $s_\alpha$ .

$$V(\vec{r}) = \sum_{n=0}^N \sum_{m=-n}^n u_{nm} Y_{nm}(\vec{r}) = y^T u = y^T G G^T u = \sum_{\alpha=1}^{(N+1)^2} s_\alpha G_\alpha(\vec{r}) \quad (2.6)$$

The Slepian functions allow for a constructive approximation of bandlimited function  $V$ , locally within the target region  $R$ , by restricting the expansion above to the  $k$  best-concentrated Slepian functions. The greater the number of terms  $k$ , the less well localized the approximation, but the smaller the approximation error (generally selecting eigenvalue  $\lambda_k = 0.5$ , [Simons et al. 2006](#)).

$$V(\vec{r}) \approx y^T G_k G_k^T u = \sum_{\alpha=1}^k s_\alpha G_\alpha(\vec{r}) \quad (2.7)$$

The new basis functions  $G_\alpha$  vanish approximately outside the chosen geographical boundaries but also remain orthogonal within the spatial region of interest  $R$ . Both near surface and satellite data can be expanded in terms of Slepian functions in the same region of interest  $R$ . As a result, one can extract the long wavelength portion of the data from a merged data set and compare it to the satellite data in order to replace the long wavelength counterpart.

### 2.2.3. Fourier domain filtering

Fourier domain analysis is a widely used methodology in the frequency-domain (spectral analysis). The signal is represented by a series of sinusoids of different frequencies. Theoretically, any spatial signal may be expressed as a weighted linear sum of harmonics (sine and cosine functions) having infinity frequency components so that Fourier transformation represents the signal as a series of sine and cosine waves of different amplitude and phase.

$$f(x) = \sum_{n=0}^{\infty} (a_n \cos k_n x + b_n \sin k_n x) \quad (2.8)$$

Although it is a common tool for combining satellite and near surface data sets, there are pitfalls that one can hardly avoid. (1) By definition, Fourier domain analysis is the decomposition of a 2D signal into plane waves. Therefore, signals measured on a spherical surface in a small area can be simplified as a plane geometry and the Fourier domain analysis can be utilized. However, for continental scale applications, such simplification is problematic due to the sphericity of the earth surface. (2) It is not possible to extract ideally consistent long-wavelength components from satellite and near surface data

because Fourier filtered results always suffer from the spectral leakage effect where the maximum bandwidth of the signal is greater than the maximum degree of the basis functions.

A simple 1-D case can illustrate this problem. Consider a set of observations at a spherical surface ( $r_0 = a/r$ ) along with the same colatitude ( $\theta = \theta_0$ ). The radial component of the potential  $V$  can be expressed as a function of longitude  $\varphi$  in the form of harmonic expansion,

$$T_r(\varphi) = \sum_{n=1}^{\infty} \sum_{m=0}^n (n+1)r_0^{n+2} [g_n^m \cos(m\varphi) + h_n^m \sin(m\varphi)] S_n^m(\cos \theta_0) \quad (2.9)$$

Reordering the terms in equation (2.9) leads to

$$\begin{aligned} T_r(\varphi) &= \sum_{m=0}^{\infty} G_n^m \cos(m\varphi) + H_n^m \sin(m\varphi) \\ G_n^m &= \sum_{n=1}^{\infty} (n+1)r_0^{n+2} P_n^m(\cos \theta_0) g_n^m \\ H_n^m &= \sum_{n=1}^{\infty} (n+1)r_0^{n+2} P_n^m(\cos \theta_0) h_n^m \end{aligned} \quad (2.10)$$

Equation (2.10) is in the same form of the Fourier series expansion. Generally, the highest horizontal spatial resolution  $\lambda$  (in km) in data associated with the highest SH degree  $n$  (Thébault et al. 2010), which is

$$\lambda = \frac{2\pi a}{\sqrt{n(n+1)}} \approx \frac{2\pi a}{n} \quad (2.11)$$

Considering the satellite model with SH up to degree 140, a low pass Fourier filter is applied to the satellite data which are expanded to its full spectrum range to filter out spatial wavelength shorter than 400 km which is corresponding to SH degree 100 according to equation (2.11). As a result, Fourier filtering filters out spectral components  $G_n^m$  and  $H_n^m$  of  $T_r(\varphi)$  whose order  $m$  greater than 100. However,  $G_n^m$  and  $H_n^m$  degree  $n$  less than 100 and order  $m$  greater than 100 still remain unfiltered so that low degree SH components still can appear in the Fourier filtered result.

Figure 2.1 demonstrates the spectral leakage of Fourier filtering for the simple 1-D case. Spherical filtering provides the information about degrees and orders smaller than 100 (triangle in the diagram). However, Fourier domain filtering involves the SH coefficients in which the orders are smaller than 100 (triangle plus rectangular). As shown in equation(2.10), the amplitudes  $G_n^m$  and  $H_n^m$  of the certain frequency (certain order  $m$ ) consist of infinitely weighted linear combinations of SH coefficients from degree  $n = 1 - \infty$ . Consequently, it leads to high frequency information of degree  $n$  greater than 100

mapping into the filtered result (in this case, degree  $n = 101 - 140$  order  $-100 \leq m \leq 100$  rectangular area).

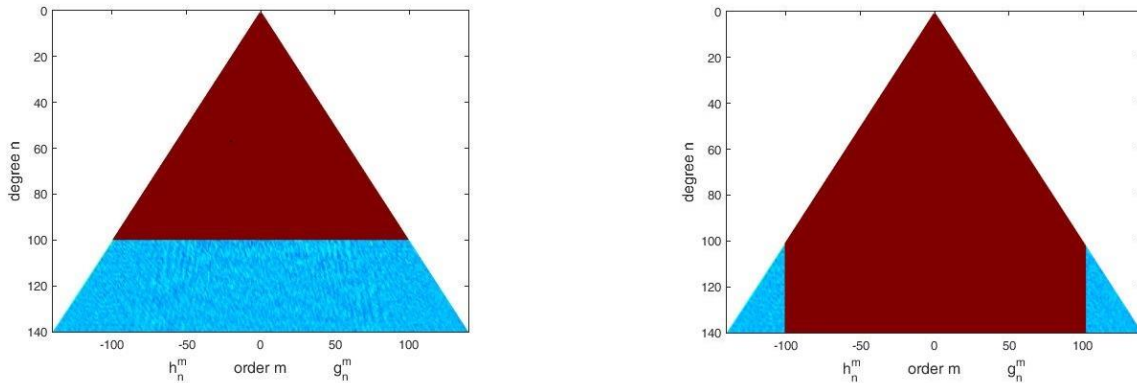


Figure 2.1: Schematic sketch of SH and FFT filtering: (Left) red area represents the components in SH filtered data. (Right) red area represents the components in FFT low pass filtered data (cut-off wavelength 400 km corresponding to SH degree 100).

## 2.3. Results

Since satellite-only magnetic models can provide SH spectral resolution up to degree and order 185 ([Olsen et al. 2017](#)), the short-wavelength information in aeromagnetic data is not covered by satellite-only model. To mimic the broad-band spectrum of the aeromagnetic data, the WDMAM model (SH degree up to 720) is combined with synthetic SH coefficients which were expanded in the range of SH degree 721-5000. The synthetic SH coefficients were randomly generated according to a statistically meaningful power spectrum which follows a power law ([Thébault and Vervelidou 2015](#)). Statistical parameters were chosen similarly to the previous paper, which were  $m = 0.7 A/m$ ,  $\gamma = 1.3$ ,  $\varepsilon = 33$  km. The SH coefficients from the WDMAM model together with statistical power spectrum method were expanded to SH degree 500,1000,2000,3000,4000 and 5000 in 0.1-degree resolution over mainland Australia as input data.

### 2.3.1. SH filtering compared to Fourier domain filtering

According to the relation between SH degree and spatial resolution, SH degree 100 corresponds to 400 km horizontal resolution. A Butterworth low pass filter (cut-off wavelength 400 km) was applied to these synthetic data to extract long wavelength less than degree 100.

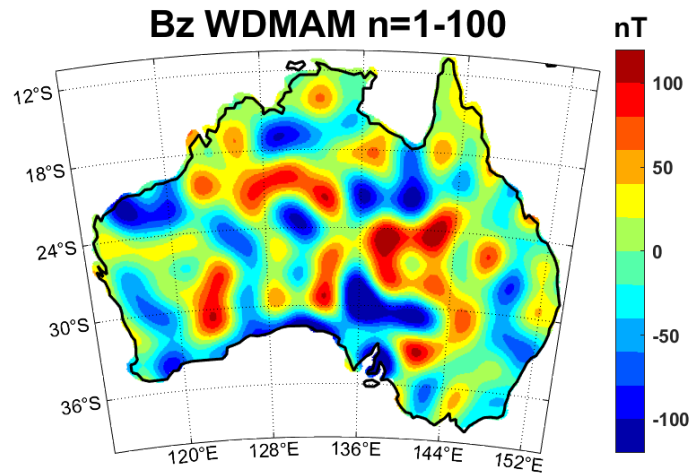


Figure 2.2: Calculated vertical component Bz from WDMAM model SH degree 1-100 at surface

If SH filtering and Fourier filtering were identical, low pass filtering (cut-off wavelength 400 km) would provide the same long wavelength information as SH representation of degree up to 100 (Figure 2.2). As illustrated below (Figure 2.4, Figure 2.5), the low pass filtered results show remarkably similar patterns compared to SH representation. The difference between the FFT filtered result and SH degree 100 representation presents spot-like structures, because the signals beyond the degree 100 are mapped into the low pass filtered result as a high frequency noise. While the high frequency distortion does not change the main patterns, the difference is not negligible, locally even beyond  $\pm 100$  nT.

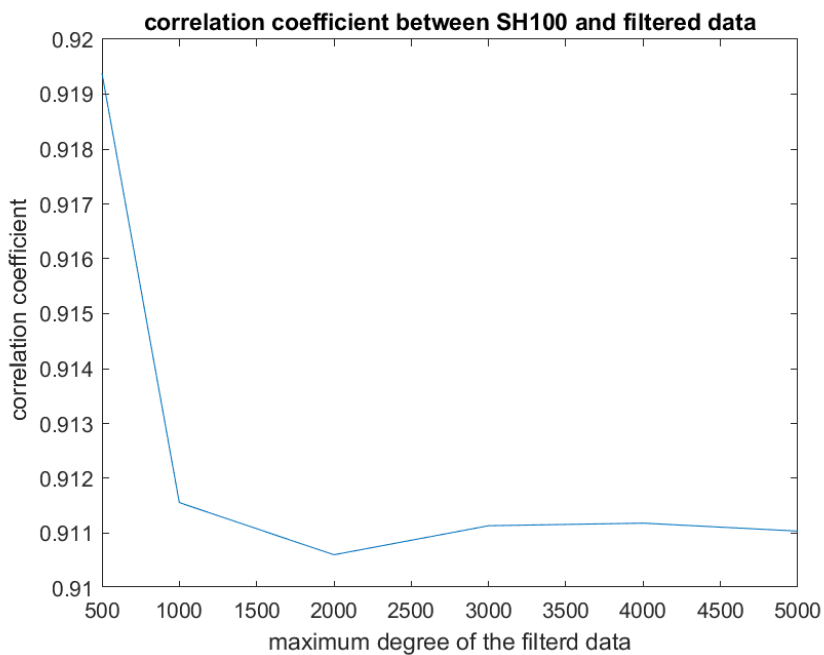


Figure 2.3: Correlation coefficients between filtered data and SH100

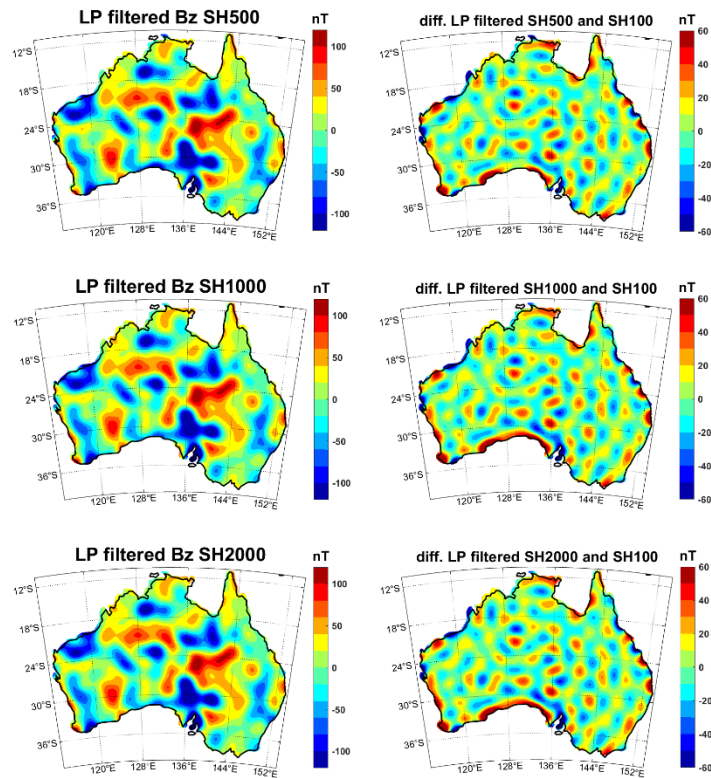


Figure 2.4: Low pass filtered synthetic data (expanded to different SH degree) with cut-off wavelength of 400 km and its difference between Figure 2.2 I

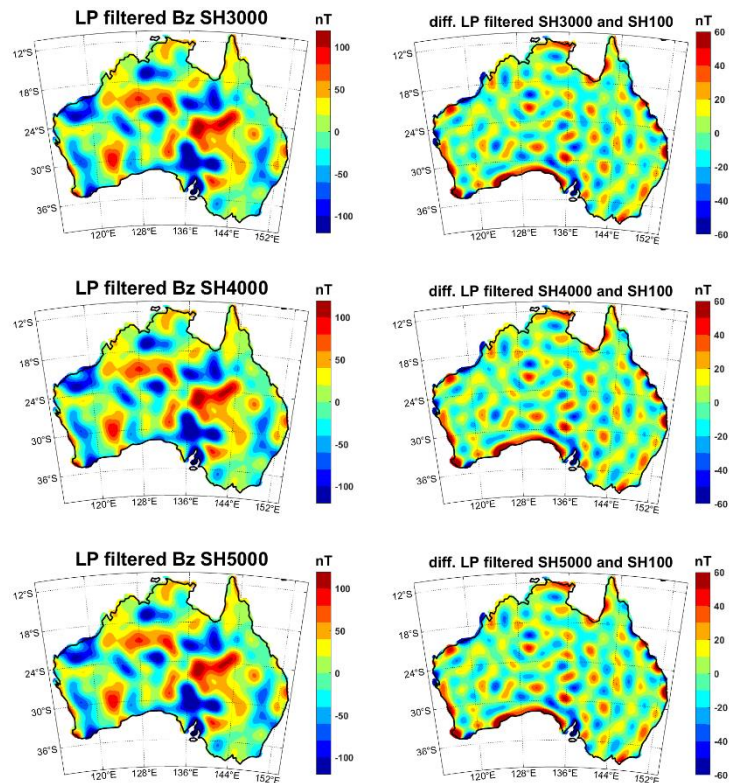


Figure 2.5: Low pass filtered synthetic data (expanded to different SH degree) with cut-off wavelength of 400 km and its difference between Figure 2.2 II

When more high frequency signal is included in the analysis, the low pass filtered results did not change significantly. Figure 2.3 shows that the correlation coefficients between low pass filtered data and SH100 representation level off after SH degree 1000, which also can be seen from the difference map that the difference was almost identical after SH degree 1000. It may imply that FFT filtering applied to real full spectrum aeromagnetic data still can extract its similarly shaped long-wavelength patterns with spot-like high frequency 'noise' which is due to the spectral leakage from the spectral information beyond the cut-off wavelength.

### 2.3.2. SH filtering compared to Slepian filtering

In this section, a similar practice was carried out to extract the first 100-degree SH components from the synthetic SH coefficients that was expanded to degree 500,1000,2000...5000, respectively.

First degree 100 Slepian base functions were evaluated according to SH degree 100 basis functions over Australia at surface height. Eigenvalues of the Slepian basis functions show that only about 300 out of 10200 basis functions have sufficient large degree of concentration in the target area. On the contrary, the contribution of the other 9900 Slepian base functions is nearly zero.

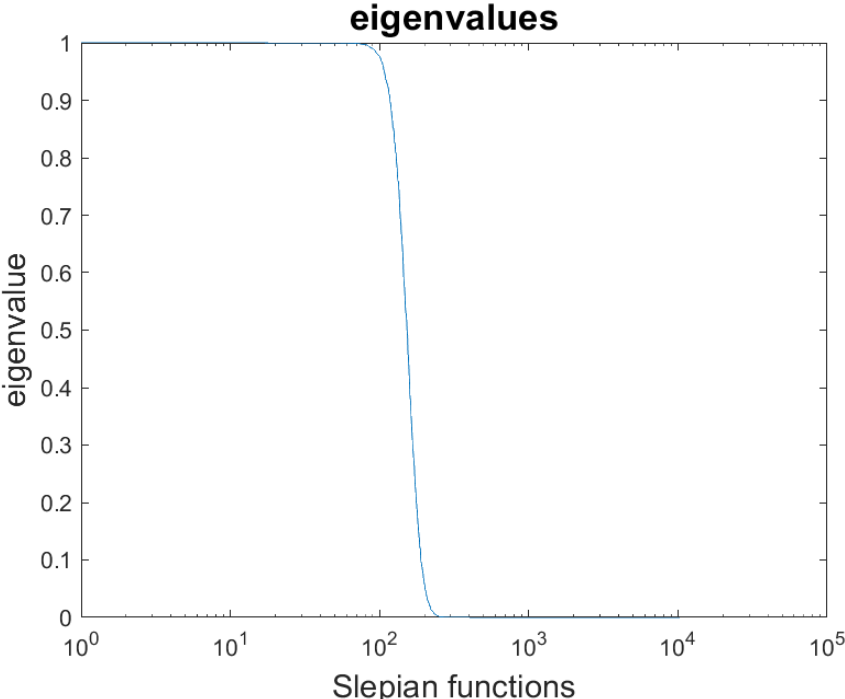


Figure 2.6: Special concentration of Slepian functions in Australia

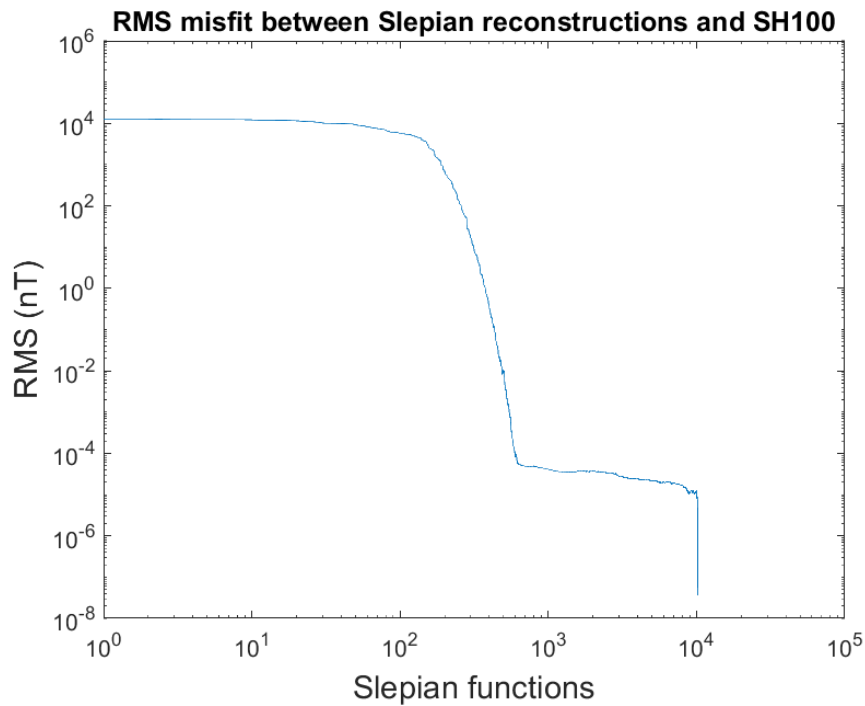


Figure 2.7: RMS misfit between Slepian reconstruction of SH1-100 signal and SH1-100

The signal calculated from SH degree 1-100 was reconstructed using these Slepian basis functions and the RMS difference was calculated to illustrate abovementioned special concentration features of the Slepian basis functions. As shown in Figure 2.7, with the increase in the number of Slepian basis functions used, the RMS difference rapidly converges to zero. The RMS values for the first 300 and 400 Slepian functions are 0.1 and 0.01 nT, respectively. This suggests that the signal that is calculated from SH coefficients of 10200 (up to SH degree 100) can be reconstructed precisely just using less amount of Slepian coefficients (e.g. just 3%).

However, if the maximum SH degree of the signal is not equivalent to Slepian basis functions', Slepian basis functions corresponding to SH degree 100 in this case, the signal cannot be recovered precisely as mentioned above. By using Slepian functions up to degree 100 as a low pass filter, we cannot precisely extract SH degree 1-100 from the synthetic data. High frequency components beyond SH degree 100 would be mapped into the filtered result.

To verify this, synthetic data calculated from SH degree 1-500, 1-1000, 1-2000..., 1-5000 were used as input data to filter out SH degree 1-100 signal using first 300 Slepian basis functions. Filtered results (Figure 2.8, Figure 2.9) are almost identical but the difference between signal from SH degree 1-100 is quite severe compared to the FFT filtered results. These results show that Slepian functions are only suitable to reconstruct signals for which the band limit is known. When signal's bandwidth is greater than Slepian functions' bandwidth, using Slepian functions as a low pass filter will map high frequency information into the filtered data.

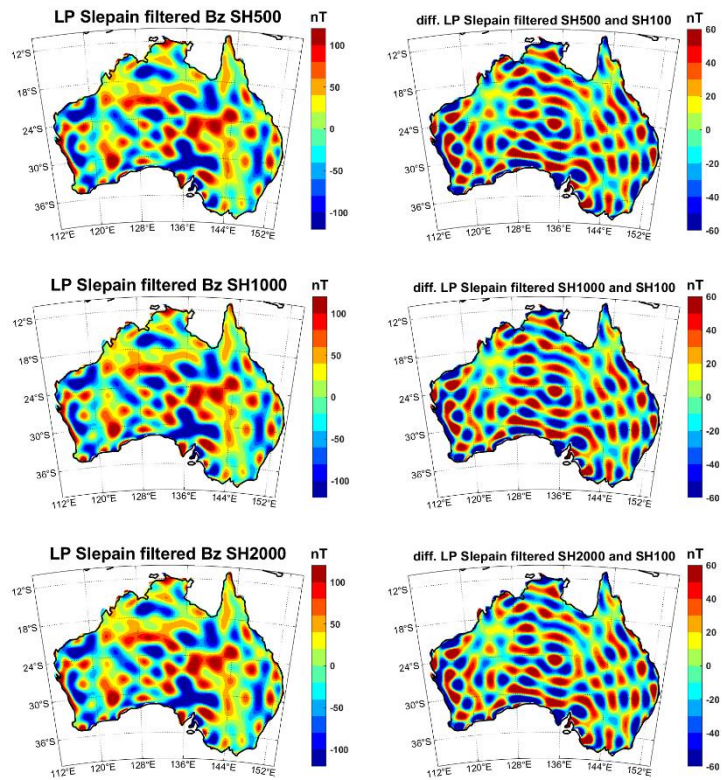


Figure 2.8: Slepian filtered synthetic data (expanded to different SH degree) using first 300 Slepian basis functions and its difference between Figure 2.2 I

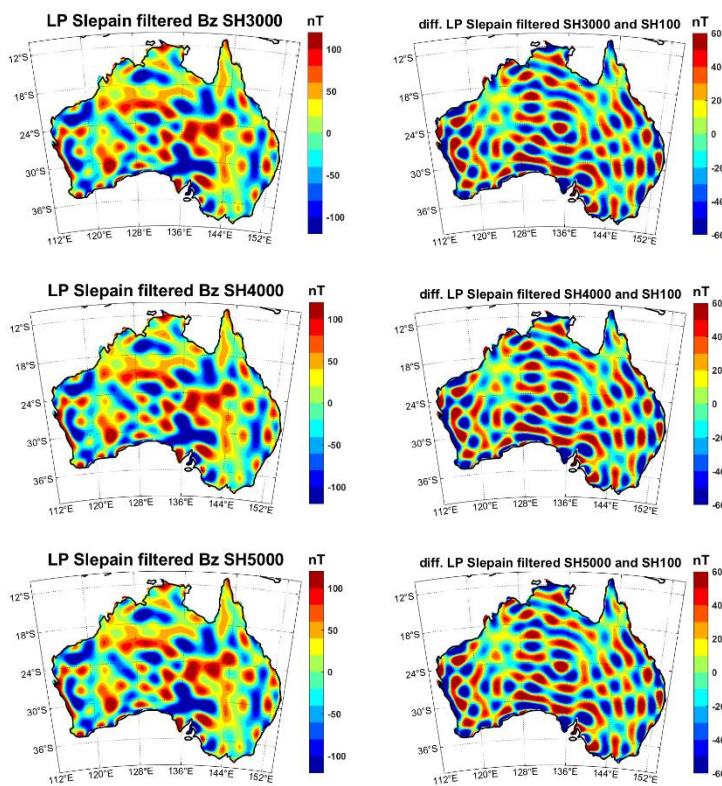


Figure 2.9: Slepian filtered synthetic data (expanded to different SH degree) using first 300 Slepian basis functions and its difference between Figure 2.2 II

Interestingly, the spectral leakage from input synthetic data of SH 1-5000 does not affect the Slepian coefficients equally. Figure 2.10 shows the percentage change between Slepian coefficients derived from the synthetic data of SH 1-100 and SH 1-5000 using first 300 Slepian basis functions as a low-pass filter. As can be seen from Figure 2.10, the relative change is above 100 % beyond first 150 Slepian coefficients and increases exponentially. However, the first 80 Slepian coefficients change less than 15 % with increase of input signal's bandwidth, which leads to an error of  $\pm 2$  nT (Figure 2.10, Figure 2.11).

As illustrated in Figure 2.10, high frequency components in the signal have severe impacts on higher order of Slepian coefficients but less impact on low order Slepian coefficients. Therefore, the first 80 Slepian basis functions which were generated from SH first 100-degree basis functions can be used as a low-pass filter to evaluate the long-wavelength distortion of the aeromagnetic anomaly map of Australia. Magnetic anomalies calculated from LCS1 were used as a reference to compare the long-wavelength components in satellite data and aeromagnetic data.

Figure 2.12 shows that overall long-wavelength patterns from two data sets are quite similar. However, significant long-wavelength distortions appear over the Yilgarn Craton in the west, sedimentary region in the central and orogen region in the south east part of the Australia.

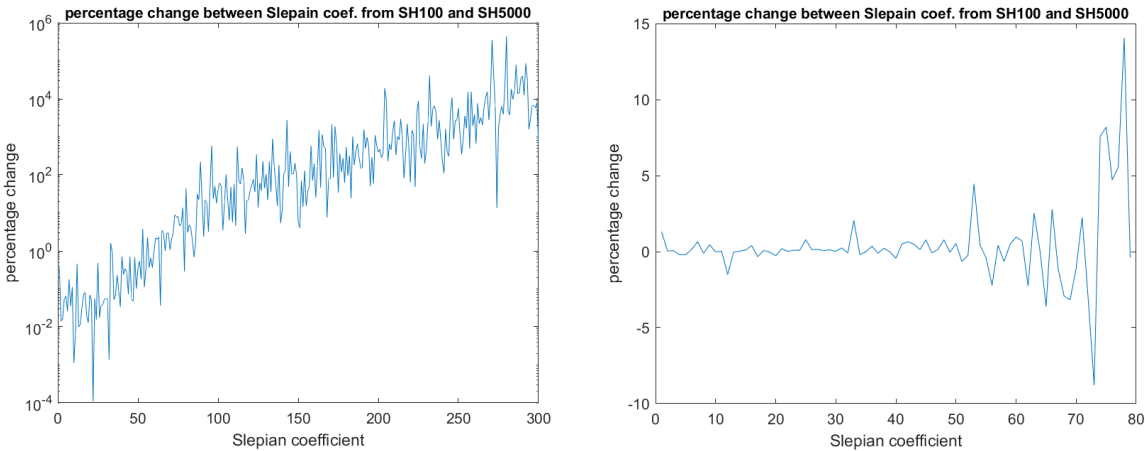


Figure 2.10: Percentage change between Slepian coefficients derived from the synthetic data of SH1-100 and SH1-5000

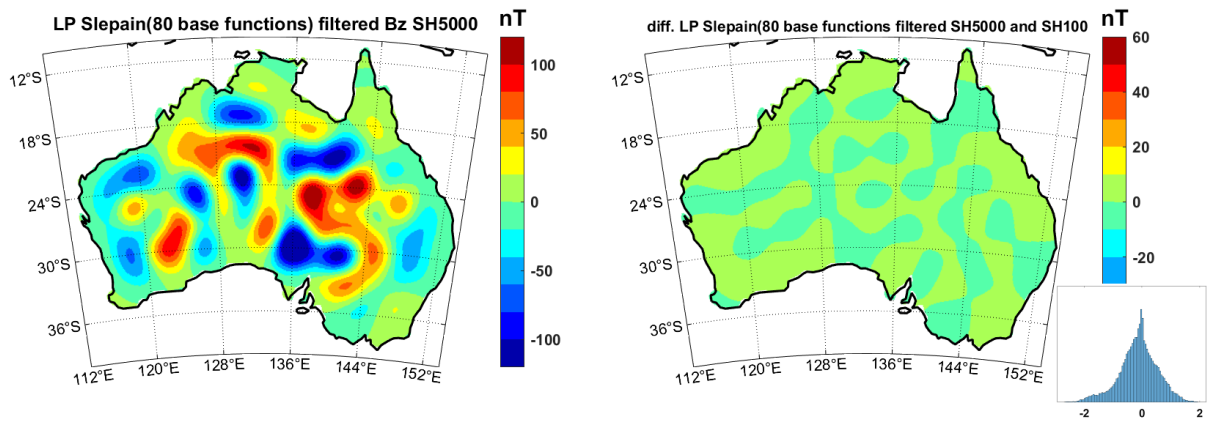


Figure 2.11: Slepian filtered synthetic data (expanded to different SH degree 5000) using first 80 Slepian basis functions. Left: filtered result from the synthetic data of SH1-5000. Right: difference between filtered result from the synthetic data of SH1-100 and SH1-5000

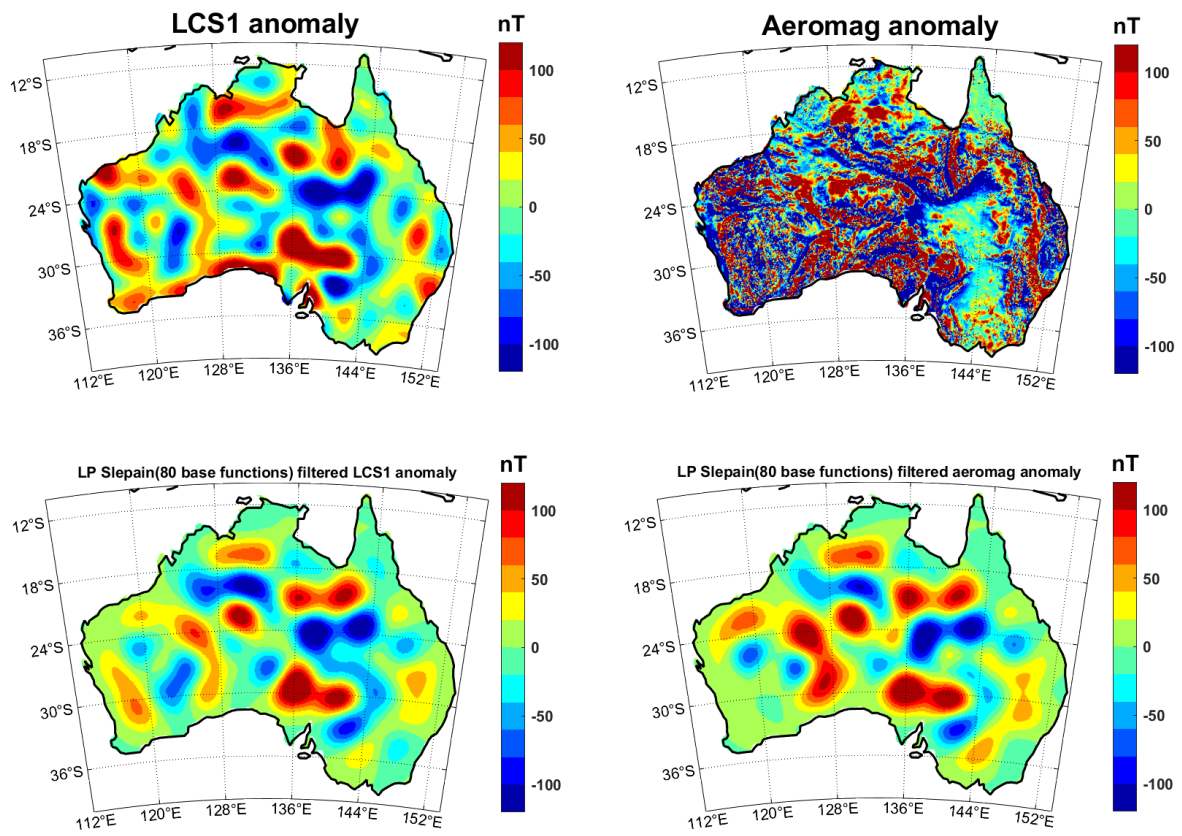


Figure 2.12: Slepian filtered satellite and aeromagnetic data (using first 80 Slepian basis functions)

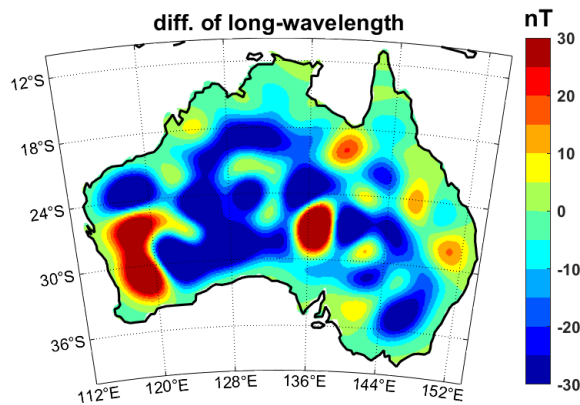


Figure 2.13: Long-wavelength difference of aeromagnetic data and LCS1 in terms of Slepian filtering using first 80 Slepian basis functions

### 2.3.3. Slepian filtering compared to Fourier domain filtering

As discussed above, it is crucial to select the number of the Slepian basis functions which in turn utilize a low-pass filter. There is a trade-off between spectral and spatial concentrations of a signal over a specific area (Simons et al. 2006). To tackle this issue, the eigenvalue of 0.5 is chosen to be a balancing point to separate the Slepian basis functions (see section 2.2.2).

If the first 153 Slepian basis functions are used instead of 300, which is the balancing point between the spectrally well-concentrated and spatially well-concentrated Slepian basis functions, it leads to a more similar result compared to FFT filtering (Figure 2.14, Figure 2.15).

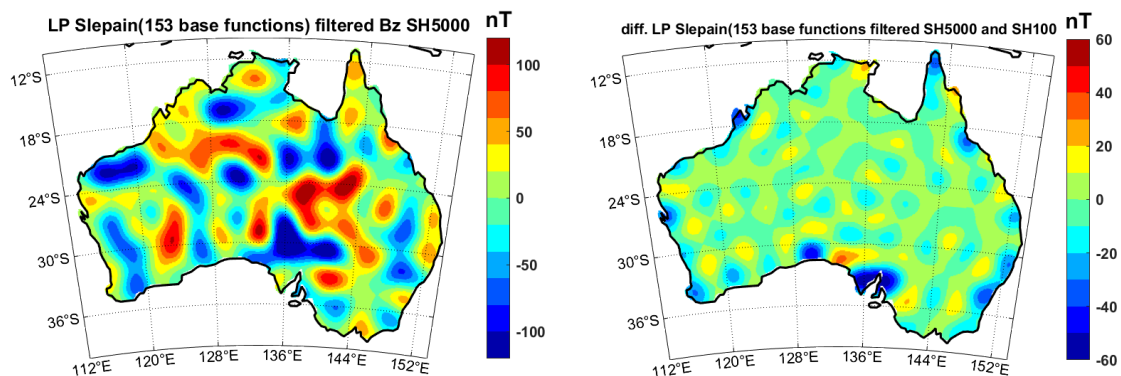


Figure 2.14: Slepian filtered synthetic data of SH1-5000 (using first 153 Slepian basis functions) and its difference between Figure 2.2

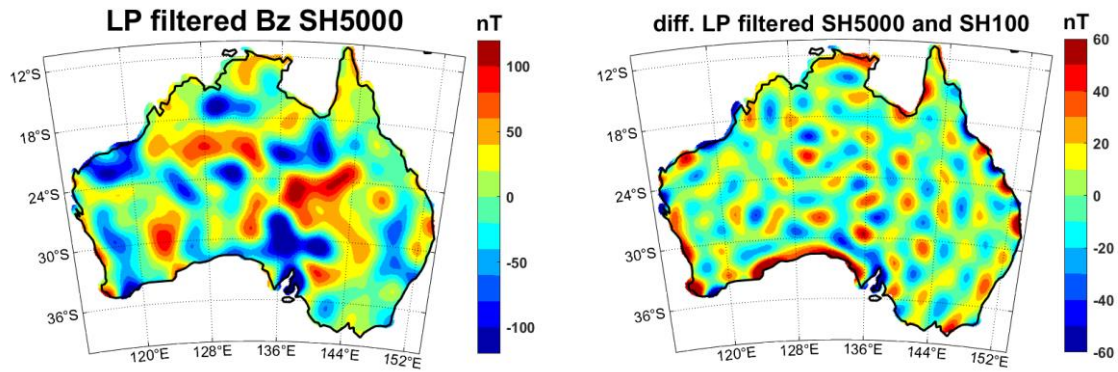


Figure 2.15: Low pass FFT filtered synthetic data of SH1-5000 (cut-off wavelength 400 km) and its difference between Figure 2.2

#### 2.3.4. Comparison of the three filtering approaches

To compare the three filtering approaches, the LCS-1 model was calculated up to 185 degree in 0.1-degree resolution and aeromagnetic data down sampled in 0.1-degree resolution. Slepian basis functions constructed from spherical harmonics up to degree 100 (first 153 Slepian basis functions used as a low-pass filter) and low-pass Butterworth FFT filtering (cutoff wavelength 400 km) methods were applied to the full-spectral LCS1 anomaly data and aeromagnetic anomaly data. LCS-1 model was expanded to SH degree 100 for SH filtering. Since SH filtering is not applicable for regional data, FFT filtering was applied to the aeromagnetic data as a proxy for SH filtering for comparison.

As discussed before, three filtered results of full-spectral LCS1 anomaly data are quite similar because the spectral leakage is not severe for satellite data (Figure 2.16 left column). For aeromagnetic data, the filtered results are slightly different especially around the coastal area (Figure 2.16 center column). The difference of long-wavelength components of satellite data and aeromagnetic data suggest that the Slepian method and the FFT method are comparable but they differ from spherical harmonic filtering due to the spectral leakage. Therefore, either Slepian or FFT methods can be used to merge the satellite and aeromagnetic data even though they introduce some spectral leakage.

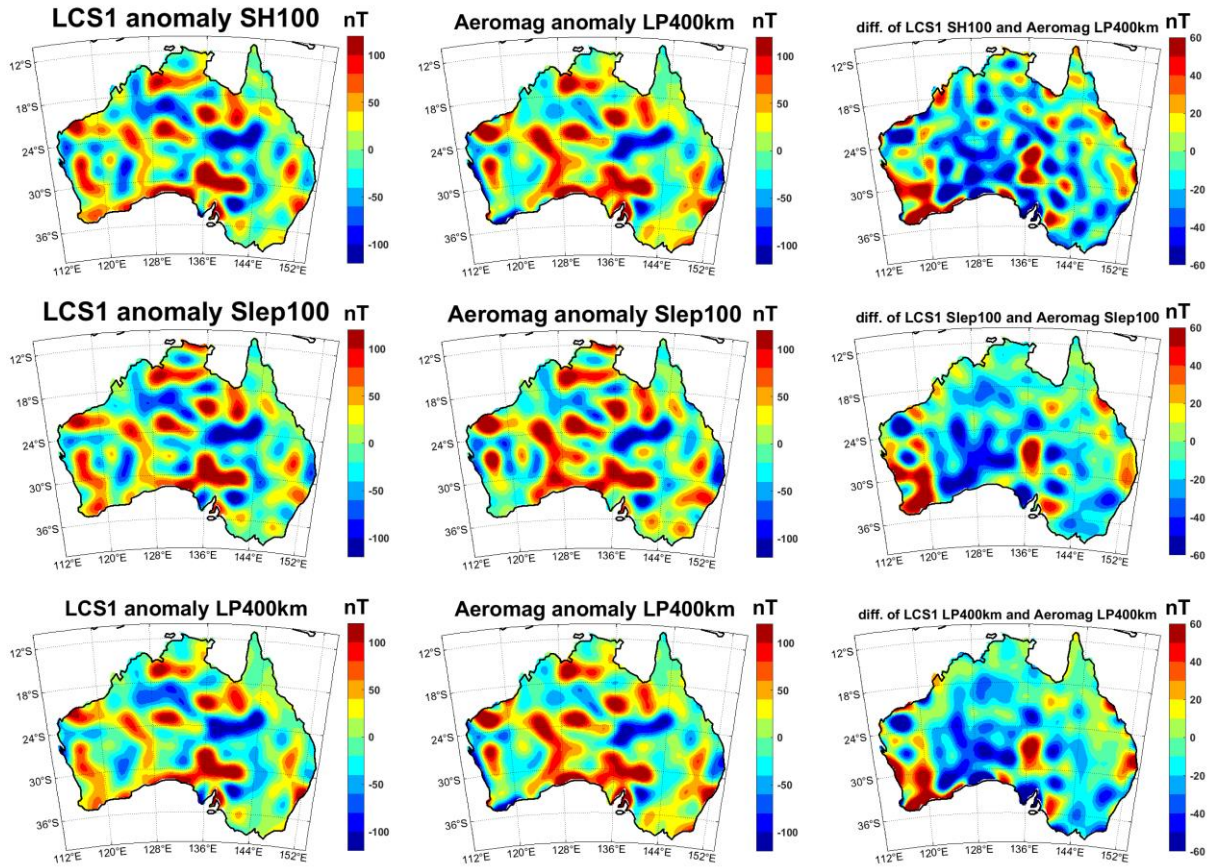


Figure 2.16: Comparison of the three filtering approaches (SH, Slepian and FFT). Left: filtered long-wavelength components of the LCS-1 anomaly data corresponding to SH degree up to 100. Middle: filtered long-wavelength components of the aeromagnetic anomaly data corresponding to SH degree up to 100. Right: difference between the left columns and right columns.

## 2.4. Conclusions

Three filtering methods were used to extract SH degree 1-100 signal from the SH expansions of synthetic SH coefficients up to degree 5000 at surface height. Fourier and Slepian filtering methods would map high frequency signals beyond SH degree 100 to the filtered data so that there is locally a large effect of spectral leakage up to  $\pm 100$  nT compared to SH expansion of degree 1-100. Although the two methods fail to assess the high frequency spectral leakage effect quantitatively, the long-wavelength patterns extracted from these two filtering methods are quite similar.

Theoretically, the Fourier filtering method is not suitable for large continental areas because it does not take in to account Earth's sphericity. In this case, the Slepian filtering method might be more reasonable that it works in spherical coordinate system. In addition, the spectral leakage effect in the Slepian filtering method is less severe than the Fourier filtering method when the spectral and spatial balancing eigenvalue of 0.5 is chosen to construct the Slepian basis functions. Therefore, the Slepian filtering method is better for analyzing long-wavelength signals from original full-spectrum signal despite there still locally exists high-frequency "noise".

Nevertheless, it could be possible to extract spectrally consistent long-wavelength components partly in terms of Slepian filtering. Although it is not the expected spectral part (SH degree 1-100 in this case), the long-wavelength distortion in aeromagnetic data still can be partly improved.

However, it is not practical to partly improve long-wavelength components of aeromagnetic data for real application since there is still a “spectral gap” in the data where it fails to reflect the true spectral contribution of the subsurface magnetic sources. In theory, it is possible to extract spectrally consistent components of aeromagnetic and satellite data as long as the spectral bandwidth of aeromagnetic data and Slepian basis functions is equal. For instance, 0.1-degree spectral resolution corresponds to roughly SH degree 3600 according to (2.11). As a result, it requires approximately 1300 TB memory to deal with the eigenvalue problem for constructing the Slepian basis functions in this bandwidth. Obviously, it is prohibitively expensive to implement the Slepian filtering method in this scenario.

Hence, practical and efficient way of analyzing spectral consistency of satellite and aeromagnetic data is still a challenging problem. To handle this problem, a physics-based method which works naturally in SH domain will be introduced in next chapter.

# Spectral consistency of satellite and airborne data: Application of an Equivalent dipole layer for combining satellite and aeromagnetic data sets

Yixiati Dilixiati, Eldar Baykiev, Jörg Ebbing

Institute of Geosciences Kiel University, Kiel, Germany

Submitted to *Geophysics*

## 3.1. Introduction

More and more near-surface magnetic data become available and a great number of nation-wide even continental-wide magnetic compilations have been published in recent years ([Bankey et al. 2002](#); [Milligan et al. 2004](#); [Gaina et al. 2011](#); [Golynsky et al. 2018](#)). There is a practical need to build large-scale magnetic compilation maps for regional studies, e.g. mineral prospecting and geological mapping ([Milligan et al. 2004](#); [Olesen et al. 2010](#); [Golynsky et al. 2018](#)), and in combination with other geophysical data and techniques, magnetic data help modelling and inversion of crustal structures ([Korenaga et al. 2000](#); [Fregoso and Gallardo 2009](#)).

However, processing of aeromagnetic survey data towards a compilation involves many steps (e.g. leveling, reference magnetic field reduction, grid merging), which inevitably introduce long-wavelength distortions ([Hamoudi et al. 2007](#)). Generally, two factors affect the long-wavelength part in magnetic compilations. Firstly, individual surveys are by nature small in dimension (usually less than several hundred kilometers) and cannot reflect the long-wavelength content larger than the survey dimension. A second source of error is the lack of data consistency. As continent-wide magnetic compilation are based on data acquired over decades, the data quality reflects instrumental improvement, navigation error and also the chosen reference field. After reducing all possible systematic error and bringing data sets to a common height, anomalies in overlapping areas rarely match. To eliminate this mismatch, some algorithms, involving shifting or tilting of a survey are used for the overlapping area or edge of the survey boundary to provide a smooth transition between adjacent surveys ([Bankey et al. 2002](#)). Consequently, the merging technique minimizes the misfit in the overlap area but affects as well the long-wavelength signal and in most cases, it is not possible to identify and correct the long-wavelength distortion introduced during processing. Comparison of the Canadian magnetic compilation and independent high-altitude EPB data which were acquired by

former Earth Physics Branch (EPB) of Canada suggests that long-wavelength distortion affects the spectral range between 300 and 2500 km ([Pilkington and Roest 1996](#)).

One possibility to correct the data is to introduce independent data as a “tie line” for leveling the merged data set. In Australia, two generations of long-haul surveys, the Australia Wide Airborne Geophysical Survey (AWAGS), have been carried out in order to improve the long-wavelength components of the Magnetic Anomaly map of Australia ([Milligan et al. 2004](#); [Milligan et al. 2009](#)). Although acquiring new magnetic data is relatively expensive and time consuming, such long-haul lines provide better control over long-wavelength ([Milligan et al. 2004](#)).

Nowadays often satellite data are used instead, which are globally available with an ever-increasing resolution. MF6 is a widely used satellite data driven magnetic model which claimed to be reliable up to spherical harmonic degree 120 corresponding to a wavelength of 333 km ([Maus et al. 2008](#)). Its updated version MF7 increases the spectral resolution up to degree 133 and scales down the wavelength to 300 km ([Maus 2010](#)). The recent lithospheric magnetic field model LCS-1 provides wavelengths down to 250 km ([Olsen et al. 2017](#)).

In practice, often a low pass FFT filter is applied to replace the long-wavelength part from the merged data grid with a satellite model ([Gaina et al. 2011](#)). Although this is a fast and simple approach, there are several disadvantages of utilizing FFT methods for merging data. (1) FFT assumes a plane surface, which is a good approximation for a small area only. When dealing with a continental-scale data set, one should ideally take the sphericity of the earth into account. (2) FFT cannot account for the varying height of acquisition between different surveys and a mean height is often used or the data upward continued to a common level. (3) FFT and spherical harmonics are defined in different spectral basis so that the filtered data in Fourier domain do not necessarily represent the same spectral information in spherical harmonic domain. In addition, satellite magnetic data are naturally filtered in spherical harmonic domain with respect to the height. Therefore, it is more natural to combine the satellite and near-surface data in the spherical harmonic domain which is the solution to the Laplace’s equation that holds for both data sets. Since spherical harmonics are globally supported functions that are not orthogonal over regional area, it would limit the applicability of spherical harmonics on global scale.

To this end, we developed a new approach to combine and analyze the satellite data and aeromagnetic data in the spherical harmonic domain for a regional area by making use of an equivalent source technique and spectral representation of a dipole field. The main advantage of this proposed method is that one can apply classical spherical harmonic analysis in regional area. This method consists of two parts, inversion of the magnetic parameters using equivalent dipole layer and conversion of magnetic parameters into spherical harmonic coefficients. The details of this approach are presented in the following section.

### 3.2. Magnetic Models and Aeromagnetic Data

For satellite data, we used two magnetic models in this study, the satellite-only lithospheric magnetic field model LCS-1 and the World Digital Magnetic Anomaly Map (WDMAM) based on combination of all available data. LCS-1 is derived from CHAMP and Swarm gradient data, whose spherical harmonic coefficients are available up to spherical harmonic degree 185. Due to the special constellation of the Swarm satellite mission, directly measured gradient data from Swarm satellites can help suppress the contribution of external magnetic fields so that improve the lithospheric field modeling ([Olsen et al. 2017](#)).

The WDMAM is an international project to compile world-wide near surface magnetic data ([Lesur et al. 2016](#)). In this paper we used the WDMAM spherical harmonic model, which consists of spherical harmonic degree up to degree 720 and the long-wavelength part of WDMAM model ranging from spherical harmonic degree 16-100 was corrected by long wavelength synthetic data derived from the GRIMM\_L120 magnetic model due to the fact that grid-stitching method would introduce unreliable long-wavelength distortion ([Lesur et al. 2016](#)). Since the LCS-1 model provides band-limited long-wavelength component of the crustal field, the main reason for using WDMAM model is to mimic the broad-band nature of the aeromagnetic data as much as possible.

For aeromagnetic data, we used three sequential edition of the Australia magnetic anomaly map (Figure 3.1) to systematically analyze the long-wavelength improvement by the individual control flight data. The Magnetic Anomaly Map of Australia was published in 1992, which was a magnetic compilation of 4 million-line kilometers of survey data over 40 years ([Tarlowski et al. 1992](#)). It was updated with the second edition in 1996. The 3rd edition was published in 1999 and updated in 2002 ([Petkovic and Milligan 2002](#)). The 4th edition was the milestone for the Australia magnetic anomaly map that substantially increased the data coverage to 19 million-line kilometers of survey data most of which were acquired in the 1990s ([Milligan et al. 2004](#)). Due to the individual control flight leveling the 4th edition has an improved control over the long-wavelength components. The control flight lines were part of the Australia Wide Array of Geomagnetic Stations (AWAGS-1) which was finished in the early 1990s and consists of two control traverse and 58 magnetic stations – four of them were permanent observatories ([Milligan et al. 2001](#)).

For the 5th edition 8 million-line kilometers of survey data were added and the long-wavelengths were leveled by additional control flight lines from AWAGS-2 ([Franklin and Milligan 2010](#)). The Australia Wide Airborne Geophysical Survey (AWAGS-2), completed in 2007, acquired data over the whole of Australia in an east-west direction with 75 km flight line spacing and tie lines in a north-south direction with 400 km spacing. Additionally, magnetic data from ground sites were used to correct the diurnal variation of the Earth's magnetic field for AWAGS-2 ([Milligan et al. 2009](#)). In addition, wavelengths

greater than 1000 km were replaced with data from the satellite magnetic field model MF6 (Franklin and Milligan 2010).

As can be seen in Figure 3.1, there is little difference between the 4th edition and 5th edition of magnetic anomaly maps by visual inspection, while the 3rd edition is obviously different as there has been no long-wavelength correction.

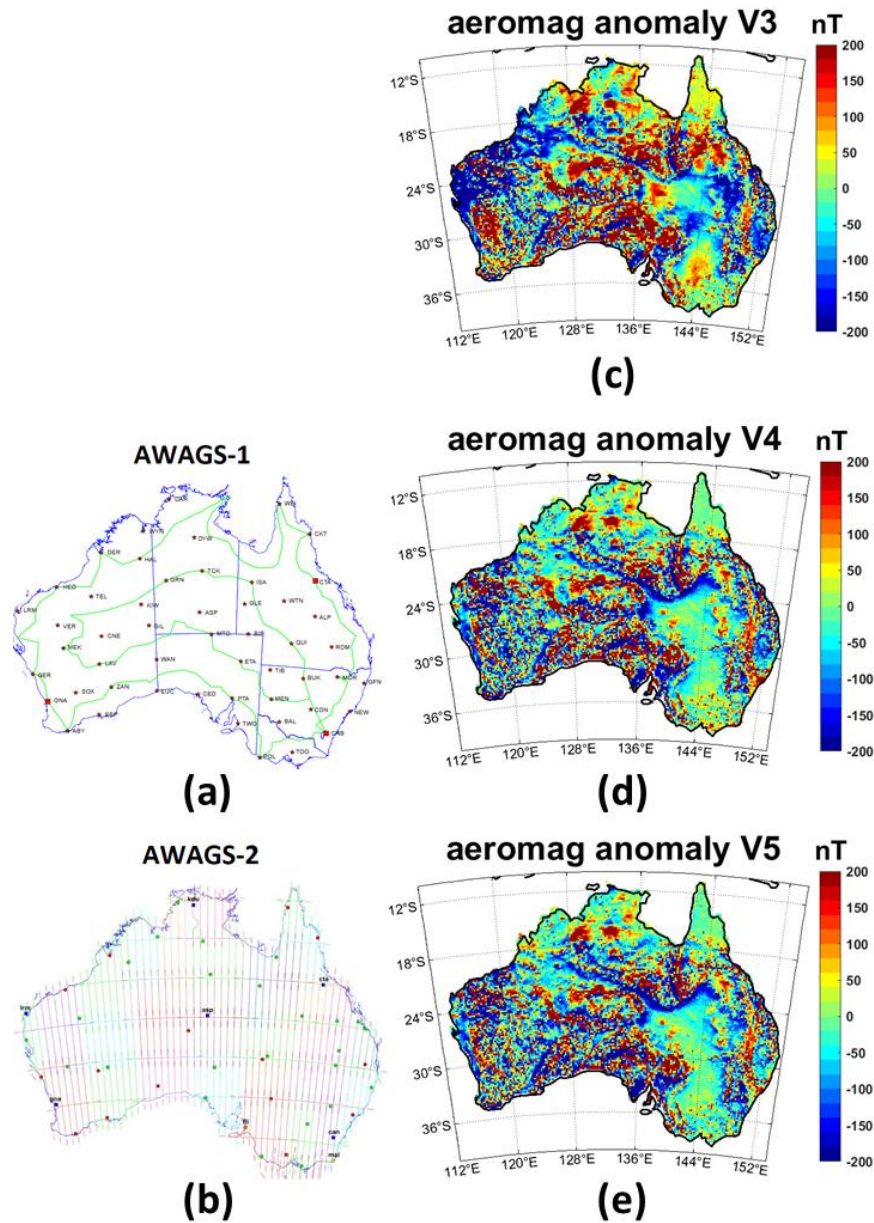


Figure 3.1: AWAGS control flight lines: (a) AWAGS-1 flight lines (green) and ground-based magnetic sites (red), (b) AWAGS-2 checkerboard flight lines (colored lines) and ground-based magnetic sites (colored dots); Magnetic anomaly map of Australia in 0.2-degree resolution: (c) 3rd edition, (d) 4th edition, (e) 5th edition

### 3.3. Methods

#### 3.3.1. Inversion of the equivalent dipole layer

The equivalent source technique is a simple and versatile method that is mainly used to perform potential field data processing and regridding ([Oliveira Jr et al. 2013](#)). This technique dates back to the turn of the 1960s when it was proposed to reconstruct gravity data on an irregular distributed grid ([Dampney 1969](#)). Later on, several applications based on this method have been developed ([Parker and Klitgord 1972](#); [Bhattacharyya and Chan 1977](#)). The beginning of the satellite era makes it possible to estimate the crustal magnetization and thickness from regional area (e.g. Australia) to the global scale utilizing this method ([Mayhew et al. 1980](#); [Mayhew 1982](#); [Arkani-Hamed and Strangway 1985](#); [Whaler and Langel 1996](#)). Generally, potential fields satisfy the Laplace equation in the source-free region. If the boundary condition is known for this region, there exists an infinite variety of source distributions outside this region which can explain the field in this source-free region ([Li and Oldenburg 2010](#)). Practically, only one simple imaginary layer of sources, the equivalent source layer, is needed to reconstruct the known field data. Note that the equivalent source does not represent the true source but has the same effect outside the source region. Hence, this technique provides mathematical simplicity to potential field data reprocessing (e.g., upward continuation, reduction to the pole). As discussed above, satellite data reflect the band-limited part of the near-surface data. One needs a suitable mathematical tool to decompose the near-surface aeromagnetic data and satellite data into the same spectral domain in order to combine the spectrally consistent part of the two data sets. Equivalent source method is a necessary part in our method to achieve this goal.

Iterative inversion methods are efficient for finding the estimated solution to a large linear system because the computational cost of direct methods (e.g. LU and SVD decomposition) often becomes prohibitive ([Freund et al. 1992](#)). The Krylov subspace methods (e.g. conjugate gradient) are a well-studied and established class of iterative methods for solving linear systems ([Golub and van der Vorst 1997](#)). For non-symmetric matrices, the biconjugate gradient stabilized method (BiCGSTAB) is a widely used Krylov subspace method, which is a fast and smoothly converging variant of biconjugate gradient (BiCG) method. However, the convergence of BiCGSTAB might suffer from serious stagnation or breakdown ([Sleijpen and Fokkema 1993](#)). To avoid the stagnation, the BiCGSTAB method was used with respect to the normal equation ( $A^T AX = A^T B$ ) in our case.

Following the eq. 4.14 of [Blakely \(1996\)](#), the magnetic vector field of a dipole with respect to induced magnetization is

$$\vec{B}_p = \frac{xV}{4\pi d^3} [3(\vec{B}_c \cdot \hat{d})\hat{d} - \vec{B}_c] \quad (3.1)$$

where  $\vec{B}_p$  is the magnetic vector at observation point  $P$ ,  $\chi$  the magnetic susceptibility,  $V$  the volume of the dipole sphere,  $d$  the distance between the dipole source and observation point and  $\hat{d}$  is its unit vector.  $\vec{B}_c$  represents the main field at source point.

The forward calculation of the total field anomaly is linearized by projecting the vector field onto the main field at observation point  $P$  (eq. 8.24 of [Blakely 1996](#)), which is

$$\Delta T = \vec{B}_p \cdot \hat{B}_c \quad (3.2)$$

where  $\Delta T$  is the total field anomaly,  $\hat{B}_c$  the unit vector of the main field at observation point  $P$ . In this study, the CHAOS-6 core field model was used for LCS-1 for consistency because this core field model was used to derive the LCS-1 model. However, the IGRF model was used for aeromagnetic compilations and WDMAM model with respect to the year when they were published. This is because IGRF model is normally applied to aeromagnetic data to remove the core field.

The inverse problem can be represented in a matrix form  $AX = B$  with respect to eq. (1) and eq. (2) where  $A$  consist of each dipole's magnetic effect at each observation point,  $B$  is a column vector of observed field (vertical component for satellite model and total field anomaly for aeromagnetic data),  $X$  contains physical parameter  $\chi V$  of each dipole source. As mentioned above, the linear system  $AX = B$  is transformed to its normal equation form ( $A^T AX = A^T B$ ) to avoid the stagnation of the BiCGSTAB method.

### 3.3.2. Spectral representation of a dipole field

Normally, it is difficult to directly apply spherical harmonic (SH) approach to the regional area since SH basis functions are only orthogonal over the whole spherical surface. It is not possible to convert the potential field data into the SH coefficients using regionally limited data. If the physical parameters are known, however, it is possible to represent the regional potential field in SH domain. Because the effect of the known sources can be forward calculated at the whole spherical surface, the orthogonality of the SH still holds. As we can see from eq. (3.1),  $\vec{B}_p$  is the function of the distance between dipole source and observation point for the known physical parameters  $\chi V$  and the main field  $\vec{B}_c$ . Therefore, inversion result of a regional area can be further forward calculated to the entire globe in order to convert the global signal to SH coefficients. Consequently, this two-step inversion and forward calculation approach makes it possible to expand the regional data to global coverage.

The standard way of converting globally distributed potential field data into SH coefficients is to evaluate a double integral of inner product of the data and specific SH basis function over two-dimensional spherical surface. In practice, the integration must be done numerically and approximated by FFT-based fast algorithm ([Driscoll and Healy 1994](#)). However, it is not necessary to use this standard

method to obtain the SH coefficients. Because the dipole source is mathematically simple and it is possible to derive the SH coefficients directly from the formula of the dipole field (see Appendix for details). The magnetic scalar potential  $\Omega$  of a dipole can be expressed in space domain as

$$\Omega(P) = -\frac{\chi V}{4\pi} \vec{B}_c \cdot \nabla_P \left( \frac{1}{|\vec{d}|} \right) \quad (3.3)$$

Mathematically equivalent form of  $\Omega$  in SH domain at observation point  $P(r, \varphi_r, \theta_r)$  can be given by

$$\Omega(r, \varphi_r, \theta_r) = \sum_{n=1}^N \sum_{m=0}^n (\mathcal{G}_n^m \cos m\varphi_r + \mathcal{H}_n^m \sin m\varphi_r) S_n^m(\cos \theta_r) \quad (3.4)$$

$$\mathcal{G}_n^m = \frac{\chi V}{4\pi r^2} \sum_{s=0}^{\infty} \sum_{m=0}^n \left(\frac{s}{r}\right)^{n-1} \left[ B_c^x \cos(m\varphi_s) \frac{\partial S_n^m(\cos \theta_s)}{\partial \theta_s} - \frac{m B_c^y}{\sin \theta_s} \sin(m\varphi_s) S_n^m(\cos \theta_s) + n B_c^z \cos(m\varphi_s) S_n^m(\cos \theta_s) \right]$$

$$\mathcal{H}_n^m = \frac{\chi V}{4\pi r^2} \sum_{s=0}^{\infty} \sum_{m=0}^n \left(\frac{s}{r}\right)^{n-1} \left[ B_c^x \sin(m\varphi_s) \frac{\partial S_n^m(\cos \theta_s)}{\partial \theta_s} + \frac{m B_c^y}{\sin \theta_s} \cos(m\varphi_s) S_n^m(\cos \theta_s) + n B_c^z \sin(m\varphi_s) S_n^m(\cos \theta_s) \right]$$

where  $r$  and  $s$  are the distance to the source point and observation point from Earth's center respectively,  $n$  and  $m$  the SH degree and order,  $\theta$  and  $\varphi$  the colatitude and longitude,  $xyz$  denote the three components of the main field in local North-East-Down coordinate system and  $S_n^m$  represents the Schmidt quasi-normalized spherical harmonics of degree  $n$  and order  $m$ .

Therefore, physical parameters  $\chi V$  can be transformed to SH coefficients in an analytical manner so that the intermediate step of integration can be avoided and the numerical accuracy can be preserved.

### 3.4. Results

#### 3.4.1. Regional SH reconstruction of the data from the magnetic models

The proposed method was tested by using the vertical components of LCS-1 and WDMAM models as input data. Note that the magnetic models are considered as noise-free for validation of the method, and the reliability of LCS-1 is discussed together with the aeromagnetic compilations. In addition, the vertical component was chosen because of its similarity to the total field anomaly both in terms of patterns and magnitude. For computation reasons, vertical components of the two magnetic models were calculated over Australia at 0.2-degree grids by expanding their SH coefficients up to SH degree 185 and 720 respectively. The input data were calculated at 100 m above the spherical surface of the Earth with regard to the altitude of the aeromagnetic data. The input data are shown in Figure 3.2a and Figure 3.2b.

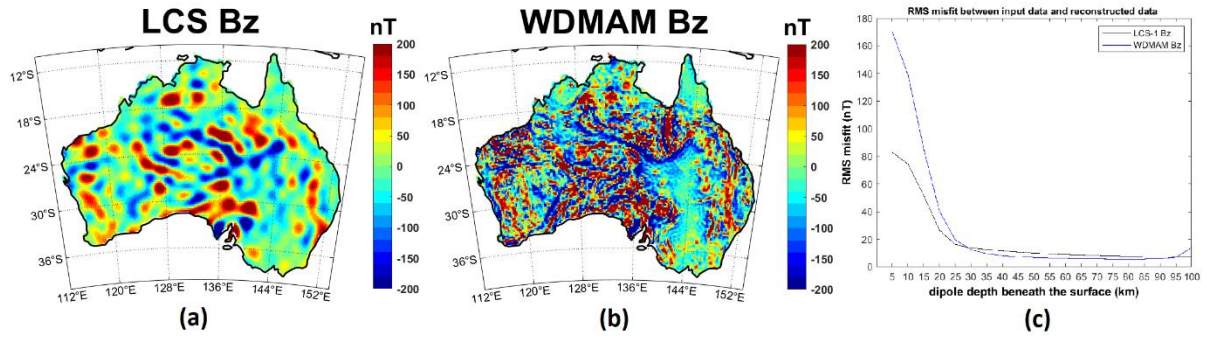


Figure 3.2: (a) LCS-1 Bz component at 100 m above the spherical surface, (b) WDMAM Bz component at 100 m above the spherical surface, (c) RMS misfit of reconstructed data and input data with respect to different dipole layers

A layer of magnetic dipoles which were placed at various constant depths beneath the spherical surface was obtained to fit the input data (Figure 3.2c). The equivalent layer consists of 17207 dipole sources that have the same coordinates as the input data. According to eq. (3.1), a linear system can be constructed in the form of  $AX = B$  where  $A$  is a square matrix (17207 by 17207) that contains each dipole's contribution to Bz component at each input data point and  $B$  is the vertical component from the magnetic models. This classical linear inverse problem of estimating the unknown  $X$  was carried out by BiCGSTAB iterative inversion method. The unknown  $X$  which represents the physical parameter  $xV$  of each dipole were obtained by setting the relative residual error for convergence to  $1e-5$  and initial guess of zero vector so that the misfit level is comparable (Table 3.1). The inverted physical parameter  $xV$  is shown in Figure 3.3.

As the equivalent dipole layer deepens, however, the RMS misfit remains constant. Interestingly, corners of the L-shaped RMS misfit plot both appear around the dipole depth of 30 km, which indicates the optimal equivalent dipole layer for the region. The optimal dipole depth also can be observed in 2-D misfit plots (not presented here) that the patterns and magnitudes stabilize after 30 km of dipole depth. As mentioned in the method section, there are infinite number of dipole layers, which, in theory, can explain the original data equally well in the source-free region. However, only one simple dipole layer is needed to represent the effect of true sources due to the computational cost. Thus, a dipole layer placed at 30 km beneath the surface is a good approximation to cover both the long and short wavelengths of the near-surface data.

Table 3.1: BiCGSTAB iterative inversion for  $A^TAX = A^TB$  system

Dipole depth below mean earth radius (km)	Maximum number of iterations		Relative residual (norm of residual divided by norm of input Bz)	
	Input data LCS-1	Input data WDMAM	Input data LCS-1	Input data WDMAM
30	39.5	38.5	9.8e-06	9.9e-06

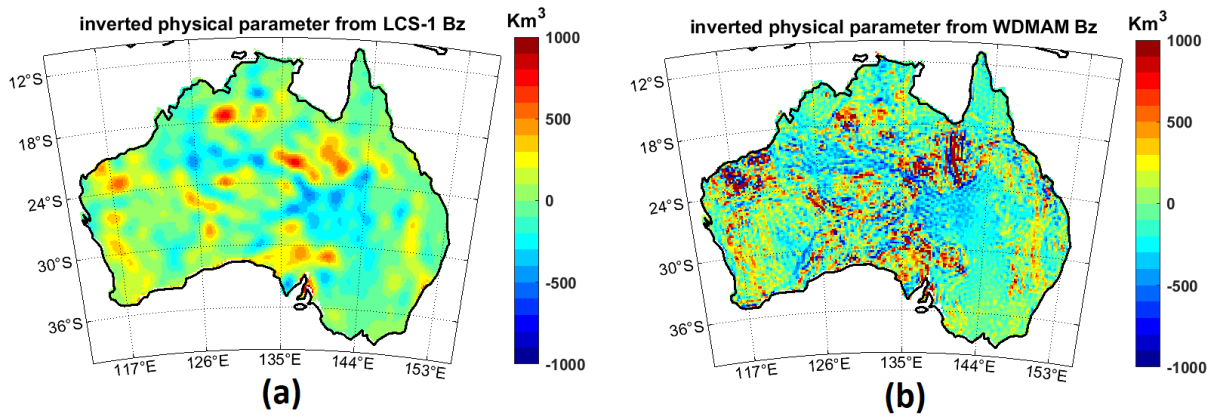


Figure 3.3: Inverted physical parameters: (a) from input data LCS-1 (Figure 3.2a) and (b) from input data WDMAM (Figure 3.2b) using equivalent source layer at 30 km depth

The aforementioned spectral representation of a dipole field was implemented to convert the magnetic parameters into SH coefficients. Further, the input data can be recovered using these SH coefficients. From Figure 3.4c and Figure 3.5c it can be seen that for dipoles at 30 km below surface the misfit between recovered data and original input data is relatively small except for coastal area (RMS 13.6 and 12.3 nT). The misfit relates to edge effect due to the surrounding magnetic sources which are not considered in the inversion. To reduce the edge effect, blank area was filled with data calculated from the magnetic models. As shown in Figure 3.4f and Figure 3.5f the edge effect from the coastline was forced to new boundary and misfit around the coastline was decreased hugely (RMS 4.4 and 8.8 nT).

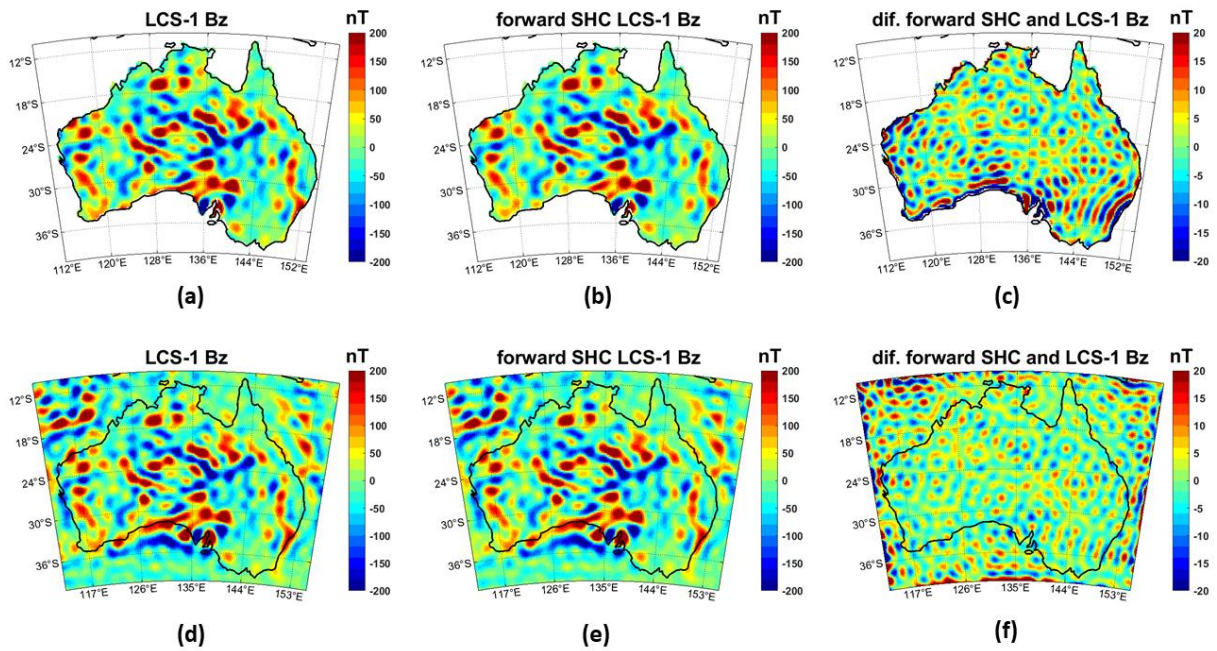


Figure 3.4: (a) Original LCS-1 data at 100 m above the spherical surface, (b) forward calculated field of the converted SH coefficients (SH degree up to 185) from equivalent dipole layer and (c) misfit between (a) and (b); (d) LCS-1 data in extended area, (e) forward calculated field of the converted SH coefficients (SH degree up to 185) from equivalent dipole layer and (f) misfit between (d) and (e).

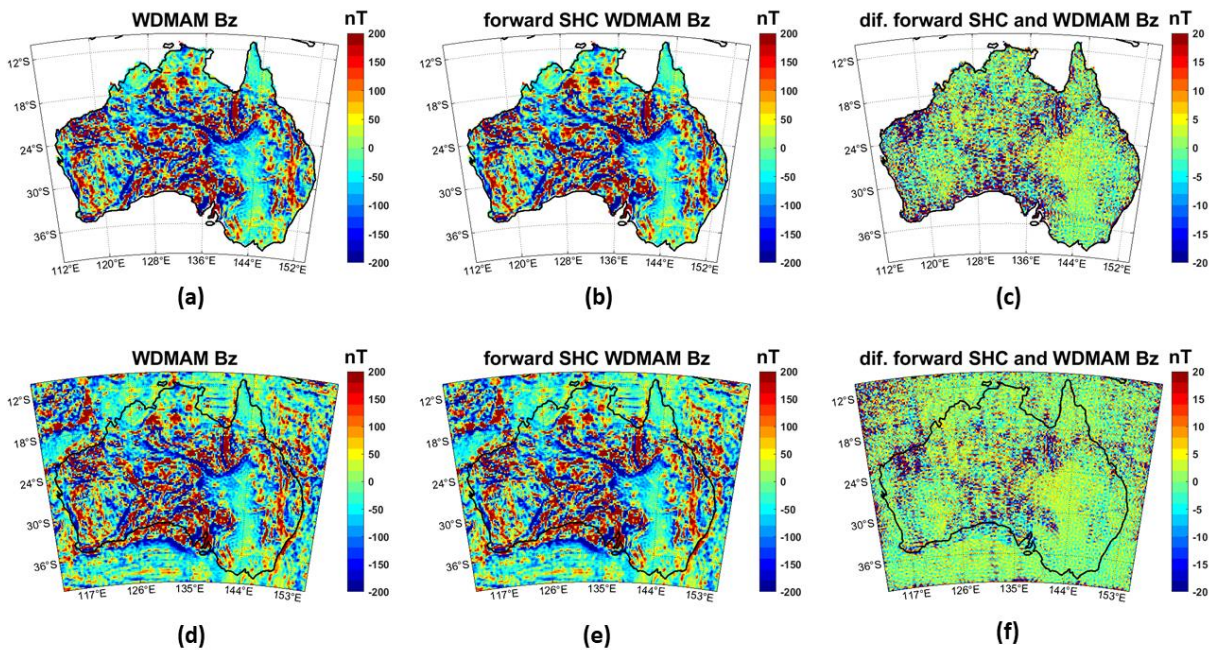


Figure 3.5: (a) Original WDMAM data at 100 m above the spherical surface, (b) forward calculated field of the converted SH coefficients (SH degree up to 720) from equivalent dipole layer and (c) misfit between (a) and (b); (d) WDMAM data in extended area, (e) forward calculated field of the converted SH coefficients (SH degree up to 720) from equivalent dipole layer and (f) misfit between (d) and (e).

What stands out in Figure 3.6 is the abrupt drops in the power spectrum of LCS-1 and WDMAM model. The steepest points of the drops are approximately at SH degree 185 and 720 respectively. This is not surprising because it stems from the spectrally band-limited nature of the input magnetic models. It reflects the maximum SH degree to which the input data was expanded. In contrast to the magnetic models, there are not sharp declines in the power spectrum of aeromagnetic data sets. It is also reasonable that aeromagnetic data are spectrally continuous resulting in a smooth SH power spectrum. For satellite-only data, SH degree 16-100 can be directly compared through the power spectrum (Figure 3.6). In the range of SH degree 16-28, the power spectrum of the magnetic models is almost identical even though they represent different satellite magnetic model (LCS-1 and GRIMM\_L120). Although it differs from SH degree 29-100, the general trend is quite similar. However, the power spectrum of LCS-1 declines slowly beyond the SH degree 110, whereas that of WDMAM shows higher power due to the contribution of the aeromagnetic data. This may imply that one can expect a high reliability of LCS-1 up to SH degree 110, which is justifiable by comparing the spectrum of LCS-1 and magnetic compilations in next section.

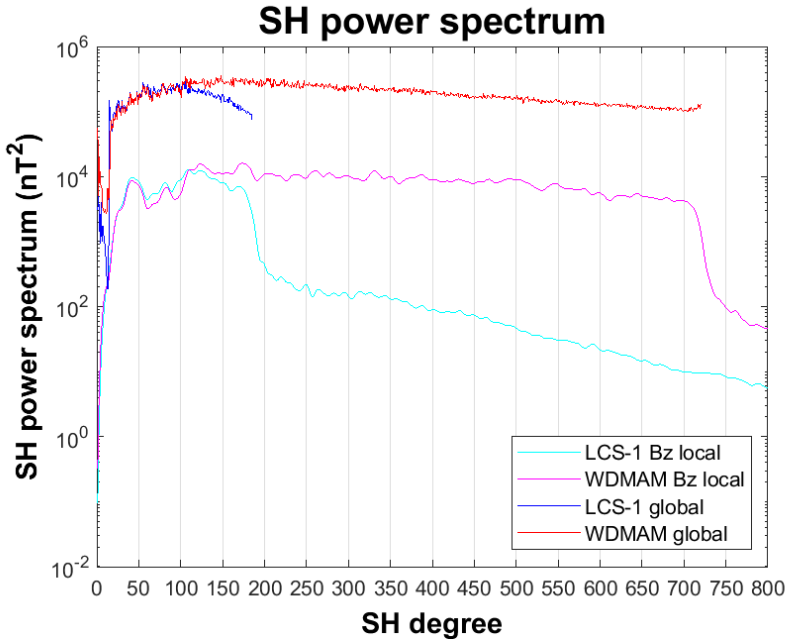


Figure 3.6: Spherical harmonic power spectrum (SH degree up to 800) of regional data calculated from magnetic models LCS-1, WDMAM and power spectrum from original model SH coefficients

### 3.4.2. Power spectrum of data sets of Australia

To assess the spectral consistency of satellite and aeromagnetic data, the 3rd edition, 4th edition and 5th edition of the magnetic anomaly map of Australia were used for systematic comparison. Because these three magnetic anomaly maps represent different long-wavelength improvement strategies. It is of practical importance that the effect of these different strategies can be recognized and quantitatively revealed using the proposed method. Therefore, these three aeromagnetic data were

processed in a manner similar to LCS-1 and WDMAM, which utilized the equivalent dipole layer at 30 km beneath the surface. The high-resolution aeromagnetic data were down-sampled to 0.2-degree resolution using nearest neighbor interpolation method (17207 points in total), which have same latitude/longitude coordinates as LCS-1 data. An altitude of 100 m above the topography (Global Land One-km Base Elevation) was chosen according to the published map of magnetic anomaly of Australia 5th edition since there is no information about flown height at each grid point. For consistency, vertical component of LCS-1 was calculated in 0.2-degree resolution and a same constant terrain clearance of 100 m. All inverted magnetic parameters were converted to the SH coefficients and the power spectrum was calculated.

Due to the fact that LCS-1 is band-limited that it is only available up to SH degree 185, one can compare satellite-only data with aeromagnetic data in this spectral range. Therefore, long-wavelength part of the power spectrum (SH degree up to 200) was selected to compare the spectral consistency of the satellite data and aeromagnetic data (Figure 3.7).

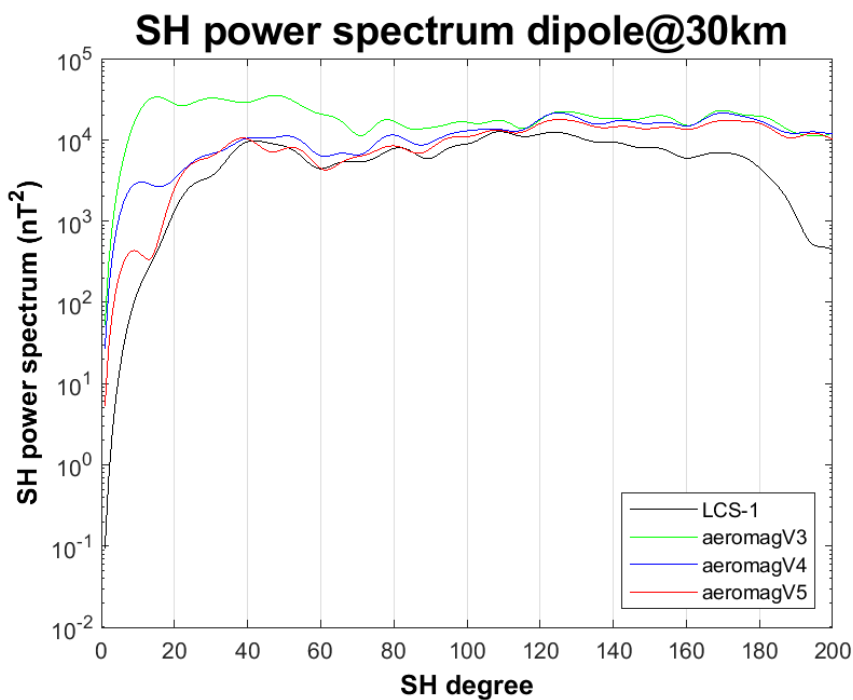


Figure 3.7: Spherical harmonic power spectrum (SH degree up to 200) of regional data

The long-wavelength improvement of the aeromagnetic data is well visible in the SH power spectrum. The spectrum of aeromagV3 and LCS-1 disagree up to SH degree 110, while that of aeromagV4 and aeromagV5 are close to the LCS-1 model. AeromagV5 shows a very good correlation to LCS-1 in the range of SH degree 40-110 owing to the high quality AWAGS-2 data. The main differences appear at SH degree 40 which is corresponding to spatial resolution of 500 km. This is probably due to the maximum dimension of the AWAGS-2 flight lines. In addition, the very long-wavelength difference of

aeromagV4 and aeromagV5 at SH degree 22 (corresponding to spatial resolution  $\sim 900$  km) can be explained by replacing the long-wavelength with a satellite model in AeromagV5. There is no detailed information about how the MF6 was used to constrain the wavelengths in excess of 1000 km. Despite that, this processing of constraining the long-wavelength part still can be detected from SH power spectrum.

According to the power spectrum analysis, the difference between the aeromagnetic data sets was calculated in space domain and SH domain using SH degree up to 110 (Figure 3.8). It is obvious that the improvement in space domain is dominated by the long-wavelength components. Figure 8a and 8b suggest that the individual levelling of AWAGS-1 has a huge impact on long-wavelength improvement. By further using the dense AWAGS-2 data (Figure 3.1b), the effect of long-wavelength improvement is minor compared to Figure 8a and 8b, which also can be seen in the power spectrum.

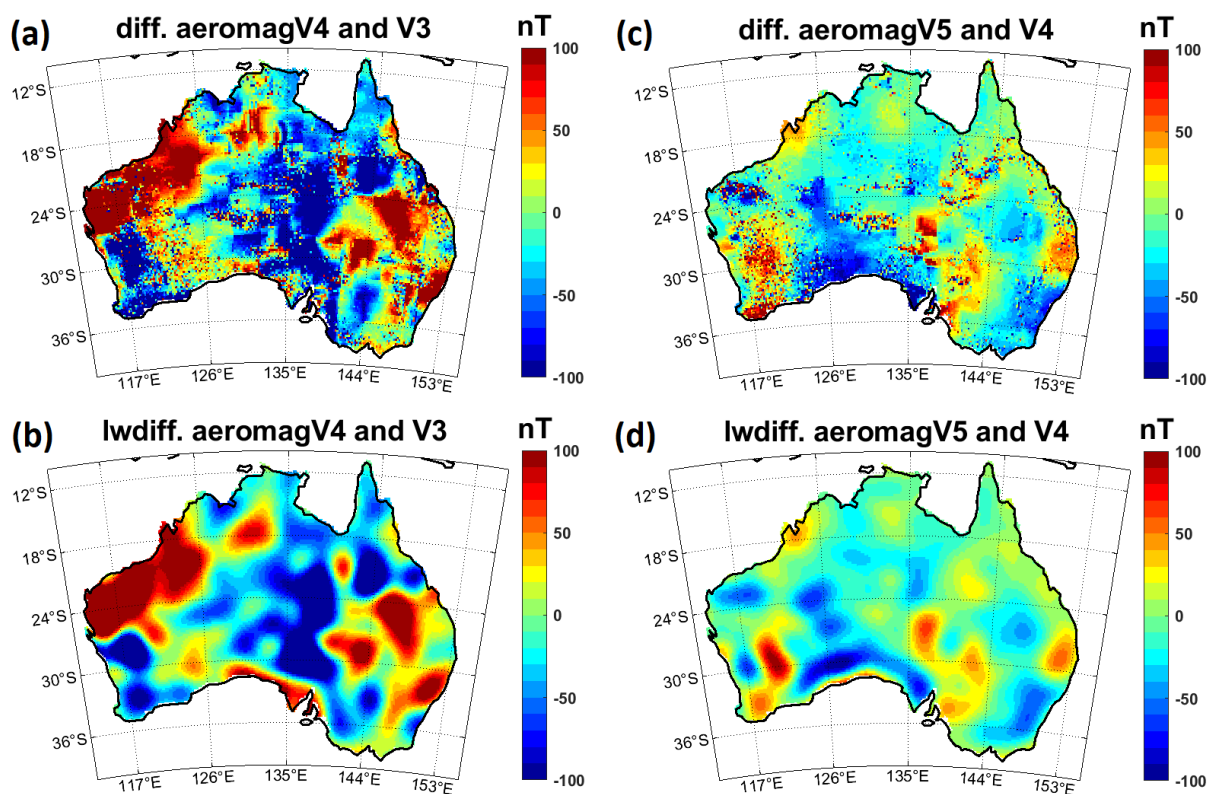


Figure 3.8: Long-wavelength improvement: (a) difference map between Australia magnetic anomaly map 4th edition and 3rd edition in space domain. (b) calculated long-wavelength difference of (a) using SH coefficients up to degree 110. (c) difference map between Australia magnetic anomaly map 5th edition and 4th edition in space domain. (d) calculated long-wavelength difference of (c) using SH coefficients up to degree 110.

However, above mentioned results did not consider the edge effect. As we can see from Figure 8c and 8d, overall patterns agree very well with each other except central-southern coastal area where the long-wavelength difference appears positive. The results of regional reconstruction of magnetic models suggest that extension of the original boundary to a new boundary can reduce this effect.

Therefore, we filled the blank area of aeromagV5 with data from magnetic models. As shown in Figure 9, blank area was filled with anomaly data calculated from LCS-1 SH degree up to 130 (Figure 3.9a) and anomaly data from WDMAM SH degree 131-720 was added on top of Figure 3.9a in Figure 3.9b. The power spectrum shows that the extension with LCS-1 data is enough for maintaining the long-wavelength. Note that the power spectrum of SH degree up to 130 represents the long-wavelength contribution of aeromagV5 onshore and LCS-1 offshore.

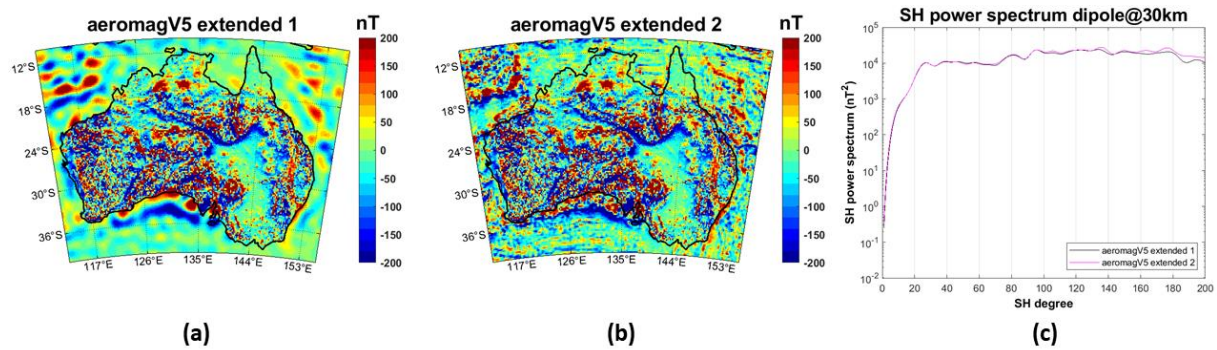


Figure 3.9: aeromagV5 extended with magnetic models: (a) blank area was filled with data calculated from LCS-1 SH degree up to 130, (b) data calculated from WDMAM SH degree 131-720 were added to (a) in blank area, (c) spherical power spectrum of (a) and (b).

Therefore, the surrounding oceanic area where there are no aeromagentic data available was filled with anomaly data calculated from LCS-1 (Figure 3.9a) for reducing the edge effect. The extension of data coverage of aeromagV5 with LCS-1 in space domain should not introduce distorted long-wavelength since LCS-1 is reliable up to SH degree 110 according to the spectrum analysis (Figure 3.7). We can expect the long-wavelength difference between aeromagentic data and LCS-1 should show overall same patterns for extended data coverage and original data coverage. As we can see from Figure 3.10a and Figure 3.10b, the edge effect mainly on the central-southern part of the coastline and overall patterns, as expected, are still unchanged. Finally, aeromagV5 was further improved by subtracting its long-wavelength components then adding its analogue from LCS-1 in the range of SH degree 15-110 (Fig. 10c).

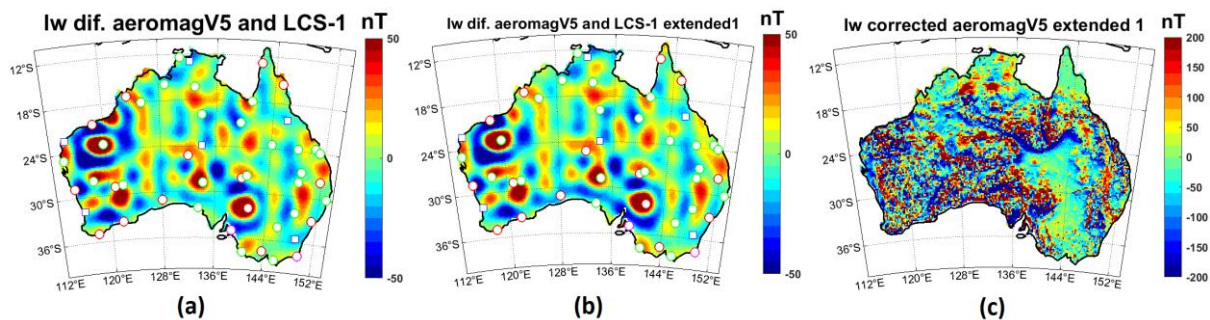


Figure 3.10: (a) long-wavelength difference between anomaly map 5th edition and LCS-1 in the range of SH degree 40-110 (contribution of the AWAGS-2 data) (b) similar as (a) but blank area was extended with LCS-1 data

and result was cropped to the coastline for direct comparison, white symbols represent the ground-based magnetic sites that blue squares are geomagnetic observatories, red circles temporary base sites at aircraft operational airports, green circles secondary temporary base sites and purple ones are extra sites (P. Milligan et al. 2009). (c) Australia magnetic anomaly map 5th edition long-wavelength component replaced by LCS-1 SH degree 15-110.

### 3.5. Discussion

Spherical harmonic representation of a dipole field was derived for local spherical harmonic analysis. The main purpose of the proposed method is to quantitatively compare the long-wavelength parts of satellite and aeromagnetic data. Some authors have attempted to study the consistency between near-surface data and satellite data, e.g. Pilkington and Roest (1996) compared high altitude EPB magnetic data with POGO-MAGSAT satellite data and near-surface aeromagnetic compilation data for Canada using Fourier-based upward continuation technique. The comparison suggested that wavelengths smaller than 300 km are reliable in the aeromagnetic compilation data, while long wavelengths between 300-2500 km are corrupted. To avoid the errors introduced by flat earth approximation of the upward continuation, Ravat et al. (2002b) used joint equivalent source inversion to estimate the spectral consistency between EPB magnetic data and satellite data, which agrees with previous result. Gaina et al. (2011) created two magnetic compilations of the Arctic replacing different wavelength components from MF6. Comparison of two candidate models shows that the long-wavelength correction (wavelengths greater than 400 km, 330 km) is strongly affected by the which wavelength is used. Therefore, spectral consistency between near-surface and satellite data is of crucial importance to apply long-wavelength correction to near-surface data.

Here, two magnetic models, namely LCS-1 and WDMAM, were used to test the effectiveness of the method. It suggests that equivalent dipole layer at 30 km below the surface can maintain the long-wavelength of the satellite data. The regional power spectrum also reveals the band-limitedness of the data which were calculated from magnetic models.

AWAGS-levelled aeromagnetic data sets have good agreements with LCS-1 in terms of power spectrum ranging from SH degree 40-110. Beyond this range, they differ gradually suggesting that at least one of them is problematic. Given that larger variances of SH coefficients due to the high-altitude Swarm observation data, LCS-1 model coefficients are not equally reliable over its entire range in that the uncertainties of them increase with SH degrees, which implies that LCS-1 might be highly reliable up to SH degree 120 (Olsen et al. 2017). In addition, a cross-spectrum analysis between central part of aeromagV5 and LCS-1 also indicates a sharp decline in spectral coherence beyond SH degree 110 (Olsen et al. 2017, Fig. 10). Although the method used by Olsen et al. (2017) is quite different (flat earth assumption with FFT-based cross spectrum analysis) from the method in this paper (equivalent source

technique combined with spectral representation of a dipole field), they all point to the same conclusion that the LCS-1 model coefficients are highly reliable up to SH degree 110 for Australia.

Comparing the power spectrum of aeromagnetic data sets alone, it can be seen that there is systematic improvement of the long-wavelength part due to the implementation of the individual AWAGS-1 and AWAGS-2. Milligan et al. (2004) has stated that there was a significant long-wavelength improvement (about 100-500 km wavelengths) in aeromagV4 but did not validate this improvement. This study validated their estimation that the long-wavelength improvement is corresponding to wavelengths around 180-500 km (SH degree 40-110) since the AWAGS data can control the wavelengths only up to 500 km (SH degree 40). This result also shows that AWAGS-2 outperformed AWAGS-1 since the spectrum of aeromagV5 is more consistent with LCS-1, which is not surprising considering the better coverage and dense flight lines of AWAGS-2. Although very long-wavelength of aeromagV5 was constrained by MF6, there was certain amount of uncertain long-wavelength component still left in the aeromagV5.

Comparing the contribution of the AWAGS-2 data in spectral domain, the long-wavelength difference of aeromagV5 and LCS-1 shows patterns related to the flight lines and ground magnetic stations (Figure 3.1b and Figure 3.10b). Although we can see patterns along with north-south even some east-west direction, they are not continuous. However, we cannot exclude the possibility that the north-south stripes could be related to satellite tracks. Even though the cause of the north-south long-wavelength difference is uncertain, the strong correlation between location of the ground-based magnetic sites and long-wavelength difference in the range of SH degree 40-110 indicates that there are long-wavelength uncertainties introduced by diurnal correction of the AWAGS-2 data. The removal of diurnal variation of the Earth magnetic field was done by extrapolating the diurnal variation recorded at ground-based magnetic sites out to nearby AWAGS-2 flight lines. As Milligan et al. (2009) explained, this linear extrapolation approach overly simplifies the actual time dependency of the magnetic field because it is not necessarily linear in space also time and the relative position of the aircraft between ground-based magnetic sites are also problematic. Therefore, we can expect some correlation between the position of the magnetic sites and long-wavelength patterns due to the extrapolation of the diurnal correction.

### 3.6. Conclusion

The proposed method provides a new tool for analyzing the spectral consistency of regional data sets. With the help of AWAGS-2, the Australian aeromagnetic data have good agreement with LCS-1 in the spectral range of SH degree 40-110. The results suggest that even this carefully processed aeromagV5, not to mention poorly constrained magnetic compilation data, has room for long-wavelength improvement.

## Chapter 4

# Variable reduction to the pole using equivalent source technique

### 4.1. Introduction

Reduction to the pole (RTP) is a standard magnetic data processing method which is aimed at simplifying the complex information provided by the original magnetic data. Magnetic anomalies not only depend on the distribution of the magnetization, but also on the direction of the magnetization and ambient main field. If only induced magnetization is considered, the susceptibility and the ambient main field determine the amplitude and shape of the anomalies.

If the magnetization and ambient main field are not vertically orientated, a symmetrical distribution of magnetization will produce an asymmetric magnetic anomaly ([Blakely 1996](#)). The RTP operation can transform this magnetic anomaly 'symmetrical' as if it would have been measured at the magnetic pole. Hereby, remanent magnetizations are neglected. Therefore, RTP simplifies the interpretation of magnetic data by removing the influence of magnetic latitude on magnetic data.

[Baranov \(1957\)](#) first introduced the theoretical concept of RTP and developed a convolution operation technique in the spatial domain. However, the mathematical and computational complexity of the method hindered the practical application of this method. [Bhattacharyya \(1965\)](#) proposed a double Fourier series expansion method to express the magnetic field and converted the convolution operation into spectrum domain. Following the work of [Bhattacharyya \(1965\)](#), [Ervin \(1976\)](#) utilized the fast Fourier transform to reduce the computational complexity.

Although RTP operation is computational efficient in the spectral domain, it becomes unstable at low magnetic latitudes where the inclination of the Earth's main field is close to zero. As the inclination approaches zero the RTP operator increases exponentially. In worst-case scenario for some specific points, the RTP operation approaches infinity ([Mendonça and Silva 1993](#)). Therefore, it would unnecessarily amplify the noise in the data and produce patterns along the direction of declination ([Li and Oldenburg 2001](#)).

An entirely different way of solving this low magnetic latitude problem is to use an equivalent layer technique which can explain the data ([Silva 1986](#)). The main idea behind this is to circumvent the Fourier based RTP problem by a 2-step linear inversion. The first step involves the calculation of the equivalent sources which have the best fit to the observed data, as shown in the previous chapter. In the second step, the RTP is obtained by recalculating the magnetic field with a vertically oriented

inducing main field. It also has advantages over the spectral domain methods that it can deal with variable geomagnetic inclination and declination over large areas.

## 4.2. Methods

RTP can be implemented either in the spatial or frequency domain. Benefiting from the computational efficiency of FFT, the frequency domain RTP method is the most popular and cost-efficient method. And although these conventional techniques have been commonly used, there are several drawbacks inherent to frequency domain methods.

Firstly, the RTP transformation is unstable near the geomagnetic equator where inclination is zero. The RTP filter in the frequency domain is expressed as (Silva 1986)

$$F(\gamma, \theta) = 1/[i \cos I_0 \cos(D_0 - \theta) + \sin I_0] [i \cos I \cos(D - \theta) + \sin I] \quad (4.1)$$

Where  $\gamma, \theta$  are the wavenumbers in a polar coordinate system,  $I_0$  and  $I$  the inclinations of the magnetic core field and magnetization and,  $D_0$  and  $D$  the declinations of the magnetic core field and magnetization respectively. If the remnant magnetization can be neglected, equation 4.1 reduces to

$$F(\theta) = 1/[i \cos I_0 \cos(D_0 - \theta) + \sin I_0]^2 \quad (4.2)$$

Equation (4.2) shows that the imaginary and real part of the function  $F(\theta)$  becomes very high when  $I_0$  is close to 0 and  $\theta$  close to  $D_0$ . The filtering function becomes undefined at the magnetic equator and when  $\theta = D_0 \pm 90$ . Furthermore, the signal would be hugely amplified along the direction of  $D_0$  near the magnetic equator.

The noise level along this direction would be inevitably magnified which makes the frequency domain RTP method unstable near the magnetic equator.

Secondly, it is problematic to implement the FFT filtering in a spherical coordinate system. Frequency domain methods, especially FFT, are well suited for rectangular Cartesian grids. But the sphericity of the earth must be taken into account for large regional data. Therefore, geophysical data on a spherical surface, in spherical coordinates, does not meet the requirements for the application of the FFT.

Thirdly, the RTP transformation in equation (4.2) requires a constant geomagnetic inclination  $I_0$  and declination  $D_0$  over the whole area, which makes it problematic to apply the RTP filter to a large-scale area where the geomagnetic inclination and declination are variable.

Thus, the frequency domain RTP transformation is only suited for small, rectangular grids where the geomagnetic inclination and declination can be considered constant.

For continental-scale or even global implementation of RTP transformation, the 2-step inversion-forward calculation method is a more acceptable method, despite being computationally expensive. The first step is to obtain magnetic parameters of equivalent layer dipoles, which can explain the input magnetic field (see appendix B for details about inversion method). The second step is to forward calculate the field with respect to the new main field direction which is artificially pointed vertically downward or upward at each equivalent dipole point.

### 4.3. Results

#### 4.3.1. Test inversion for local area

One of the main problems of a regional magnetic inversion is the magnetic effect of the surrounding area near the boundary, called edge effect. Usually the magnetic effect of the surrounding area in our study area is unknown. Thus, we cannot subtract this effect from the observation data in the target area. Therefore, the far field or edge effect acts as a perturbation to the observation data. To reduce this effect, the conventional approach is to extend the target area to keep the original target area less disturbed.

To select efficient boundary extension conditions a 2° global equivalent dipole layer was inverted to demonstrate the edge effect for a local area. 5°, 10° and 15° boundary extension were tested to Australia in order to calculate the edge effect in a local inversion. For these 3 cases, an equivalent layer was placed at 30 km depth and input data were forward calculated from the 2° global inversion model. Describing this in a linear system  $Ax=b$ , the right side is the magnetic effect of all the sources outside the inversion window over Australia. Then inversion results within the extended area were removed so that the far field effect in the inversion for our target area were comparable for three different boundary extension conditions. Figure 4.2 shows the estimation of the far field effect for the three boundary conditions. There is not fundamental difference in the far field effect patterns between the three cases except a difference in the north and north-east part of the maps. This suggests that although the extension of the boundary could not eliminate the far field effect, it can be reduced to some extent.

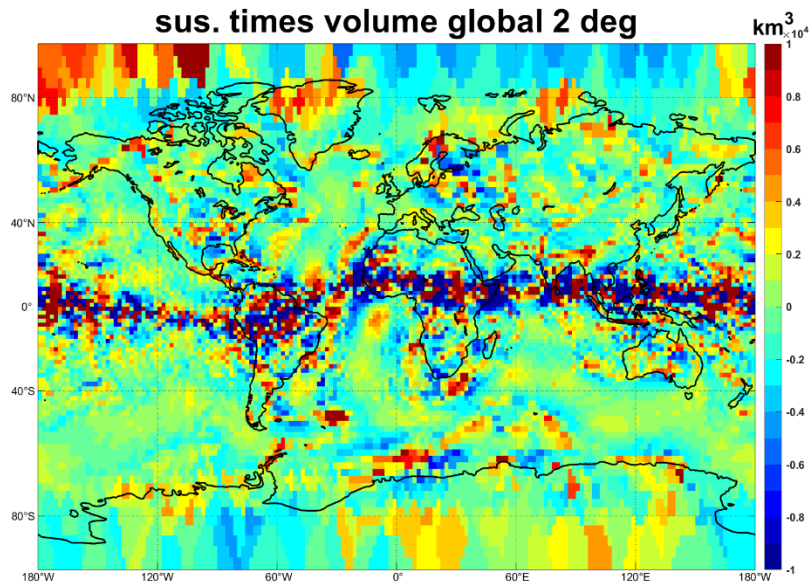


Figure 4.1: Global 2° inversion of susceptibility times volume

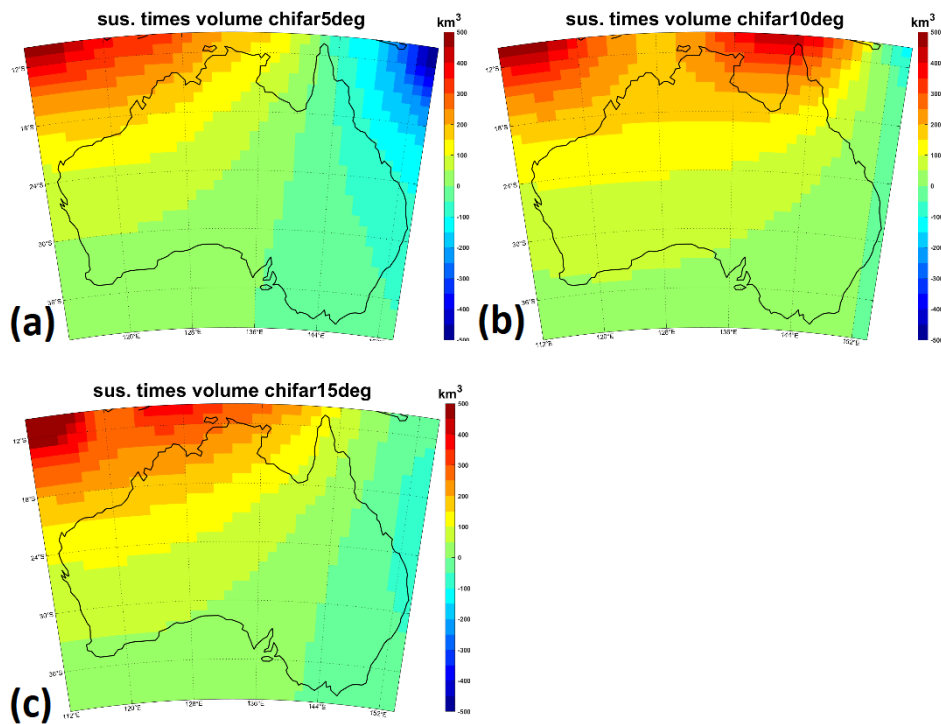


Figure 4.2: Far field effect in local inversion for different extensions: (a) 5°, (b) 20°, (c) 15°.

Three different resolutions (1°, 0.5° and 0.3°) with 10° extension were tested using the LCS1 model as input data over Australia (Table 4.1) to find out an acceptable resolution and extension for the regional inversion.

The equivalent dipole layer was placed at 30 km beneath the surface. The input data was Bz component of the LCS1 model at 5 km. The inverted dipoles were recalculated at 5 km and 400 km to compare with the LCS1 model's Bz components respectively.

Table 4.1: misfit map of predicted Bz component and LCS-1 Bz component at 5km and 400km height

misfit model geometry	Misfit between LCS-1 Bz component and predicted Bz @5km	Misfit between LCS-1 Bz component and predicted Bz @400km
1° resolution with 10° extension	<p>residual @5km</p> <p>nT</p>	<p>residual @400km</p> <p>nT</p>
0.5° resolution with 10° extension	<p>residual @5km</p> <p>nT</p>	<p>residual @400km</p> <p>nT</p>
0.3° resolution with 10° extension	<p>residual @5km</p> <p>nT</p>	<p>residual @400km</p> <p>nT</p>
0.3° resolution with 15° extension	<p>residual @5km</p> <p>nT</p>	<p>residual @400km</p> <p>nT</p>

As we can see from Table 4.1, inverted dipoles can explain the data at 5 km but fail to fit the data at 400 km for a 1° resolution. If the resolution was increased to 0.5°, there was still a systematic misfit between the LCS1 Bz component and the predicted data, but with a decreased residual. Dipoles with 0.3° resolution almost equally good fitted the magnetic data both at near surface and satellite altitude. It also suggests that a 15° extension did not further minimize the residual.

To summarize, several test inversions were carried out to demonstrate the influences of the source spacing and the boundary extension. For a local inversion, a target window of 112°W, 154°E, -30°S, -10°N was selected to demonstrate these 2 factors. The equivalent dipole sources were placed at 30 km beneath the surface and input data were at 5 km above the earth surface.

Firstly, extension of the target area can reduce the edge effect but cannot eliminate the far field effect. For three different boundary extension cases, the far field effect introduces similar patterns to the inversion results. Although an increase in boundary extension could reduce the overall far field effect in the target area, a moderate increase in boundary extension may be sufficient in terms of accuracy and calculation cost. The 5° extension also could be a good choice for the target area that agrees well with the far-field effect for gravity data ([Szwilius et al. 2016](#)). However, it may be not enough for other areas near the equator. The limitation of the 5° extension will be shown for tile-wise global inversion (section 4.3.2).

Secondly, a high resolution of the sources helps to maintain the long wavelength and short wavelength information from the input data. With 0.5° and 1° spacing of the dipole sources the predicted results at satellite altitude systematically differ from the satellite data, although the inverted models fit the satellite data very well at 5 km height. For a 0.3° resolution inversion, the largest misfits only occurred in the extended area and the misfit in the target area was relatively small. This suggests that source spacing less than 0.3° can preserve the magnetic information from the LCS-1 model both from near-surface altitude to satellite height.

Therefore, it was decided to use 0.25° resolution and 10° extension for the global RTP.

#### 4.3.2. Global tile-wise inversion

As first step of our RTP transformation a tile-wise inversion scheme was adopted to deal with the global inversion problem. The entire globe was divided into 240 patches with a 15° by 15° size and two 15° polar caps. Each of them had a 10° extension on each edge. The equivalent dipole layer was located at 30 km beneath the surface to follow the average Moho depth of the continental crust. An equal area sphere partitioning algorithm ([Leopardi 2006](#)) was used to distribute the source dipoles with equal distance since a regular grid in spherical coordinates results in a dense grid point distribution near the

poles. This would increase singularity of the sensitivity matrix. The total number of dipoles was 662409 with an average distance between adjacent sources of  $0.25^\circ$ .

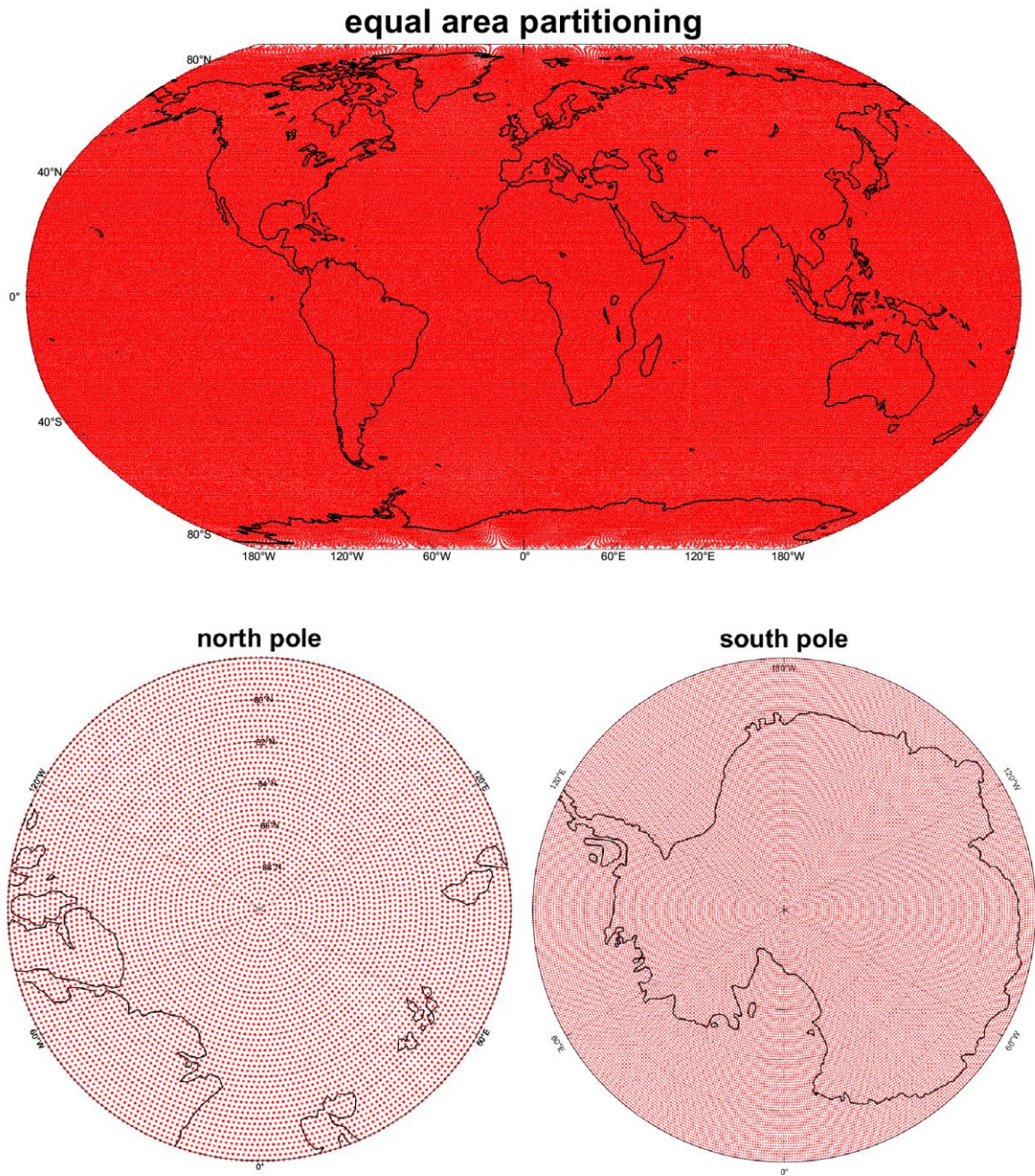


Figure 4.3: Equal area partitioning

The global tile inversion result had some gaps along the equatorial area because the inversion method failed to converge in these areas (Figure 4.4).

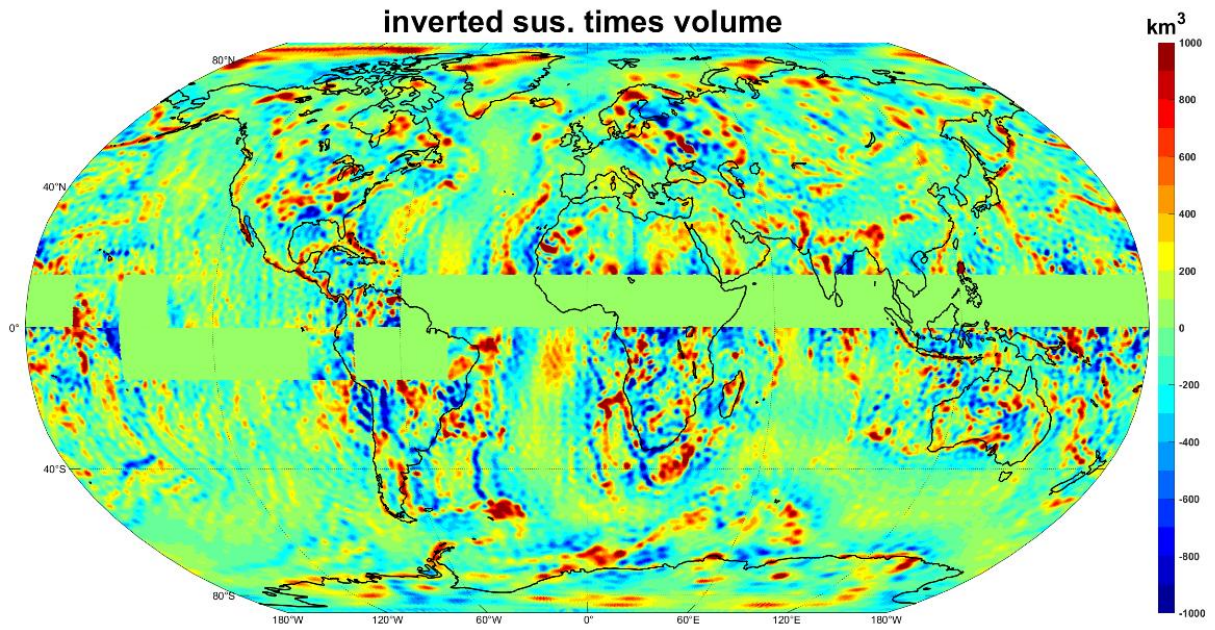


Figure 4.4: Global tile-wise inversion result of  $15^\circ$  by  $15^\circ$  tiles with  $10^\circ$  extension. The iterative inversion method stagnated along equatorial areas due to the high condition number of the sensitivity matrix so that inversion resulted in initial guess of zero.

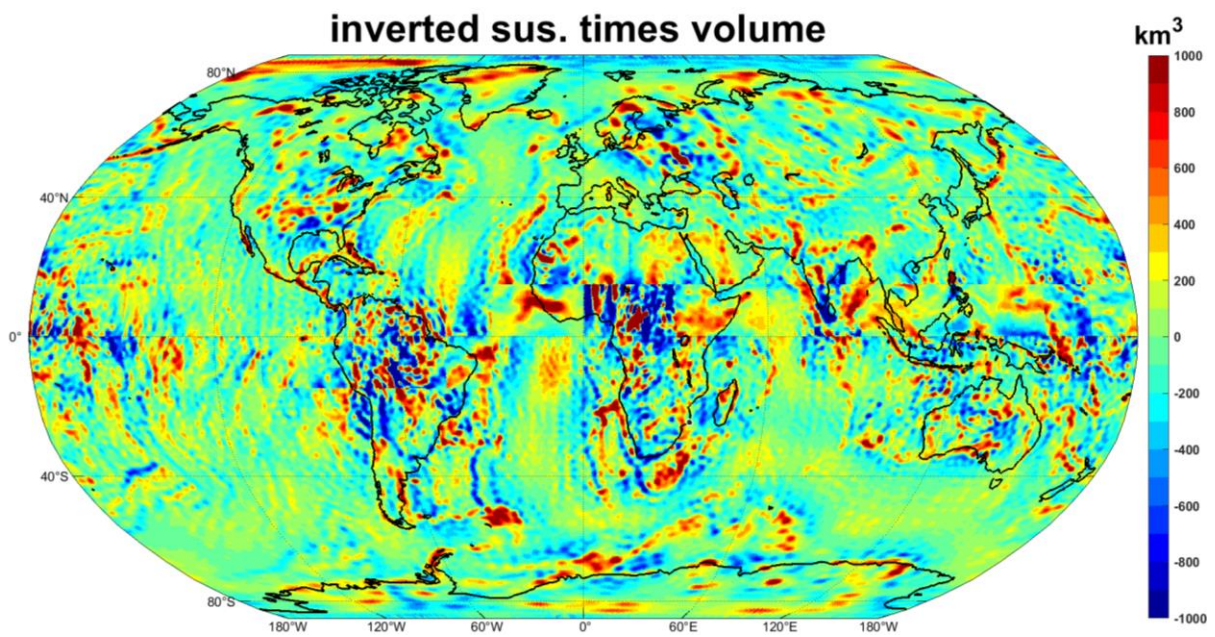


Figure 4.5: Global tile-wise inversion result of  $15^\circ$  by  $15^\circ$  tiles with  $10^\circ$  extension (boundary extension reduced to  $5^\circ$  for areas where inversion resulted in initial guess of zero in Figure 4.4)

If the boundary extension for these areas was decreased from  $10^\circ$  to  $5^\circ$ , we can fill the gaps with high misfits (Figure 4.5 and Figure 4.6).

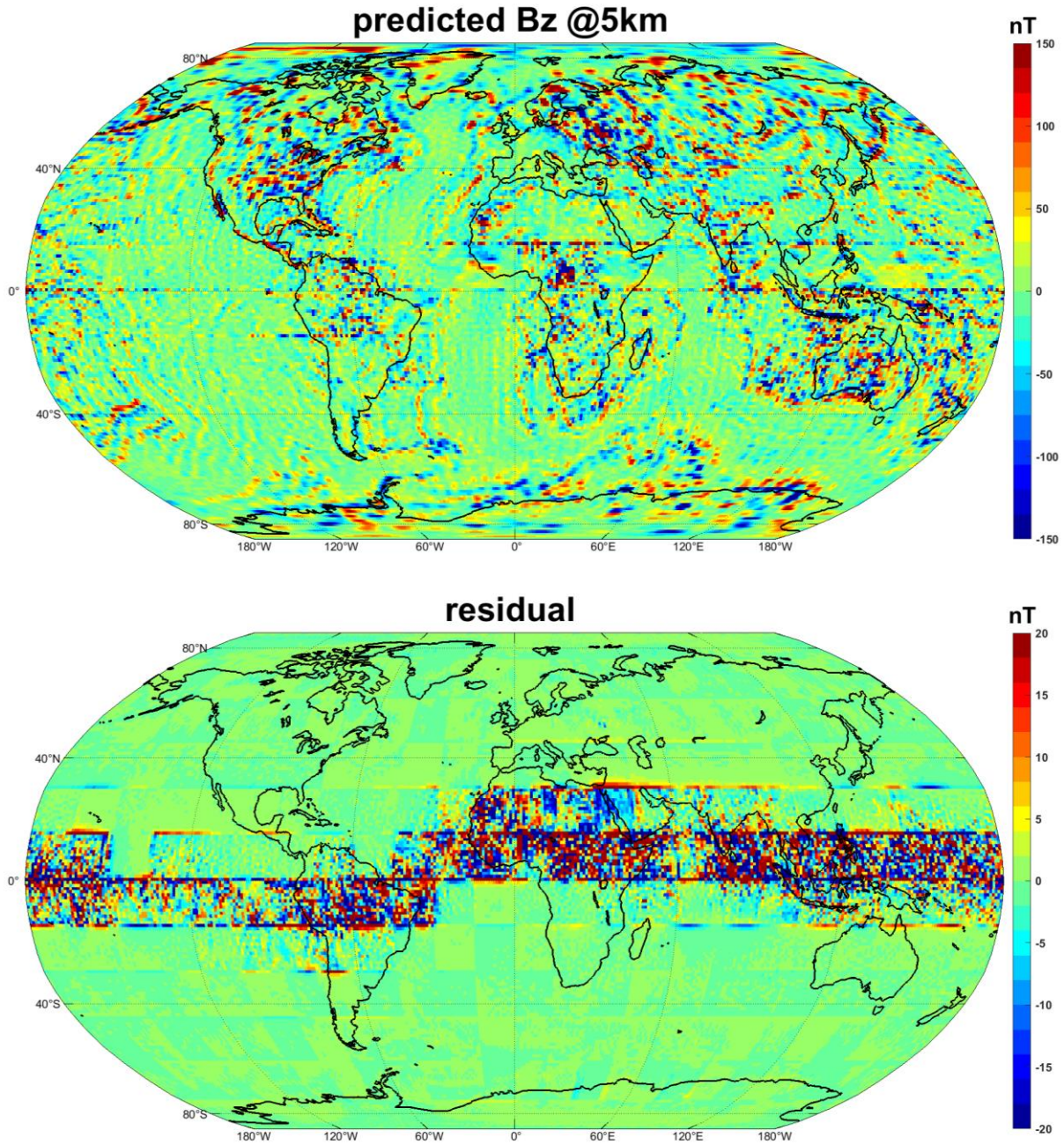


Figure 4.6: Predicted Bz component and misfit in 1° resolution at 5 km. Predicted field was forward calculated from the inversion result of Figure 4.5.

To show the uncertainty which is introduced by the insufficient boundary extension of 5°, the predicted Bz component was calculated using the inverted magnetic parameters from Figure 4.5. The 1° resolution forward calculated Bz field shows this introduced error in the equatorial area. The predicted field at satellite height also shows the same feature. As seen from Figure 4.7, it is obvious that misfit correlates with the magnetic inclination. The main part of the high misfit is in the close envelope of the magnetic inclination of  $\pm 30^\circ$ , following the magnetic equator.

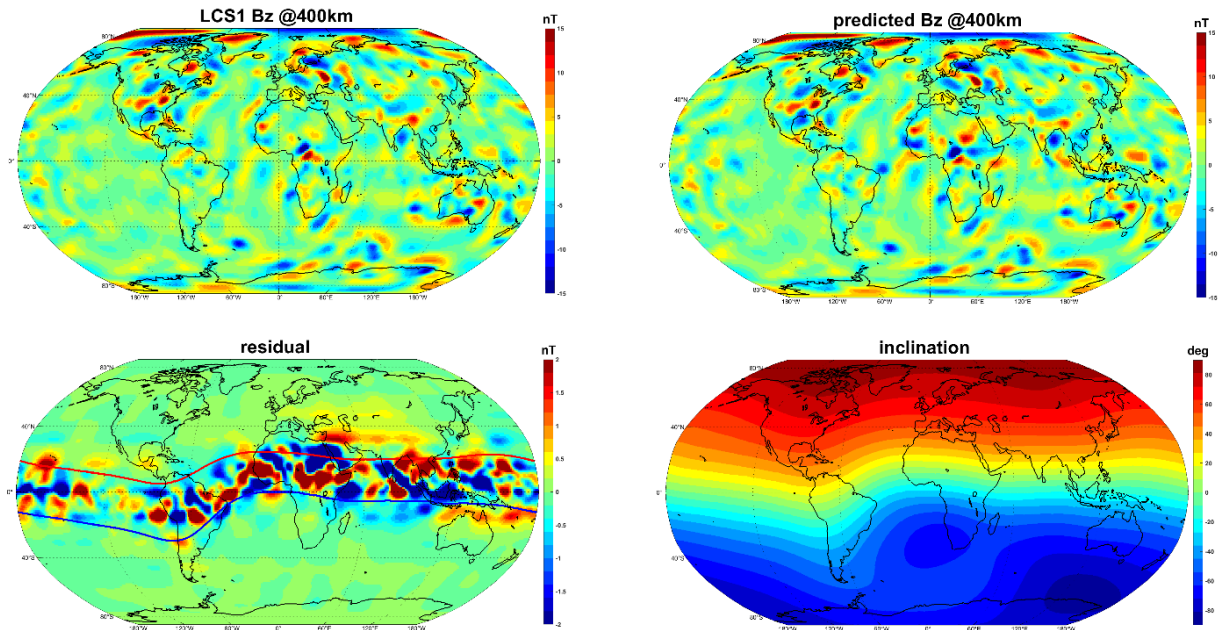


Figure 4.7: Predicted data and misfit in 1° resolution at 400 km and the core field inclination. Predicted field was forward calculated from the inversion result of Figure 4.5.

Therefore, a 5° extension for the equatorial areas is not a suitable way to deal with the inversion problem. Because the small inclination around the equatorial areas increases the condition number of the sensitivity matrix so that the iterative inversion method becomes unstable and fails to converge. To mitigate this effect, the iterative inversion method was applied to the normal equation which is  $A^T A x = A^T b$ . Thereby, stagnation of the iterative inversion method around the equatorial areas can be avoided (see appendix B). Finally, it led to more continuous result than the inversion of original linear system (Figure 4.8).

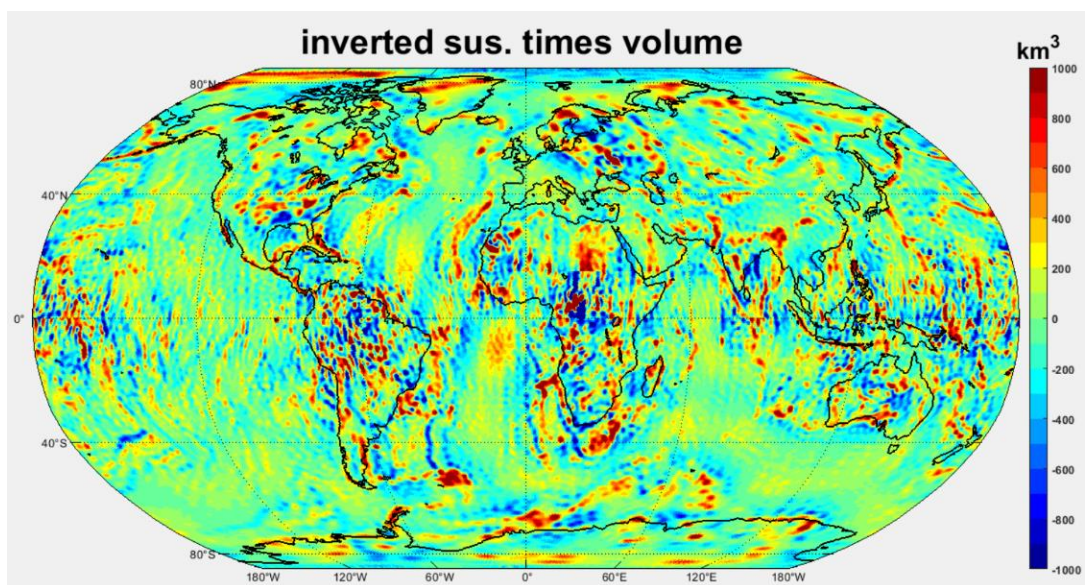


Figure 4.8: Global tile-wise inversion result of 15° by 15° tiles with 10° extension. The iterative inversion method was applied to the normal equation  $A^T A x = A^T b$ .

Figure 4.9-Figure 4.11 show that misfit of the inverted model has been significantly decreased. The main body of the misfit appears along the tiles' boundary.

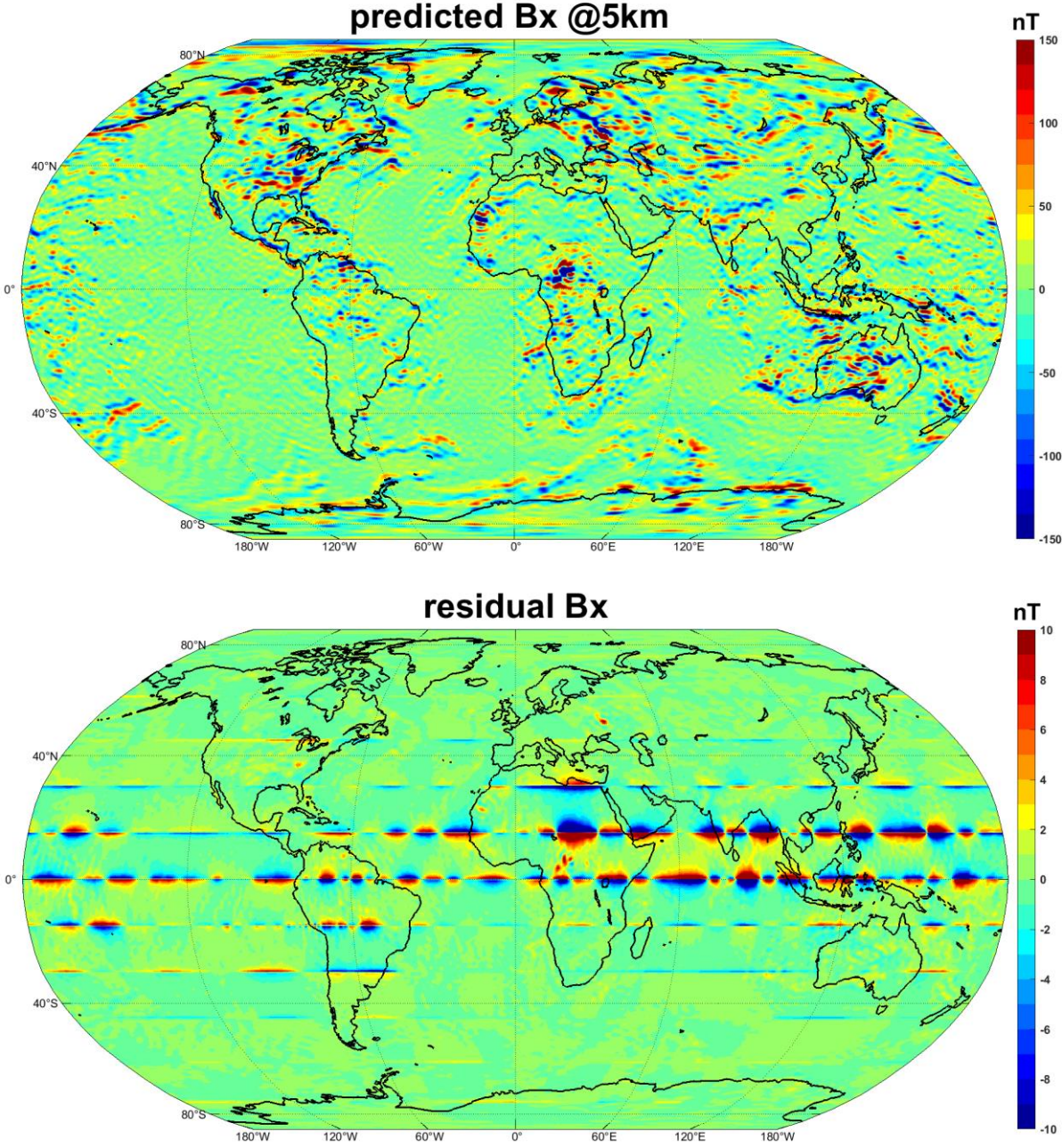


Figure 4.9: Predicted field Bx and misfit at 5 km (with preconditioner)

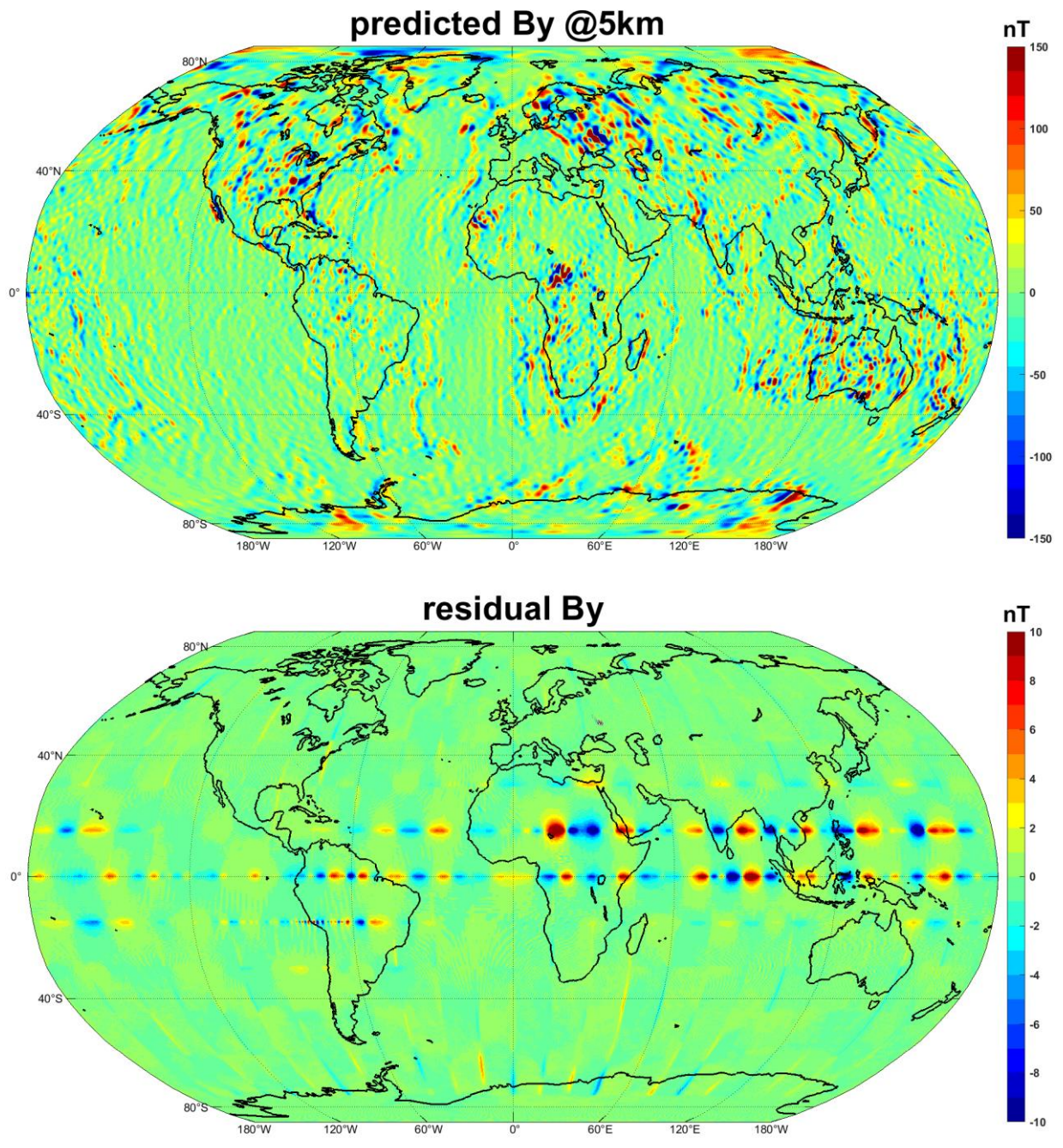


Figure 4.10: Predicted field  $B_y$  and misfit at 5 km (with preconditioner)

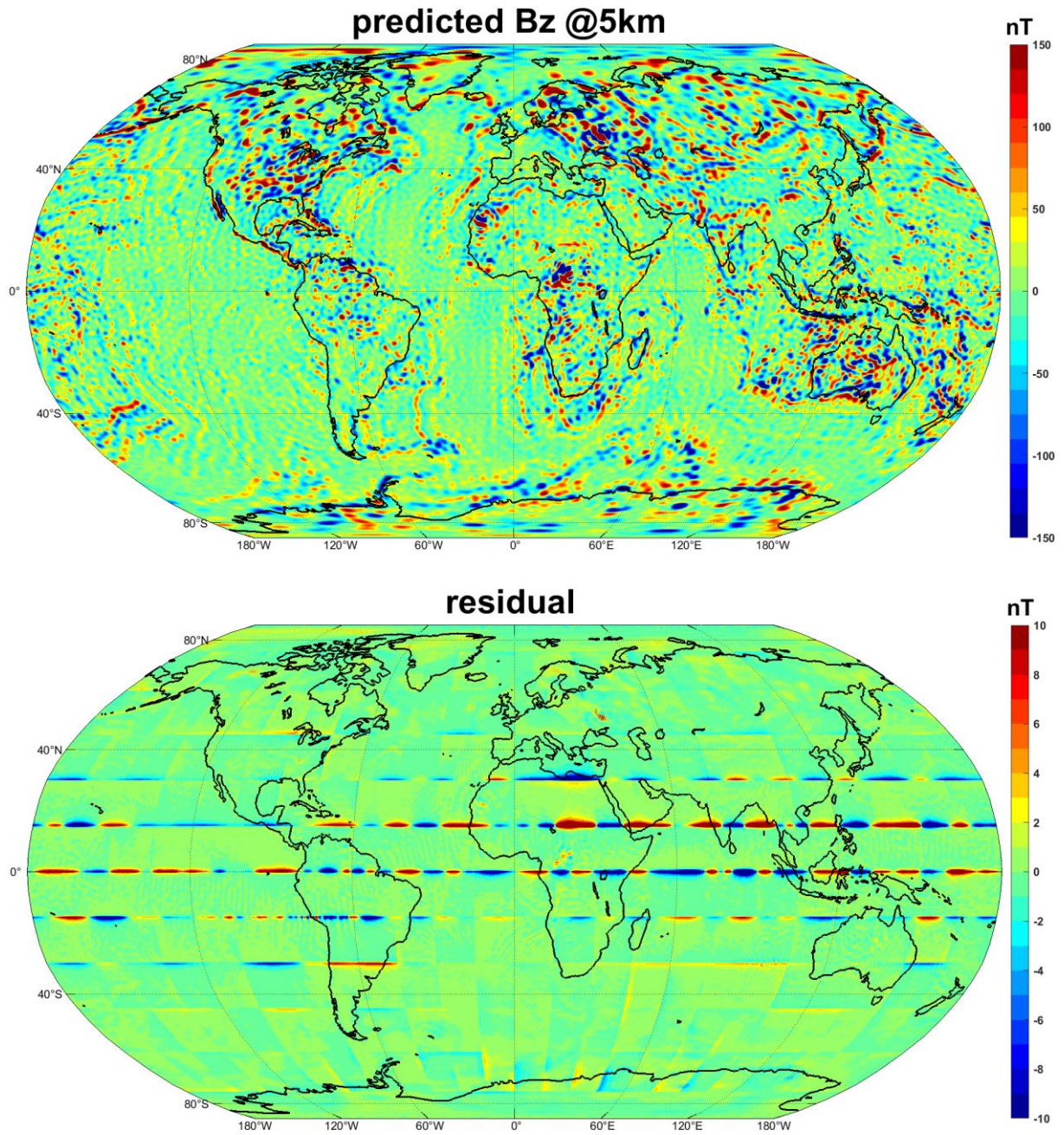


Figure 4.11: Predicted field Bz and misfit at 5 km (with preconditioner)

According to the preconditioned inversion result, the RTP transformation leads overall to sufficient results with slight distortions around the tile boundaries.

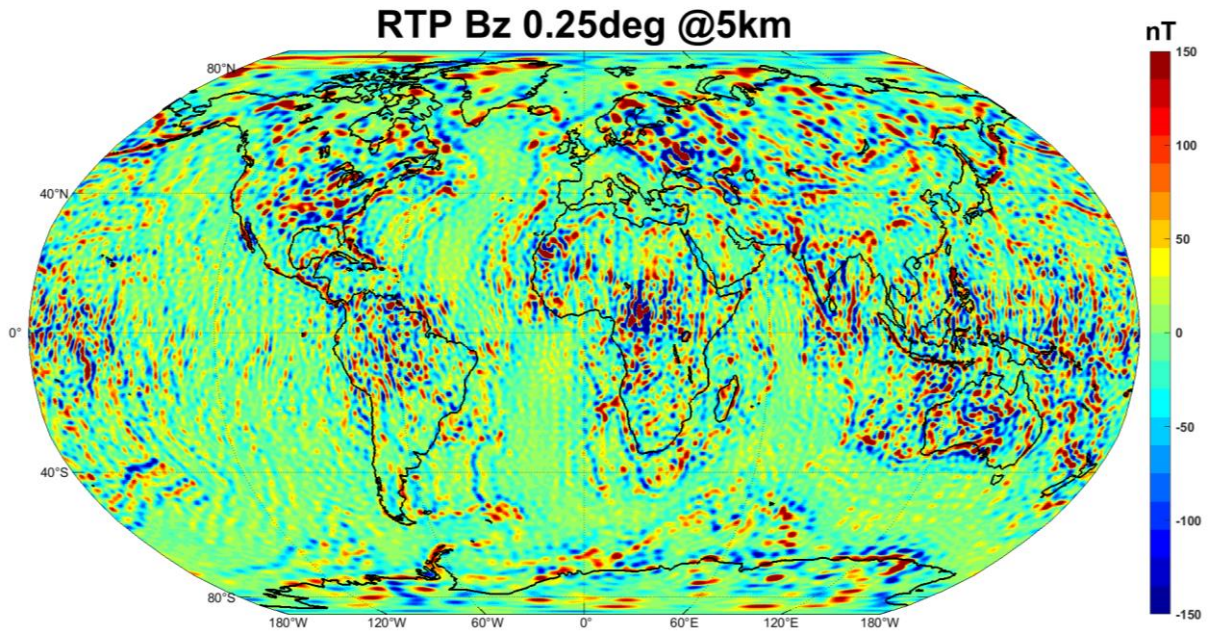


Figure 4.12: RTP transformation of LCS-1 at 5 km

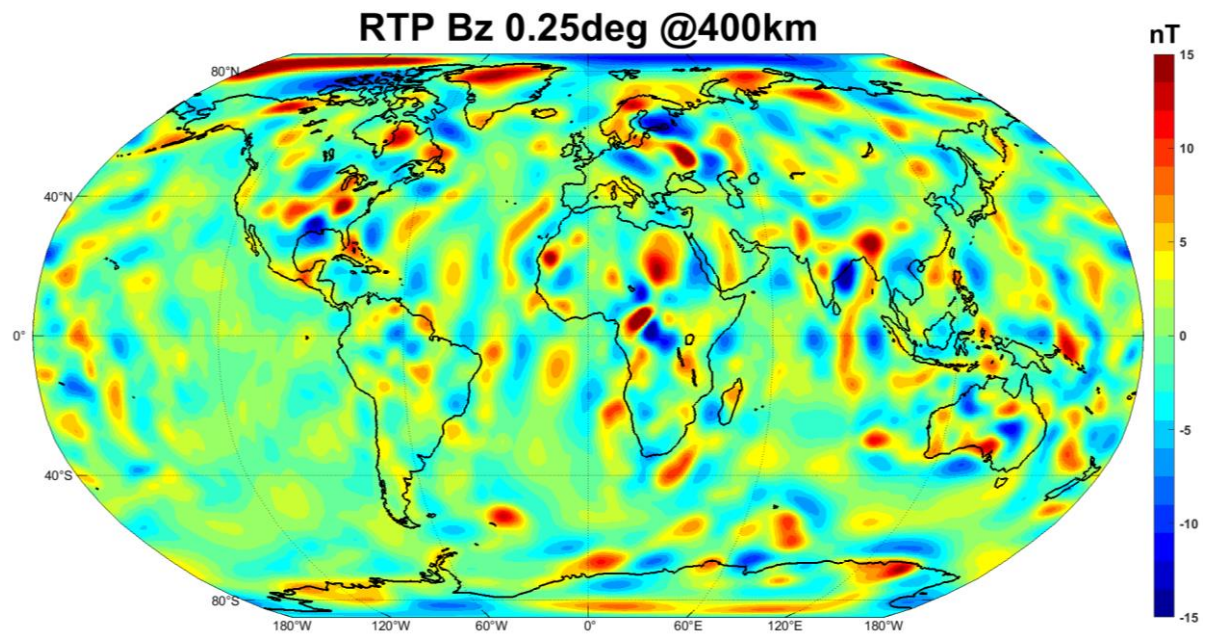


Figure 4.13: RTP transformation of LCS-1 at 400 km

#### 4.4. Conclusion

The reduction to the pole transformation for LCS-1 satellite data was calculated globally with a  $0.25^\circ$  resolution. The forward calculated field from the inversion result shows that the inverted magnetic parameters can explain the magnetic data from LCS-1 quite well except for the tile boundaries along the equator. The general patterns of the input LCS-1 Bz field and its RTP transformation at 5 km height are similar in higher latitude areas. However, some north-south orientated structures have been amplified by the RTP transformation around the equatorial area. It also suggests that the vast majority

of the north-south orientated structures along the equator is probably the amplified data misfit rather than true signal. Leaving aside the near equatorial areas, the RTP data associated with higher latitudes should be reliable. Together with Chapter 3, the RTP data provide a mainstay in linking the ancient neighbouring continents in a Gondwana framework.

Following the definition of the pseudo-gravity, the pseudo-gravity transformation can be carried out using the same magnetic parameters of the equivalent source layer. Although the inverted magnetic parameter is not physically meaningful susceptibility, it can serve as pseudo-susceptibility and together with the pseudo-gravity transformation, they can assist in inferring of large-scale sub-surface geological structures.

# East Antarctica magnetically linked to its ancient neighbours in Gondwana

Jörg Ebbing<sup>1</sup>, Yixiati Dilixiati<sup>1</sup>, Peter Haas<sup>1</sup>, Fausto Ferraccioli<sup>2,3</sup>, Stephanie Scheiber-Enslin<sup>4</sup>

<sup>1</sup> Institute for Geosciences, Kiel University, Kiel, Germany

<sup>2</sup> OGS, Trieste, Italy

<sup>3</sup> British Antarctic Survey, Cambridge, UK

<sup>4</sup> Witwatersrand University, Johannesburg, South Africa

Published in: *Scientific Reports* 11, 5513 (2021); <https://doi.org/10.1038/s41598-021-84834-1>

## 5.1. Introduction

Defining the architecture of the lithosphere under the thick ice cover of Antarctica is of wide interest as large parts are still blanks on geological maps (Figure 5.1 and recent Gondwana map by [Murthy 2017](#)). Novel methods and data are needed to enhance our current knowledge and link the geology from the few outcrops at the coast to that under the ice ([Kennicutt et al. 2019](#); [Stål et al. 2019](#)). For example, in a recent study, heat-flow values from the formerly adjacent neighbours were interpolated into East Antarctica, deriving a map significantly different from previous interpretations ([Pollett et al. 2019](#)). A second study uses a set of geophysical data and models to define lithospheric domains in East Antarctica by statistical analysis ([Stål et al. 2019](#)). Both these statistical methods in their simplicity provide new insights, but have limitations, mostly due to the sparse coverage of data used.

Magnetic data collected over the last 50 years, although with varying resolution and accuracy, covers Antarctica and its ancient continental neighbours. Previous studies have shown that magnetic data, especially when interpreted jointly with geochronological, geochemical, geophysical and palaeomagnetic datasets, helps identifying fundamental links between formerly adjacent neighbours within the Gondwana, Rodinia and Columbia supercontinents ([Müller et al. 2019](#); [Swanson-Hysell et al. 2015](#)). These links are highly relevant for global supercontinent studies as current plate reconstructions still vary considerably, both in terms of defining the relative positions and the tectonic processes that affected different continents.

In this context, Antarctica has a special role as it holds a key position in a Gondwana framework ([Boger 2011](#); [Ferraccioli et al. 2005](#); [Li et al. 2016](#)) but its geology is mostly hidden under its thick ice cover. Therefore, reconstructing the position of Antarctica helps to extrapolate the geology from the former

adjacent neighbours. For example, such reconstructions were used to discuss the structural setting of East Antarctica with respect to the setting of Southern Australia and showed that the magnetic data indicate the continuation of the Australian geology under the ice of Antarctica ([Finn et al. 1999](#); [Aitken et al. 2014](#); [Aitken et al. 2016](#)). That link between Antarctica and Australia has been studied in detail using aeromagnetic data of comparable quality. Studies on the link between Antarctica and Southern Africa, however, have often had a focus on Dronning Maud Land on the Antarctic side or relied on low-quality global magnetic compilations outside Antarctica ([Mieth and Jokat 2014](#); [Mieth et al. 2014](#); [Mueller and Jokat 2019](#)). Similar observations can be made for the link between India and Antarctica, which has been studied albeit without using magnetic data ([Veevers 2009](#)). A reason for this is that aeromagnetic data for the Indian subcontinent are not openly available and in state-of-the-art global compilations models like EMAG2v3 ([Meyer et al. 2017](#)) are indicated to be of low quality.

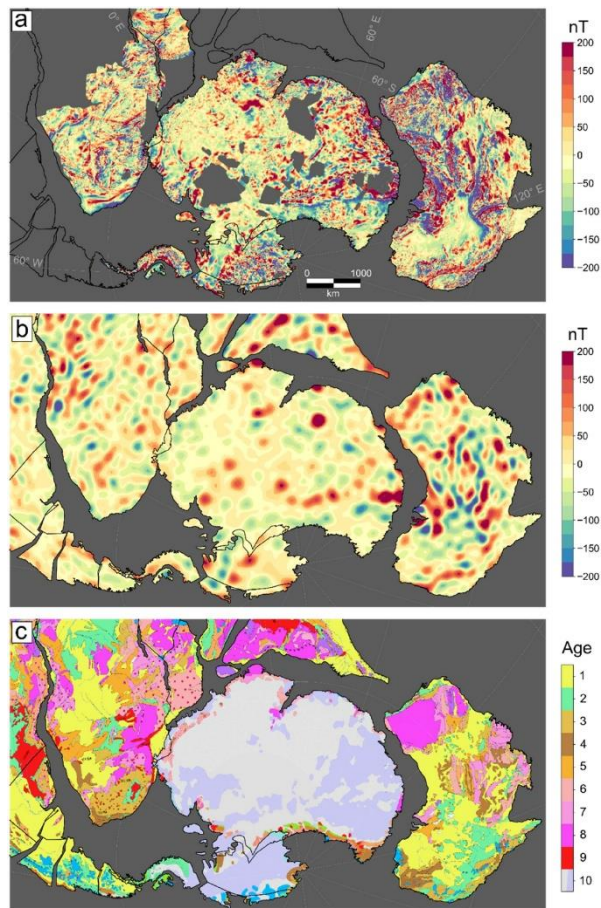


Figure 5.1: (A) Conformed aeromagnetic data, (B) Satellite model LCS-1 after variable reduction to the pole, represented at 5 km height. (C) Surface geology as represented in the Geological Map of the World ([Bouysse 2010](#)). The geological of the units are: 1: Cenozoic, 2: Mesozoic, 3: Upper Paleozoic, 4: Lower Paleozoic, 5: Neoproterozoic, 6: Mesoproterozoic, 7: Paleoproterozoic, 8: Archean, 9: Large Igneous Provinces, 10: Glaciers and Ice. For more details, see ([Bouysse 2010](#)). All data sets are rotated back to 200 Ma with the deformable plate model of [Müller et al. 2019](#).

Resolution and accuracy are in general an issue when using global magnetic anomaly compilations to derive tectonic interpretations and supercontinent linkages. For example, EMAG2v3 has a nominal resolution of 2 arc-minutes, but data content is highly heterogeneous over the globe. That relates to accuracy and resolution, but also the treatment of the long-wavelength content that is notoriously unreliable. The maximum wavelength contained in any dataset is limited by the survey extent and often one refers to a spectral gap between satellite and aeromagnetic data. To address this spectral gap, in Australia a number of long-haul flight lines had been acquired ([Minty et al. 2003](#); [Milligan et al. 2004](#); [Franklin and Milligan 2010](#)). Still, the long-wavelength range in the most recent release has been replaced by satellite data due to their increased accuracy. A number of studies have made use of recent releases of the satellite lithospheric magnetic field to replace the long-wavelength part of aeromagnetic surveys with satellite data ([Olesen et al. 2010](#); [Gaina et al. 2011](#)). For example, in the Circum-Arctic region, the long-wavelength aeromagnetic data were replaced with satellite data using a cut-off filter of 400 and 330 km ([Gaina et al. 2011](#)). This cut-off relates to the maximum spatial resolution of the early generation of satellite models ([Maus et al. 2005](#); [Maus et al. 2008](#); [Olsen et al. 2017](#)) and corresponds to the maximum reliable wavelength of typical aeromagnetic surveys.

The resolution of satellite-derived magnetic field models is limited by the orbit height, instrumentation and mission period. Since 2013, the Swarm satellite mission from the European Space Agency has been continuously measuring the Earth's magnetic field. The mission consists of three-satellites at different altitudes and with changing orbit inclinations ([Olsen et al. 2017](#); [Thébault et al. 2016](#)). The addition of these data to the data from previous satellite missions (e.g. CHAMP, Oersted) helps to increase spectral accuracy and appears in the Swarm-derived lithospheric field model LCS-1 providing reliable wavelengths in some regions to 250 km ([Olsen et al. 2017](#)). However, in Polar Regions, the noise in satellite data is greater than at mid-latitudes ([Lesur and Maus 2006](#)). Due to the increased noise, the lithospheric field estimates are less accurate for wavelengths larger than 300 km wavelength.

Here, we conformed the available aeromagnetic compilations for Antarctic and its neighbouring continents Australia and Southern Africa to satellite data. This process results in a homogeneous data representation across the heart of Gondwana. We discuss the value of the conformed data and the satellite data itself by linking up anomalies between Southern Africa, Australia and East Antarctica. In addition, we look at the satellite data link to India to its Antarctic counterpart.

## 5.2. Conforming satellite magnetic and aeromagnetic data

To illustrate the different steps in homogenising the aeromagnetic data, we choose the area of Southern Africa (Figure 5.2). Two aeromagnetic grids cover the area of South Africa, one made publicly available in 2000s ([Stettler et al. 2000](#)) and the second, an updated version, released in 2019 ([Council for Geoscience 2019](#)). In the original compilation a difference in the main level of  $> -100$  nT can be

observed between South Africa and its northern African neighbours (Figure 5.2A), while in the latest release South Africa is shifted by  $\sim +50$  nT (not shown here).

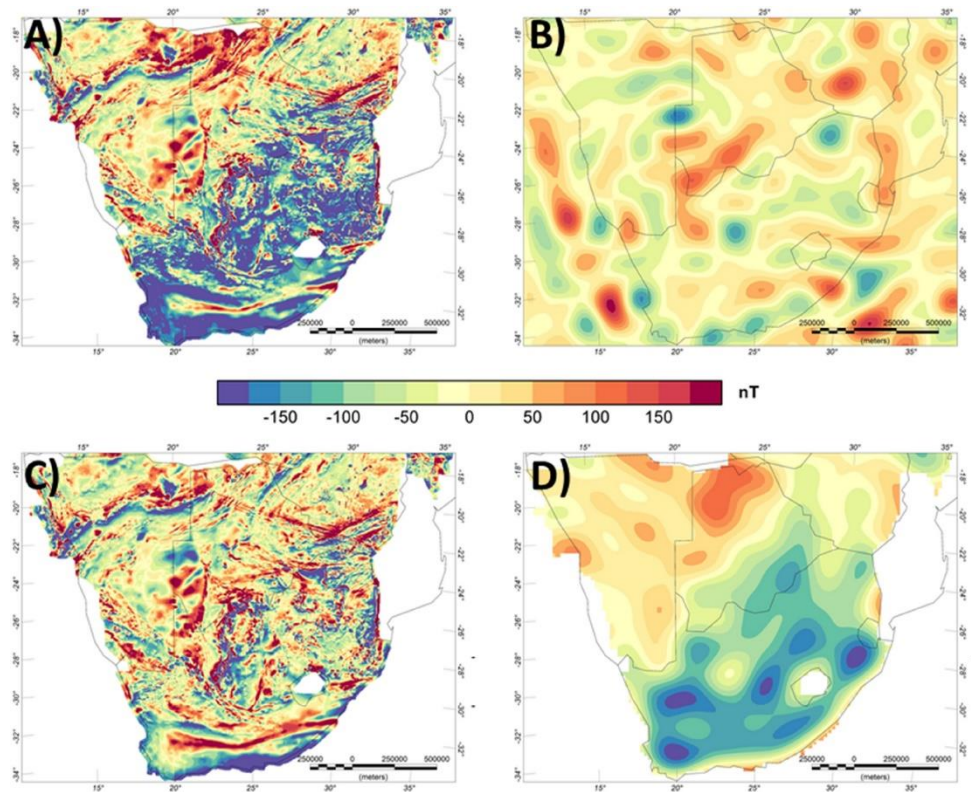


Figure 5.2: Lithospheric magnetic anomaly of Southern Africa. (A) Original aeromagnetic compilation ([Stettler et al. 2000](#)), (B) Satellite-derived model LCS-1, (C) Conformed aeromagnetic and satellite model. (D) Difference of (A, C).

The difference in the level could be misinterpreted as reflecting fundamental variability in crustal-scale geology or thermal state. E.g. the long to mid wavelength field is often used to estimate the Curie isotherm ([Martos et al. 2017](#)), but can also relate to differences in crustal architecture ([Ebbing et al. 2009](#)), upper mantle magnetization ([Idoko et al. 2019](#)) or a combination of thermal and structural properties ([Milano et al. 2019](#)). For this area, the pattern partially correlates with some of the main tectonic features of the area such as the boundaries of the Kaapvaal Craton to its surrounding. An indication, that this feature here is instead an artefact of processing comes from the fact that the shift values for the two generations of compilation have an opposite sign.

Therefore, we replace the long-wavelength part of the original 2000s Southern Africa aeromagnetic compilations with the satellite model LCS-1 (Figure 5.2B). For this, we use an equivalent layer approach and replace the data up to spherical harmonic degree 130 (corresponding to  $\sim 300$  km wavelength) with satellite data (see Data and Methods for more details). The resulting conformed grid is spectrally consistent and still contains the high-frequency information of the original compilation.

The long-wavelength part of the aeromagnetic compilation, if accurately estimated, is expected to be similar to satellite derived data. However, the long-wavelength part shows differences of more than -100 nT for South Africa and considerably less differences for the countries to its north as can be seen in the correction applied to the data (Figure 5.2D).

As mentioned, for South Africa, an updated aeromagnetic grid is as well available ([Council for Geoscience 2019](#)), having an apparent higher resolution, due to the inclusion of more recent surveys, and with an opposite sign shift of 50 nT for the long-wavelength in South Africa. Conforming this grid to the satellite model results again in a long-wavelength trend correction and in a homogenous anomaly map that still reflects the major crustal domains of Southern Africa.

We applied the same procedure to the Australian and Antarctic datasets (see Data and Methods). For Australia, the differences in the long-wavelength range are relatively small. The differences result from the use of a different satellite model as compared to original Australian compilation, where the long-wavelength part was replaced by the satellite model MF-7 ([Maus et al. 2008](#)). Here, we replace instead the long-wavelength components with the more recent LCS-1 model for improved consistency between the compilations for the individual continents we examined.

More interesting are the differences for Antarctica. For the ADMAP-2 compilation all surveys have been corrected for the same geomagnetic reference model, but no correction for satellite data has been applied ([Golynsky et al. 2018](#)). Nevertheless, the long-wavelength component of ADMAP-2 still corresponds very well with the satellite-derived model. Conforming the Antarctic aeromagnetic compilation to the satellite model leads to sharpening of some anomalies with the main differences between satellite and aeromagnetic data in the long-wavelength range being correlated to the line density and general data coverage (Figure 5.3). In areas where the aeromagnetic data coverage is denser, the location of the anomalies are similar, but shapes and extents may vary.

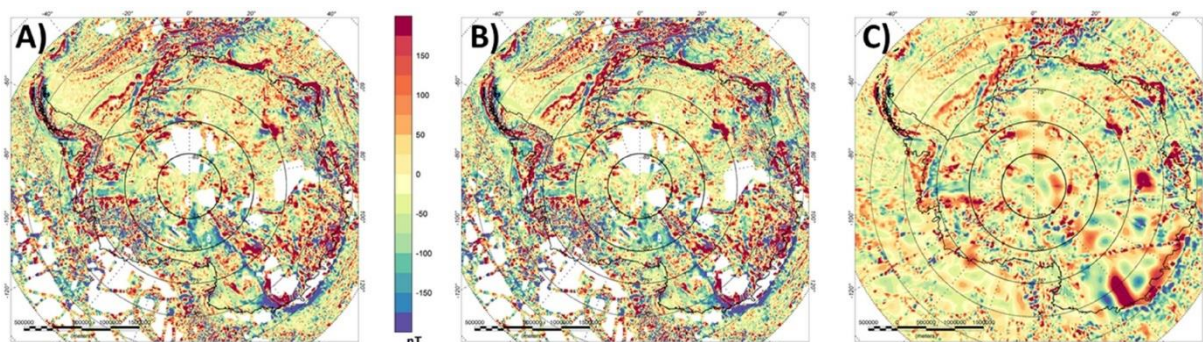


Figure 5.3: Lithospheric magnetic anomaly for Antarctica. (A) Original ADMAP-2 compilation ([Golynsky et al. 2018](#)). (B) After conforming ADMAP-2 to the satellite model LCS-1. (C) EMAG2v3 ([Meyer et al. 2017](#)).

Unfortunately, not all of the continents surrounding Antarctica, have aeromagnetic compilations in the public domain, e.g. India. Therefore, one might consider using data from global compilations to fill the

gaps. In Figure 5.3, we compare the conformed satellite-aeromagnetic anomaly map to the global model EMAG2v3 for Antarctica. The comparison shows that most of the details seen in our satellite-corrected aeromagnetic data compilation are less clear in the global compilation. EMAG2v3 comes with a data quality measurement that shows the dataset does not contain consistent high-quality measurements for this area. It is evident that EMAG2v3 is only a smoothed representation of the aeromagnetic datasets and some of the linear features appear blurred and do not show the strike directions.

For India, the quality of the data in EMAG2v3 is even worse ([Meyer et al. 2017](#)) and hence any correlation of the features to East Antarctica is even more complicated. Another issue is the direction of the inducing main field. Induced magnetisation is commonly assumed to be the dominant magnetisation over the continents, while remanent magnetisation dominates over the oceanic plates ([Hemant and Maus 2005](#)). The direction and strength of the magnetic main field changes from the poles to the equator. While the strength of the field governs the amplitudes of the anomalies, the inclination of the field governs the shape and location of the anomalies. For a vertical field, the peak anomalies are located over the source body and side slopes are small. For an inclined field, a typical magnetic dipole anomaly is observed, where none of the anomalies are necessarily located directly over the source. For Polar Regions, such as Antarctica, this directional effect is often ignored, but for inclinations less than 70 degrees, the changes become more important.

While the inclination does not represent the inclination during break-up, it implies that simple reconstructions show rock formations adjacent to each other that actually have a completely different orientation in the Earth magnetic field because their magnetic field is based on the present day continent layout. The inclination in Southern Africa and Australia is around 50 degrees and increases to 90 degrees in Antarctica. India is located slightly north of the magnetic equator (where inclination is zero). Therefore, after conforming the compilations to a common satellite model, we performed a reduction to the pole considering the variable direction of the magnetic field (Figure 5.5 and see Methods section). However, this correction should consider the orientation of the magnetic field during the time of acquisition. Such information is next to impossible to retrieve for all the surveys acquired over more than 60 years. We applied the correction only to the satellite model for which a reduction to the pole (RTP) with a common datum is straight forward. Common spectral methods for reduction to the pole fail for satellite data. Instead, we calculated a RTP satellite model with an equivalent source method. This method also does not suffer from the numerical instability at the magnetic equator as Fourier-based methods do, but as it is computationally expensive was not used for the aeromagnetic data sets.

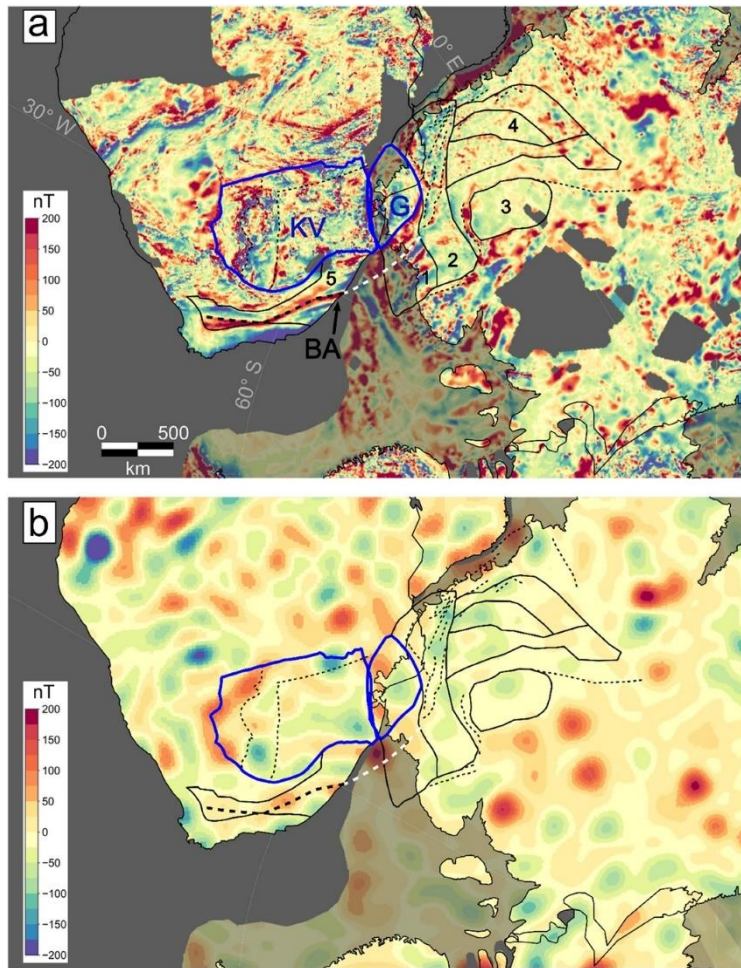


Figure 5.4: Zoom in on the South Africa-Antarctica connection. (a) Combined aeromagnetic-satellite model. The connecting cratons are marked as blue contours. KV: Kaapvaal, G: Grunehogna Craton. Beattie Magnetic Anomaly (BA) is indicated as thick dashed line. Solid black contours represent selected tectonic units of Antarctica older than 200 Ma. 1: Natal type terrane boundaries. 2: Maud Belt, 3: Valkyrie Craton, 4: Tonian Antarctic Super Terrane (TOAST). Contour 5: Natal terrane. Dashed lines indicate several fracture zones in South Africa and Dronning Maud Land, White dashed line: Continuation of the Beattie Magnetic Anomaly, (b) Satellite data LCS-1. Both data sets have been reduced to the pole and are represented at 5 km height. All data sets are rotated back to 200 Ma. Semi-transparent anomalies indicate aeromagnetic anomalies on the continental margin.

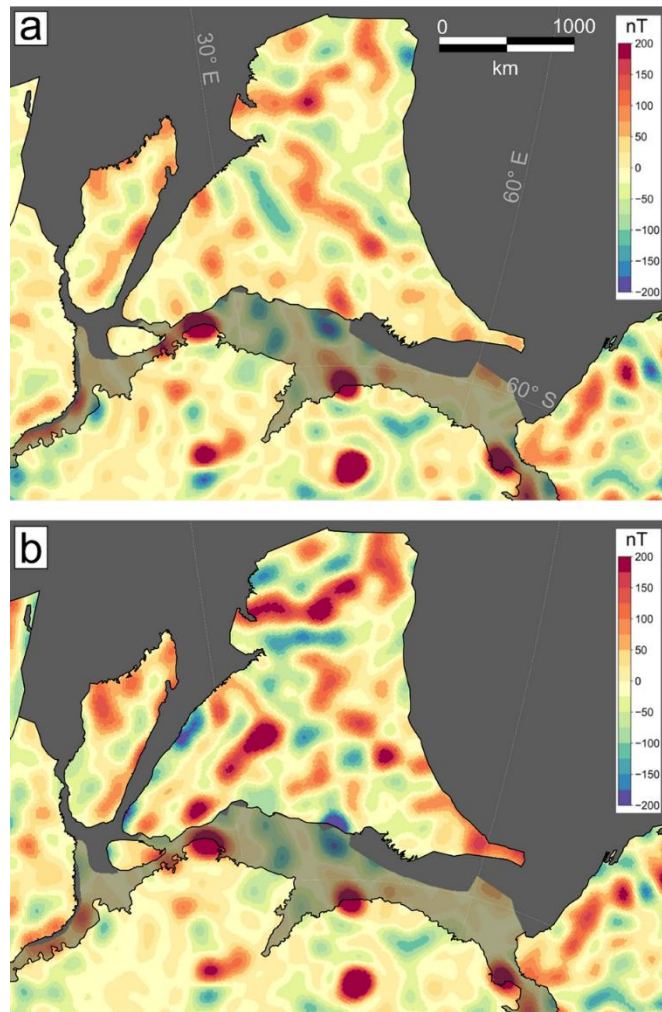


Figure 5.5: Zoom in on the India-Antarctica connection. (a) Original satellite mode LCS-1, (b) RTP corrected satellite model. Both data sets are represented at 5 km height. All data sets are rotated back to 200 Ma. Semi-transparent anomalies indicate aeromagnetic anomalies on the continental margin.

### 5.3. Discussion

Two things are of interest in interpreting the conformed aeromagnetic and satellite data: (1) the internal structure of the continents, especially East Antarctica, and (2) the link to its adjacent parts in a Gondwana framework. Figure 5.1, Figure 5.4 and Figure 5.5 show the results in a pre-Gondwana break-up configuration ca 200 Ma ago based on a deforming plate model<sup>5</sup>.

The area, where the integration of satellite and aeromagnetic data has changed the most is Southern Africa. Figure 5.4 shows a zoom to the link between South Africa and East Antarctica. It has been already discussed that the Beattie anomaly can be linked to an anomaly with similar amplitude and trend in Dronning Maud Land, Antarctica ([Riedel et al. 2012](#)) that sharply terminates along the western orogenic front of the East African Orogen ([Corner and Groenewald 1991](#); [Jokat et al. 2003](#); [Golynsky and Jacobs 2001](#)). Recently, it was suggested by geological-petrological modelling that the Beattie anomaly is linked to a shear zone near the southern boundary of the Natal terrane ([Scheiber-Enslin et](#)

al. 2014). The anomaly is part of a family of anomalies, one of which correlates with outcropping shear zones in the Mesoproterozoic Natal belt for which a complex remanent magnetisation was suggested (Maré and Thomas 1997). However, the corresponding Antarctic anomalies have a higher amplitude (Figure 5.4), due to the fact that the corresponding sources on the South African side are covered by sediments of the Karoo basin. In the satellite data, a weak imprint of the Beattie anomaly is visible, which confirms its regional significance (Figure 5.4).

The satellite data show their potential in illuminating the link between India and East Antarctica (Figure 5.5). In the original satellite data, the Indian-Antarctic link is not very pronounced, but after the RTP correction, the anomalies line up, indicating a continuation of the Indian geological provinces under the Antarctic ice. Satellite data are limited in their ability to resolve local structures, but are expected to reflect the major tectonic setting. The match-up of the India and Antarctic pieces suggest that the sources are upper crustal Precambrian basement that has not been significantly altered by continental break-up.

However, future more detailed analysis should consider the importance of remanent magnetisation, as many of these rock formations are billions of years old and gained parts of their magnetic orientation during emplacement or formation when the Earth's magnetic field had a different orientation. Ideally, to increase the correlation of the Indian continent to Antarctica, one would need to process the aeromagnetic data for India in the same manner as for the other continents, if the survey data became available.

#### 5.4. Conclusions

Aeromagnetic data are important when discussing the tectonic setting of the continents, especially in a plate reconstruction. However, aeromagnetic compilations should be conformed to satellite data to be spectrally consistent, especially when these compilations are based on multiple surveys acquired over a long time period. The increased resolution and accuracy of satellite data allows confident identification of the main tectonic signatures in the data sets. In this study, the higher resolution of the conformed compilations further aids the interpretation of the links between East Antarctica and its former Gondwana neighbours. That is clearly seen both in the well-established link between Australia and Antarctica and the less-explored link between the interior of Southern Africa and Antarctica. RTP satellite data show furthermore the huge potential for reinterpreting the link between India and East Antarctica, when aeromagnetic data over the Indian subcontinent become available.

Less important here is the exact geometry of the margins and break-up, but that properties from the interior of the continents can be linked to their previous neighbours. Here, we emphasis this for East Antarctica. A natural next step would be to apply multivariate analysis (Stål et al. 2019) adding the magnetic data. That would allow definition of lithospheric domains for East Antarctica in line with the

tectonic setting of Australia, Southern Africa and possibly India. This furthermore could help to interpolate other sparse measurements into East Antarctica or to define statistical correlations which can be used for predictions. A current application is deriving geothermal parameters under the Antarctic ice ([Burton-Johnson et al. 2020](#)). Guided interpolation of geothermal heat-flow values using the magnetic field is possible, as well as cluster analysis and machine learning approaches, where statistically correlation are exploited for improved predictions.

## 5.5. Data and Methods

Australia, Southern Africa and Antarctica are three of the areas of the world with particularly comprehensive aeromagnetic data coverage (see Figure 5.2, Figure 5.6 and Figure 5.7). In Australia and Southern Africa, widespread high-resolution aeromagnetic data acquisition has primarily been motivated by mineral resource mapping ([Milligan et al. 2004](#); [Stettler et al. 2000](#)), while in Antarctica the focus has mostly been on systematically exploring subglacial geology and defining large-scale crustal architecture ([Mieth and Jokat 2014](#); [Golynsky et al. 2018](#); [Ferraccioli et al. 2009](#)). Therefore, the survey parameters (e.g. survey height and line spacing) typically adopted in the three continents are quite different.

Over Australia more than 800 individual surveys are nowadays included in Geoscience Australia's National Airborne Geophysical Database (NAGD) that contains more than 31 million line kilometres of total field magnetic intensity data. Since 1990, surveys have usually been conducted with flight line spacing of 400 metres or less ([Milligan et al. 2004](#)). To reduce long-wavelengths errors, high-altitude airborne traverse data were used, which significantly improved the intermediate wavelengths from 100 to 500 km. For edition 5 of the magnetic anomaly map for Australia, which is used here, the long-wavelength part (>1000km) has been replaced with the satellite magnetic model MF-6.

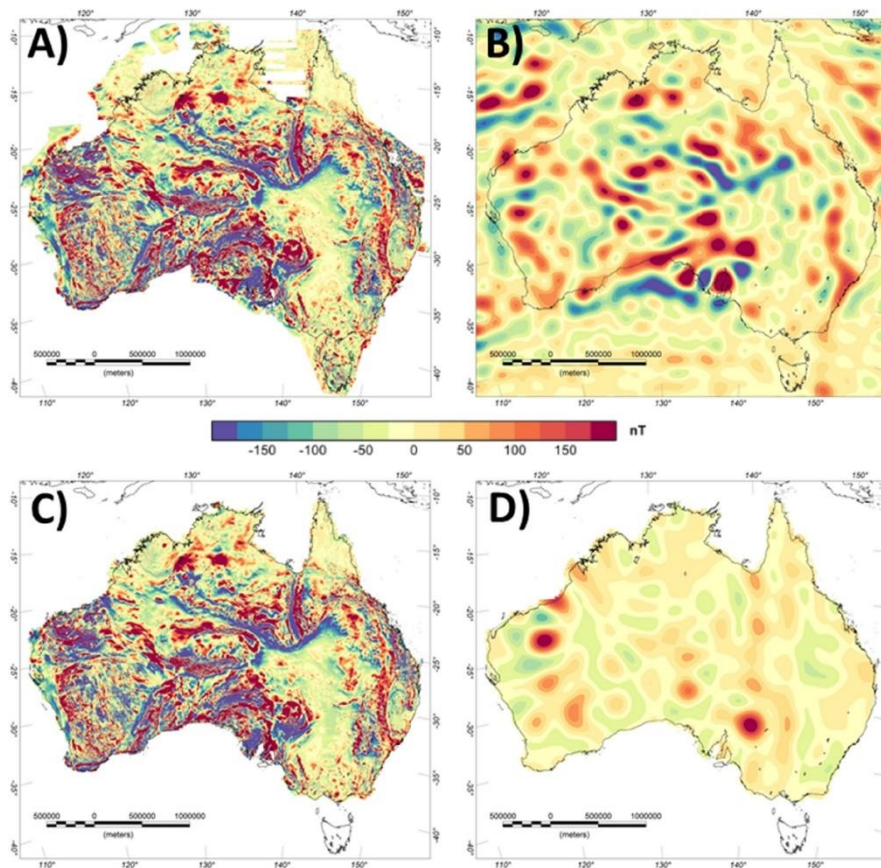


Figure 5.6: Lithospheric magnetic anomaly of Australia. (A) Original aeromagnetic compilation ([Franklin and Milligan 2010](#)), (B) Satellite-derived model LCS-1, (C) Conformed aeromagnetic and satellite model, (D) Difference between (A,C).

Systematic data acquisition in Antarctica started as early as the International Geophysical Year 1957–1958. A wealth of modern airborne geophysical surveys, including airborne gravimetry and aeromagnetic data acquisition over previously largely unexplored Antarctic frontiers, such as the Gamburtsev Subglacial Mountains ([Ferraccioli et al. 2011](#)) and Wilkes Land in East Antarctica ([Aitken et al. 2014](#)) was stimulated by the International Polar Year 2007/2008. The first Antarctic magnetic anomaly compilation (ADMAP-1) was produced in 2001 from more than 1.5 million line kilometres of shipborne and airborne measurements ([Golynsky et al. 2006](#)). This was succeeded in 2018 by the second-generation Antarctic magnetic anomaly compilation (ADMAP-2) that includes more than 3.5 million line-km of aeromagnetic and marine magnetic data that more than doubles the initial near-surface database ([Golynsky et al. 2018](#)). Large-scale international aeromagnetic exploration in Antarctica has continued since ADMAP-2, with major more recent surveys flown e.g. over the Recovery and South Pole frontiers ([Forsberg et al. 2018](#); [Paxman et al. 2019](#)).

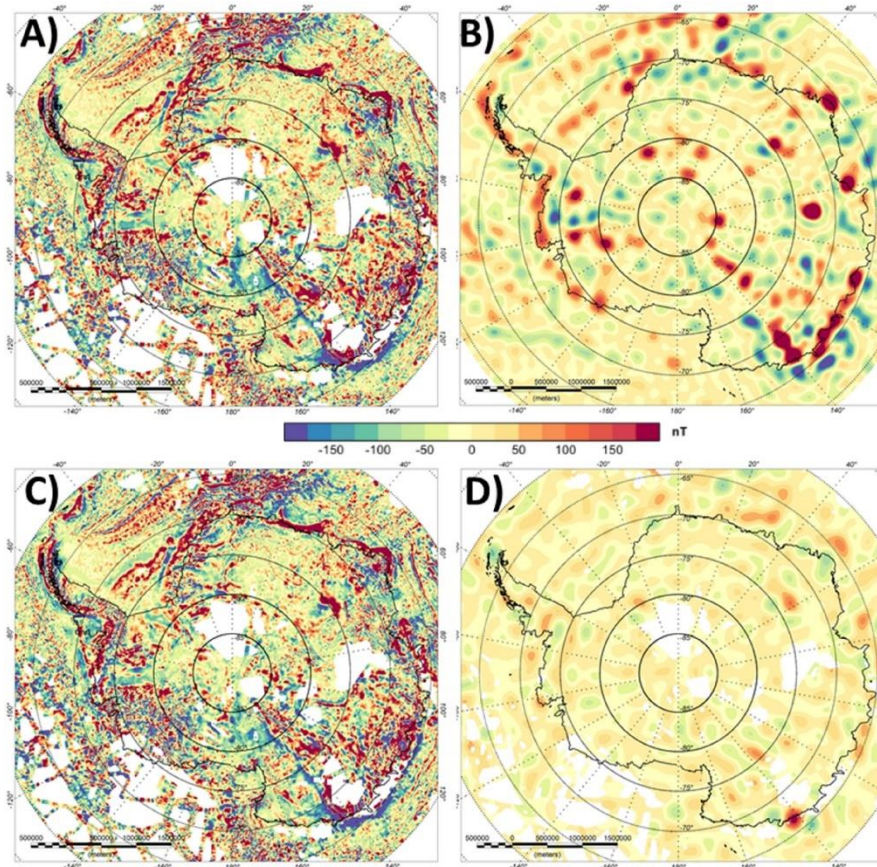


Figure 5.7: Lithospheric magnetic anomaly of Antarctica. (A) Original aeromagnetic compilation ([Golynsky et al. 2018](#)), (B) Satellite-derived model LCS-1, (C) Conformed aeromagnetic and satellite model, (D) Difference between (A, C).

For Southern Africa (Figure 5.2), two modern compilations exist from the Council for Geoscience, Republic of South Africa, who began collecting and compiling aeromagnetic data in the 1970s. Similar programs of collecting aeromagnetic data throughout the Southern Africa region have resulted in nearly complete aeromagnetic coverage of South Africa, Namibia, Botswana and Zimbabwe. The Council for Geoscience has compiled all of these magnetic data available in southern Africa and has gridded the data at one km grid spacing ([Stettler et al. 2000](#)). Because the data have a relatively large line spacing (1 km), they were initially only used for large scale mapping, mainly for mapping the Kaapvaal Craton boundary, lithology identification and for defining important linear magnetic features ([Webb 2009](#)). An update for the Republic of South Africa is now available ([Council for Geoscience 2019](#)). The long-wavelength part between the two compilations is quite different, while the short-wavelength part is very similar, again confirming the use of a common reference model. Quantitative interpretations of the higher resolution data concentrated on individual targets such as the Beattie magnetic anomaly ([Scheiber-Enslin et al. 2014](#); [Lindeque et al. 2011](#); [Weckmann et al. 2007](#)).

The satellite model for the lithospheric magnetic field is LCS-1 ([Olsen et al. 2017](#)). LCS-1 contains the spherical harmonics from degree and order 15-185. The lower order spherical harmonics are

associated with the main (core) field and omitted from the lithospheric field part. In comparison to previous models, LCS-1 represents the field to a high spherical harmonic degree by providing coefficients to 185 corresponding to ~220 km wavelength. Based on the data from pre-Swarm satellite mission data only, earlier models limited the representation to degree 70 (~600 km), 85 (550 km) or 130 (300 km). For LCS-1, the spectral range to degree 130 is globally consistently estimated, while for the higher spherical harmonics, especially in Polar Regions, the noise increases, making the representation less accurate. Still, for Australia there is lithospheric signal contained in the higher spherical harmonics ([Olsen et al. 2017](#)).

## 5.6. Conforming aeromagnetic compilation to satellite model

To homogenize the data, we applied an equivalent dipole layer approach coupled with spherical harmonic representation (Chapter 3). The reason for using an equivalent source method is, that the Fourier based methods result in artefacts when applied to global long-wavelength satellite data and suffer from instabilities at the magnetic equator. Equivalent sources do not suffer from this instability, but require extensive computational resources. Hence for the aeromagnetic surveys a simplification has to be made.

- 1) For estimating the magnetic parameters of the equivalent dipole layer, we used BiCGSTAB iterative inversion method. For the satellite data, we located the equivalent dipole layer at 30 km beneath the reference level with a horizontal spacing of 25 km corresponding to the data spacing. These values were found to best represent both the spectral content at an observation height of 400 km and near surface. The field was inverted using the direction of the main field model CHAOS-6 ([Finlay et al. 2016](#)) at each dipole location. No amplitude correction was applied. CHAOS-6 was also used as reference model for LCS-1.
- 2) From the equivalent dipole layer, we forward calculate the RTP model at 5 km ellipsoidal height for a vertical field and a constant field strength.
- 3) For the aeromagnetic data, we also applied an equivalent dipole layer representation, but for computational reasons, first performed a simple resampling of the data data to ~22 km (0.2 degree equiangular) resolution for Australia and Southern Africa and ~44 km (equidistant) for Antarctica. This step did not affect the long-wavelength content of the data, but obviously limited the short-wavelength content. The equivalent sources were again located at 30 km beneath the reference level and were calculated using CHAOS-6 as main field.
- 4) Next, we estimated the spherical harmonic coefficients from the equivalent layer for both the satellite and aeromagnetic data by calculating the coefficient for each dipole and summing up their

individual effects. Spherical harmonic coefficients have been calculated to degree and order 180 for satellite data and 720 for the aeromagnetic data sets.

- 5) For spherical harmonic coefficients up to degree and order 130, the difference between the satellite and aeromagnetic data has been calculated and used to correct the original aeromagnetic data.

## 5.7. Data Availability

The aeromagnetic data are available at:

South Africa:

<http://www.geoscience.org.za/index.php/2019-03-13-12-40-41/publications/284-geophysical-data>

Australia:

<http://www.ga.gov.au/news-events/news/latest-news/latest-editions-of-magnetic-anomaly-grid-and-radiometric-map-released>

Antarctica: <https://doi.pangaea.de/10.1594/PANGAEA.892724>

The satellite model LCS-1 can be accessed at:

<http://www.spacecenter.dk/files/magnetic-models/LCS-1/>

The reprocessed grids with 0.1-degree resolution can be accessed here:

<https://www.3dearth.uni-kiel.de/en/public-data-products>

Full resolution data sets can be provided on request by the authors.

## 5.8. Plate-tectonic illustrations

Figure 5.1, Figure 5.4, Figure 5.5 and the movie in the supplementary material have been made with GPlates (<http://www.gplates.org/>) using its global reconstruction files. The supplementary animation provides an example for the last 200 My of plate tectonics centred over Antarctica. The movie illustrates with the conformed aeromagnetic data and satellite data as infill, where no aeromagnetic data are available, the link between Antarctica and the adjacent continents. The plate-tectonics illustration was done in GPlates (<http://www.gplates.org/>).

## 5.9. Acknowledgements

This work was supported by the European Space Agency (ESA) as part of the Support to Science Element 3D Earth and by the Deutsche Forschungsgemeinschaft (DFG; German Research Foundation) under the SPP1788 (DynamicEarth) project Magnetic Lithosphere (EB255/2-2).

## 5.10. Author Contributions

J.E. drafted the manuscript and reprocessed the data sets. Y.D. programmed and applied the equivalent source algorithm. P.H. calculated the plate-reconstructions. F.F. wrote the interpretation of reconstructed map and the setting of Antarctica. S.S.-E. helped with interpretation of the link between Southern Africa and Antarctica. All authors read and commented on the draft manuscript.

# Global high-resolution magnetic field inversion using spherical harmonic representation of tesseroids as individual sources

Eldar Baykiev, Yixiati Dilixiati, Jörg Ebbing

Institute of Geosciences Kiel University, Kiel, Germany

Published in: *Geosciences*, 10(4), 147; <https://doi.org/10.3390/geosciences10040147>

## 6.1. Introduction

The Earth's magnetic field contains signal from various sources, including the core, ionosphere, magnetosphere and the Earth's magnetic lithosphere (e.g. [Langel and Hinze 1998](#)). The lithospheric magnetic field reflects the tectonic setting and geological provinces of the Earth as shown by the typical stripe anomalies over the oceans reflecting seafloor spreading ([Müller et al. 2008](#)). Often the lithospheric magnetic anomalies are interpreted from aeromagnetic surveys, where the contribution of the inducing core field is routinely reduced during processing: aeromagnetic surveys commonly have limitations with respect to long wavelengths due to the survey extension or the methods by which individual surveys are stitched together.

Global models of the lithospheric magnetic field, on the other hand, can provide a global heterogeneous coverage and are usually based on a spherical harmonic representation (e.g. [Maus 2010](#)). For these models, the reliable spectral range is defined by the part not dominated by the main field and within the measuring bandwidth of the data sources. The main field associated with the core, is dominating the spherical harmonic coefficients up to degree 15. Therefore, lithospheric models like LCS-1 ([Olsen et al. 2017](#)) only define a reliable lithospheric field spectral content for degrees > 15.

LCS-1 provides the coefficients to degree and order 185 based on measurements from the CHAMP and Swarm satellite missions. [Kotsiaros and Olsen \(2014\)](#) showed that combination of the gradient observations with the vector information improves the lithospheric field determination and reliable range can be increased to degree  $n = 154$  in comparison to only vector measurements, which can reach degree  $n = 138$  only. However, for previous models like the various generations of MF (e.g. [Maus 2010](#)), it is stated that satellite-data provide the full signal to degree and order 85, while some signal loss is occurring for the higher degrees. LCS-1 using data from the multi-satellite mission Swarm shifts this range to degree 133 and provides even higher coefficients. This improvement is significant as the reliable spectral range of the satellite lithospheric field is currently one of the basic limitations

concerning the robustness of the interpretation of lithospheric field model in terms of magnetization and magnetic crustal thickness on continental or global scales.

A number of studies previously presented models of the lithospheric magnetization within the spherical harmonic degree range corresponding to the satellite-derived lithospheric field. First magnetic crustal models were presented by ([Meyer et al. 1983](#); [Hahn et al. 1984](#)), based on seismic crustal thickness estimated and susceptibility estimations from geology. These models took in account only an induced magnetization and were not coinciding with Magsat anomaly maps ([Langel et al. 1982](#)). The Standard Earth Magnetization Model ([Purucker et al. 1998](#)) included both induced and remanent magnetizations, using the 3SMAC model ([Nataf and Ricard 1996](#)) to set different tectonic areas (i.e. magnetic properties) and a remanent magnetization in oceans from ([Dyment and Arkani-Hamed 1998](#)). This model was updated several times by adding further crustal models and information about heat-flow ([Purucker et al. 2002](#)). Hemant ([2003](#)), Hemant and Maus ([2005](#)) introduced a model where ranges of susceptibilities and magnetizations were assigned for each geological region of the world according to geographical information system (GIS). The model was adjusted via iterative inversion to fit satellite-derived (mostly from CHAMP satellite mission) lithospheric field model MF7 ([Maus 2010](#)). The result was the vertically integrated susceptibility (VIS) model and vertically integrated remanent magnetization (VIM) for the oceanic crust. Later, the remanent model was modified by making plate reconstruction corrections and improving oceanic remanence estimates ([Masterton et al. 2013](#)). However, the VIS model is still considered the reference for any later attempts.

Another limitation in inferring information for the magnetic sources comes from the non-uniqueness of the magnetization solution due to the existence of magnetization structures that do not produce any visible magnetic field, the so-called annihilators ([Lesur and Jackson 2000](#); [Lesur and Vervelidou 2020](#); [Maus and Haak 2003](#)). That means that any inversion requires a priori information or a reference model to result in plausible susceptibilities.

All these inversion and modelling approaches used fitting and/or inversion based on point dipole sources. That allows only a simplified representation of the geometry of the crusts, especially when seismic and other types of information are considered. However, modelling of aeromagnetic surveys requires such a better representation of the source bodies and therefore often Cartesian or Fourier based approaches are used ([Götze and Lahmeyer 1988](#)). A representation with magnetic tesseroids ([Baykiev et al. 2016](#)) provides a versatile discretization that can be used for modelling both satellite and airborne data. The forward modelling code of ([Baykiev et al. 2016](#)) allows the calculation of the magnetic field in spherical coordinates using spherical prisms, which are also called tesseroids (magnetic sources).

However, magnetic inversion of satellite-measured data within a particular wavelength window, corresponding to the reliable lithospheric field, is only viable if the signal of the individual sources is also filtered to the same spectral range. Therefore, the calculated field (across the entire spherical surface) of each tesseroïd can be converted into a spherical harmonic representation. This enables the inversion for the reliable wavelength range while keeping the geometrically confined and discretized lithospheric magnetization model. This set-up allows a reliable calculation of the magnetic field at any altitude above the Earth's surface.

In the following, we first outline inversion method that is designed to have an adequate source discretization and inverts for a specific spherical harmonic range only. The validity of the approach is demonstrated with a synthetic example and next applied to the satellite-model LCS-1 in order to provide a global lithospheric susceptibility model, which as we demonstrate at the end can serve as reference or background model for further studies on local scales.

## 6.2. Methodology

### 6.2.1. Tesseroid Forward Field

The software package magnetic tesseroids ([Baykiev et al. 2016](#)) is used for the forward calculation. Magnetic tesseroids calculates the vector magnetic field of a given tesseroid model on a specified grid. The magnetic contributions of all tesseroids in the model are summed up in the resulting data grid of the magnetic field vector components. In case of only induced magnetization, the vector magnetic field of each tesseroid is directly proportional to its magnetic susceptibility  $\chi$  ([Baykiev et al. 2016](#)):

$$\mathbf{B}_P = \chi \frac{\Phi_P \cdot \mathbf{R}_{coord}(\lambda_C, \varphi_C, \lambda_P, \varphi_P) \cdot \mathbf{B}_C}{4\pi G \rho} \quad (6.1)$$

where

$$\mathbf{R}_{coord}(\lambda_C, \varphi_C, \lambda_P, \varphi_P) = \mathbf{E}_{NEU} \cdot \left( \mathbf{R}_y \left[ \frac{\pi}{2} - \varphi_P \right] \right)^T \cdot \left( \mathbf{R}_z[\lambda_P] \right)^T \cdot \mathbf{R}_z[\lambda_C] \cdot \mathbf{R}_y \left[ \frac{\pi}{2} - \varphi_C \right] \cdot \mathbf{E}_{NEU} \quad (6.2)$$

$\mathbf{R}_y$ ,  $\mathbf{R}_z$  and  $\mathbf{E}_{NEU}$  are the rotation matrices:

$$\mathbf{R}_y[\alpha] = \begin{bmatrix} \cos \alpha & 0 & \sin \alpha \\ 0 & 1 & 0 \\ -\sin \alpha & 0 & \cos \alpha \end{bmatrix}, \mathbf{R}_z[\alpha] = \begin{bmatrix} \cos \alpha & -\sin \alpha & 0 \\ \sin \alpha & \cos \alpha & 0 \\ 0 & 0 & 1 \end{bmatrix}, \mathbf{E}_{NEU} = \begin{bmatrix} -1 & 0 & 0 \\ 0 & 1 & 0 \\ 0 & 0 & 1 \end{bmatrix} \quad (6.3)$$

$\Phi_P$  is the tesseroid's gravity tensor in the coordinate system of the computation point P and  $\mathbf{B}_C$  is the magnetizing field in the coordinate system of the tesseroid's center C.

Therefore, the magnetic field vector in each point of the two-dimensional spherical grid can be expressed as:

$$\mathbf{B}_{P(i,j)} = \chi \frac{\Phi_{P(i,j)} \cdot \mathbf{R}_{coord}(\lambda_C, \varphi_C, \lambda_{P(i,j)}, \varphi_{P(i,j)}) \cdot \mathbf{B}_C}{4\pi G \rho} \quad (6.4)$$

where  $i = 1 \dots I$ ,  $j = 1 \dots J$  are the indices of the computational point within this spherical grid with  $I$  longitudes and  $J$  latitudes.

### 6.2.2. Spherical Harmonic Model

In this study, we utilize the software package SHTools ([Wieczorek and Meschede 2018](#)) to convert the forward calculated spherical grids ( $\mathbf{B}_{P(i,j)}$ ) into a spherical harmonic representation. For the inversion we set calculated grids ( $\mathbf{B}_{P(i,j)}$ ) to be equidistant with the number of points  $= 2 \times J$ . To convert the grid into a spherical harmonic model, SHTools utilizes the algorithm of ([Driscoll and Healy 1994](#)) of efficient computation of the spherical harmonic expansion of functions defined on a two-dimensional sphere. The relative errors using the method on  $I = 2 \times J$  sampled grids are similar to using grids with datapoints at Gauss-Legendre quadrature spacing (see [Driscoll and Healy 1994](#) for more details).

### 6.2.3. Projected Gradient Inversion

Generally, geophysical inversion is ill-posed. Due to the presence of noise in the observed data and rounding errors in forward calculation, the existence, uniqueness and stability of the inversion are hard to guarantee. For unique solution, constraints or specific inversion method must be applied. However, in classical methods like least-squares inversion or Tikhonov regularization, the resulting susceptibilities are not constrained even though if the geometry is known. Hence, the inversion can result in negative susceptibilities, which are unreasonable if occurring for large areas over the continents. Furthermore, the addition of further constraints requires certain modifications.

Therefore, we adopt the projected gradient method ([Lin 2007](#)), which allows us to exclude negative susceptibility values and to set a priori constraints.

The projected gradient method is a way to solve a constrained optimization problem, more specific a non-negative least square linear inversion problem. The optimization problem is,

$$\min_{\chi \geq 0} \|\mathbf{A}_{SHC} \mathbf{x} - \mathbf{d}_{SHC}\|_2^2 \quad (6.5)$$

where  $\mathbf{A}_{SHC}$  is the sensitivity matrix which represents each the magnetic field spherical harmonic coefficients of each tesseroid,  $\mathbf{x}$  is the magnetic susceptibility and  $\mathbf{d}_{SHC}$  represents the spherical harmonic coefficients of the observed magnetic field model.

The cost function  $f(\mathbf{x})$  is:

$$\begin{aligned} f(\mathbf{x}) &= \min_{\chi \geq 0} \|\mathbf{A}_{SHC} \mathbf{x} - \mathbf{d}_{SHC}\|_2^2 = \min_{\chi \geq 0} \{(\mathbf{A}_{SHC} \mathbf{x} - \mathbf{d}_{SHC})^T (\mathbf{A}_{SHC} \mathbf{x} - \mathbf{d}_{SHC})\} \\ &= \min_{\chi \geq 0} \mathbf{x}^T \mathbf{A}_{SHC}^T \mathbf{A}_{SHC} \mathbf{x} - 2\mathbf{d}_{SHC}^T \mathbf{A}_{SHC} \mathbf{x} + \|\mathbf{d}_{SHC}\|_2^2 \\ &= \min_{\chi \geq 0} \mathbf{x}^T \mathbf{Q} \mathbf{x} - \mathbf{P}^T \mathbf{x} + \|\mathbf{d}_{SHC}\|_2^2 \end{aligned} \quad (6.6)$$

where  $\mathbf{Q} = \mathbf{A}_{SHC}^T \mathbf{A}_{SHC}$ ,  $\mathbf{P} = 2\mathbf{A}_{SHC}^T \mathbf{d}_{SHC}$ , and the constrained optimization problem becomes a constrained quadratic programming (QP) problem.

Gradient Descent type method is a standard way to solve the quadratic optimization problem. To ensure non-negative solution to the optimization problem, the projection operator is used to force the iteration back to the constraint range. Specifically, the projected gradient method iteratively uses the gradient projection to update the current solution  $\mathbf{x}^k$  to  $\mathbf{x}^{k+1}$  by the following rule,

$$\mathbf{x}^{k+1} = P_{\Omega}\{\mathbf{x}^k - \alpha_k \cdot Grad(\mathbf{x}^k)\} \quad (6.7)$$

where

$$P_{\Omega}\{\mathbf{x}\} = \begin{cases} \mathbf{x} & \text{if } \mathbf{x} > 0 \\ 0 & \text{if } \mathbf{x} \leq 0 \end{cases} \quad (6.8)$$

$\alpha_k$  is the step size and  $Grad(\mathbf{x}^k)$  is the search direction which is defined by the equation below.

$$Grad(\mathbf{x}^k) = \mathbf{A}_{SHC}^T \mathbf{A}_{SHC} \mathbf{x}^k - \mathbf{A}_{SHC}^T \mathbf{d}_{SHC} \quad (6.9)$$

To find a reasonable step size  $\alpha_k$  in each iteration, there are sub-iterations to either increase or decrease the initial guess  $\alpha_0 = 1$  by  $0.1^t$  until  $\alpha_k$  satisfies the so-called sufficient decrease condition

$$f(\mathbf{x}^{k+1}) - f(\mathbf{x}^k) \leq 0.01(\mathbf{x}^{k+1} - \mathbf{x}^k)^T Grad(\mathbf{x}^k) \quad (6.10)$$

However, the computational complexity per iteration is relatively large to find a step size  $\alpha_k$  satisfying the condition. To reduce the cost of checking this condition, Lin (2007) uses a Taylor expansion of the cost function and simplifies the sufficient decrease condition as shown in the equation below.

$$(1 - 0.01)(\mathbf{x}^{k+1} - \mathbf{x}^k)^T Grad(\mathbf{x}^k) + 0.5(\mathbf{x}^{k+1} - \mathbf{x}^k)^T \mathbf{Q} (\mathbf{x}^{k+1} - \mathbf{x}^k) < 0 \quad (6.11)$$

We use the Projected Gradient Method with the simplified form of the sufficient decrease condition for our analysis, in the way it is presented here.

### 6.3. Data

For both the synthetic and real data application, we use a similar set of data to confine the geometry and parameters space. For the synthetic inversion, a global lithospheric field model is forward calculated from a crustal model with predefined susceptibility. The same geometry is later used for the inversion of a measured lithospheric magnetic field model.

#### 6.3.1. Model Geometry

For all calculations, we assume the entire crust to be magnetic and set the geometry of the model, which defines the size of the tesseroids. The top of the model is the top of the crystalline basement as provided from the model Crust1.0 (Laske et al. 2013), originally with  $1^\circ \times 1^\circ$  resolution (Figure 6.1a), but here for the global application resampled to  $2^\circ \times 2^\circ$  resolution. The base of the model is the Moho boundary. The Moho depth model is taken from (Szwilius et al. 2019) (Figure 6.1b). The model is based

on a similar catalogue as the Moho depth in Crust1.0, but based on a geostatistical kriging approach and provides uncertainties, which potentially can be exploited in further modifications. This set-up defines a one-layered crust, which is presented with tesseroids, which have variable thickness.

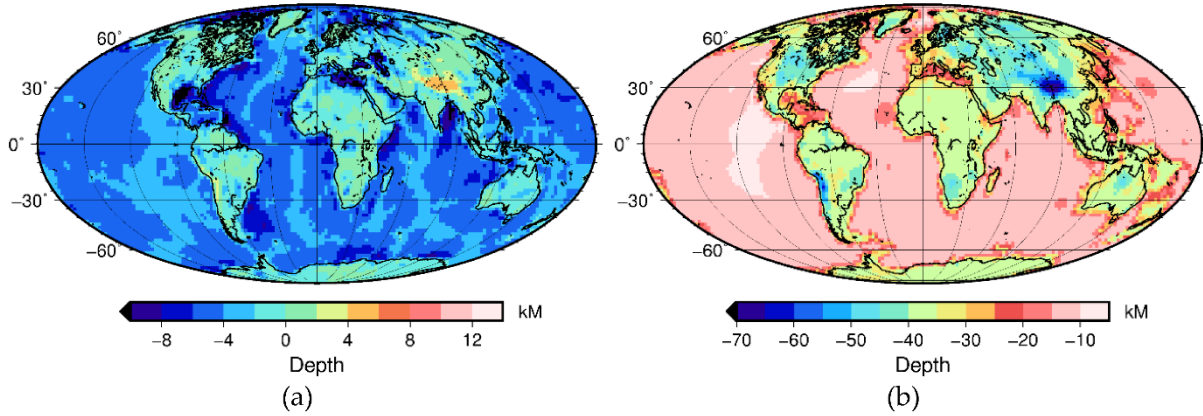


Figure 6.1: Upper and lower boundaries of the synthetic model: (a) basement depth taken from CRUST1.0 (Laske et al. 2013) and (b) Moho depth taken from Reference (Szwilius et al. 2019).

### 6.3.2. Magnetization Direction and Susceptibility

Induced magnetization in the crust is a response of the mainly ferrimagnetic rock properties to the inducing main field. We use International Geomagnetic Reference Field model, year 2014 (Thébaud et al. 2015) to define the direction and strength of the inducing field in the centrepoint of each tesseroid.

For the initial susceptibility distribution in the model, we use the VIS model from Hemant & Maus (2005). For each tesseroid the susceptibility is calculated from their model by dividing the VIS model by the height of the tesseroid. The VIS value used is the mid-tesseroid value (Figure 6.2a).

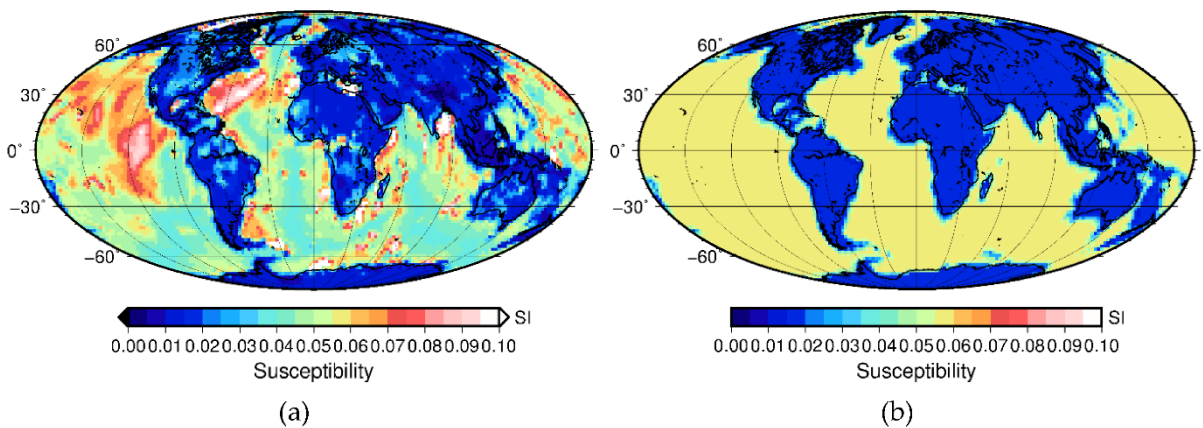


Figure 6.2: Susceptibility distribution in synthetic models: (a) susceptibility based on a vertically integrated susceptibility model (Hemant and Maus 2005). (b) Initial guess  $\mathbf{x}_A^0$  with averaged susceptibilities from Hemant VIS-based initial guess  $\mathbf{x}_H^0$ . Crustal domain boundaries are taken from the age of the oceanic crust map (Müller et al. 2008).

To explore the effect of a-priori information (initial guess) on the inversion, we calculate a simplified susceptibility distribution with averaged values for oceanic and continental crust (Figure 6.2b). We use the map of the age of the oceanic crust by (Müller et al. 2008) and separate the oceanic and continental crust and calculate the mean average susceptibility from the VIS model in Figure 6.2a. This results in average value for the continental crust of 0.0154 SI and for the oceanic crust of 0.0555 SI.

While we neglect remanence in the synthetic tests, we also consider remanent magnetization as a priori information in the application to real data. For this, we use the remanent magnetization vectors from (Masterton et al. 2013) and calculate the corresponding field using 1-km thin tesseroids to imitate original dipole methods of Masterton et al. (2013). The model of Masterton et al. (2013) relies on many initial assumptions, such as shape of the sources in the oceanic crust, which may not coincide with the actual sources in the real crust. However, it is currently the best available model to subtract the remanent field of the oceans.

### 6.3.3. Lithospheric Magnetic Field Models

#### 6.3.3.1. LCS-1

For the global inversion of real data, we choose the lithospheric magnetic field model LCS-1, which is the most up-to-date spherical harmonic model of the lithospheric field derived from the CHAMP and Swarm satellite observations (Olsen et al. 2017). Figure 6.3a shows the field for spherical harmonic degrees 16-89 at 400km height, representing satellite orbit height. The lower cut-off is in line with the original model, while the higher cut-off is chosen in line with our model parametrization.

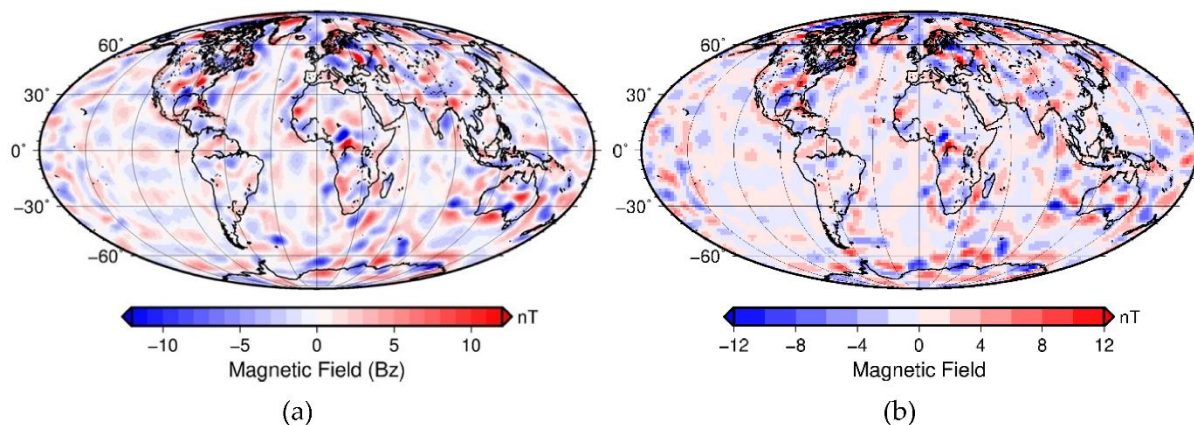


Figure 6.3: LCS-1 with and without remanence: (a) LCS-1 with degrees from  $n = 16$  to 89, (b) LCS-1 without modelled remanent field (Figure 6.4b), within degrees from  $n = 16$  to 89.

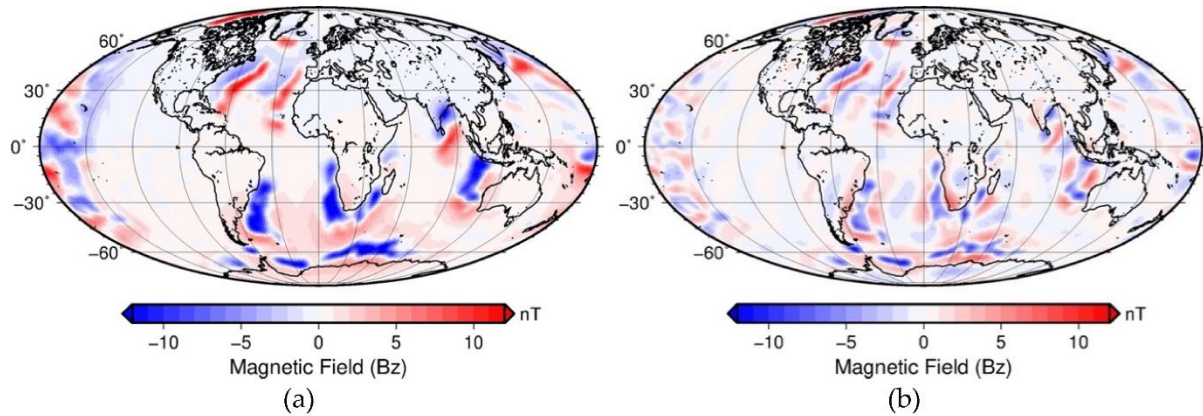


Figure 6.4: Spherical harmonic model of the remanent field derived from Masterton et al. (2013): (a) all spherical harmonic degrees from  $n = 1$  to 89, (b) truncated model with degrees from  $n = 16$  to 89.

We use the remanent magnetization model of Masterton et al. (2013) and calculate the corresponding magnetic field for the spherical harmonic degrees 16-89. For this, we assign the remanent vector model to a spherical shell of 1 m thickness made of tesseroids  $0.25^\circ$  in longitudinal and latitudinal width. From this, we calculate the remanent field (Bz component) at the altitude of 400 km (Figure 6.4). Truncated spherical harmonic model of the calculated remanent field is shown in Figure 6.4b and the residual after subtracting this field from LCS-1 in Figure 6.3b.

### 6.3.3.2. Synthetic Observed Field

For the analysis, we create a synthetic input data set for testing our inverse approach. For this, we forward calculate the with magnetic tesseroids (Baykiev et al. 2016) the magnetic field of a crustal model at the satellite altitude of (400 km). The grid spacing is chosen to be 1 degree, which approximately corresponds to a spherical harmonic degree of  $n = 89$ . Calculated grid is converted into a spherical harmonic model with maximal degree  $N = 89$  using SHTools (Wieczorek and Meschede 2018) (see Figure 6.5a). To further imitate a satellite-derived lithospheric magnetic field model, we truncate all degree below and including degree  $n = 15$ . Filtered synthetic observed Bz component is shown in Figure 6.5b.

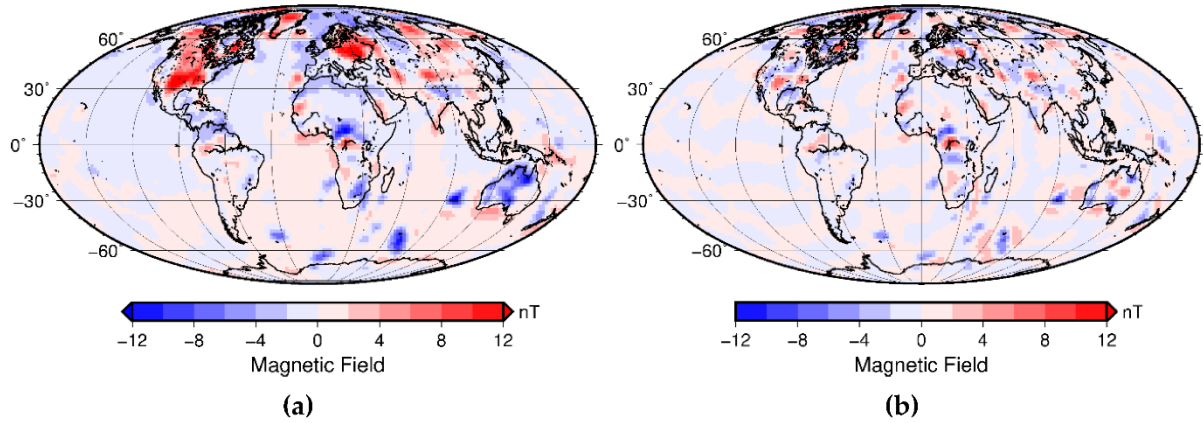


Figure 6.5: Spherical harmonic model of the synthetic field: (a) all spherical harmonic degrees from  $n = 1$  to 89, (b) truncated model with degrees from  $n = 16$  to 89.

## 6.4. Results

### 6.4.1. Synthetic Test

The first test explores how the inversion of a truncated field recovers the initial true model used to create the synthetic field. The loss of the long wavelength part between degree 1 and 15 implies that the inversion might tend to result in solutions that may not match susceptibility distribution in the true model.

The Projected gradient method requires an initial solution that is used as a first guess before iterations start. To explore how the truncation of the field affects the inversion results, we introduce two a priori models:  $\mathbf{x}_H^0$  with the susceptibility distribution from the true model (see Figure 6.2a), and  $\mathbf{x}_A^0$  with averaged susceptibility values for oceanic and continental crustal areas (Figure 6.2b).

#### 6.4.1.1. A-Priori Model from a True Susceptibility Model

This first test helps to identify the error introduced by grid processing and creation of spherical harmonic models of each tesseroid field within the algorithm. For the inversion using a truncated field with a true model  $\mathbf{x}_H^0$  as an initial assumption, we expect that manipulations with grids introduce rounding error and that not a complete fit can be achieved. After the first iteration, the projected gradient norm reaches its minimum (approx.  $75,696 \times 10^{-4}$ ) and remains the same for all further iterations.

One can use the iteration value of  $75,696 \times 10^{-4}$  for the linear norm to set up a threshold for future inversions, since this value represents the error introduced by re-gridding and the conversion to spherical harmonics.

RMS of the difference between the true model  $\mathbf{x}_H^0$  and the inversion result  $\mathbf{x}_H^{N=1}$  after the first iteration is about 0.0 SI, i.e. non-zero linear norm value after the initial iteration does not affect result and the

way floating point numbers from the result are stored in the output text files (max 18 digits after the point).

#### 6.4.1.2. Initial Guess with Averaged Susceptibility for Oceanic and Continental Crust

Next, we explore the effect of the a priori model. Earth lithosphere magnetization is not well known, hence the effect of the a priori assumptions might seriously affect the results. For this, we compare the results of the inversion (Figure 6.6b) with the initial guess  $\mathbf{x}_A^0$  (Figure 6.2b) with the true model  $\mathbf{x}_H^0$  (Figure 6.2a). Figure 6.7 and Figure 6.8 indicate that the fit for the field is very good for degrees  $n > 15$  and the RMS of the difference between the observed and calculated field is very low (0.00933 nT) (Figure 6.6b).

However, the long-wavelength part of the spectra is very different. The resulting susceptibility distribution  $\mathbf{x}_A^N$  is similar in patterns as the true model  $\mathbf{x}_H^0$  (Figure 6.2a), but has an overall decreased amplitude, especially for spatially large areas (Figure 6.7a). This can be explained by the differences in the long-wavelength range. The inversion provides only susceptibilities in the limited spectral range. To explain degrees 16-85, the amplitude of long-wavelength anomalies (and therefore susceptibility of spatially wide sources) can be lower than in the true model. That is also seen in the spectral representation in Figure 6.8.

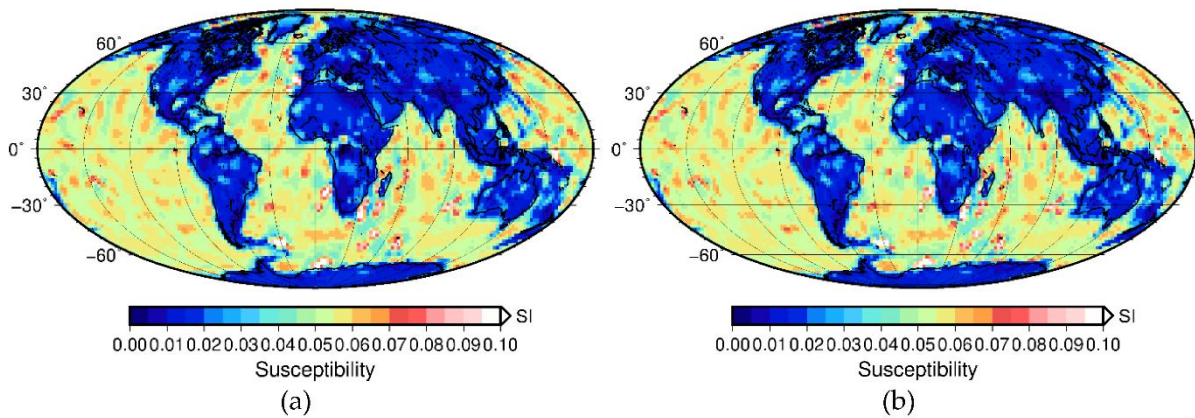


Figure 6.6: Synthetic dataset Inversion result  $\mathbf{x}_A^N$  with the initial guess  $\mathbf{x}_A^0$ . (a)  $\mathbf{x}_A^N$  with  $N=1000$ . (b)  $\mathbf{x}_A^N$  with  $N = 10000$ .

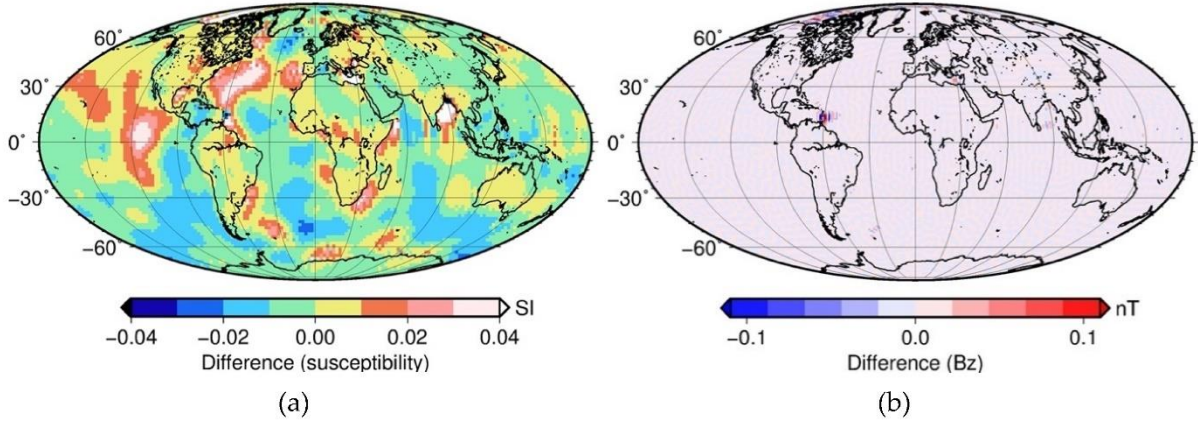


Figure 6.7: Difference grids for the inversion with the initial guess  $\mathbf{x}_A^0$  with averaged values for continental and oceanic crust (Figure 6.2b). **(a)** Difference between the true mode  $\mathbf{x}_H^0$  (model from Figure 6.2a, not initial guess  $\mathbf{x}_A^0$  from Figure 6.2b) and the inversion result  $\mathbf{x}_A^N$ , where  $N = 10000$  is the number of iterations. **(b)** difference between the synthetic truncated observed magnetic field component  $B_z$  (from Figure 6.3b) and truncated forward calculated component  $B_z$  of the inversion result  $\mathbf{x}_A^N$ .

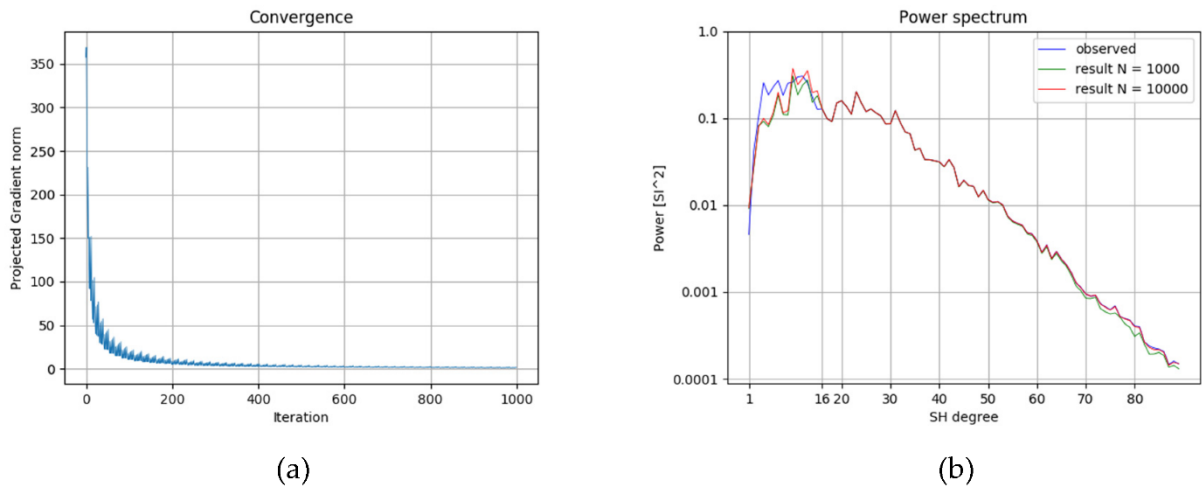


Figure 6.8: Inversion convergence (values of  $Grad(\mathbf{x}^k)$ ) and spectrums of the synthetic field and the field of the inversion result. **(a)** Values of projected gradient at each iteration (up until iteration  $N=1000$ ). **(b)** power spectrum of the synthetic observed field spherical harmonic model (Figure 6.5a) with all degrees and power spectrum of the forward calculated spherical harmonic model of the inversion result  $\mathbf{x}_A^N$  after  $N=1000$  (green) and  $N=10000$  (red) iterations.

### 6.4.2. Inversion of LCS-1

For the inversion with real data, we again choose VIS based model  $\mathbf{x}_H^0$ . The geometry of the model is the same as in the synthetic example and we only replace the synthetic data set with the observed lithospheric magnetic field.

For the inversion, we invert LCS-1 directly and after removing the remanent field as additional a-priori parameter.

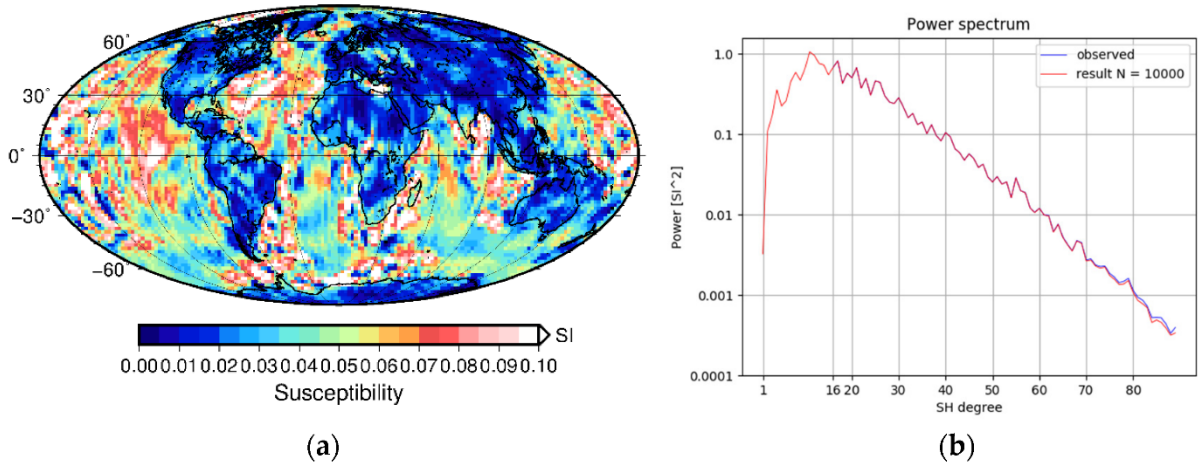


Figure 6.9: Inversion result and spectrums. (a) Inversion result  $\mathbf{x}_{LCS}^N$  with the initial guess  $\mathbf{x}_H^0$  after  $N = 10000$  iterations. (b) power spectrum of LCS-1 and power spectrum of the forward calculated spherical harmonic model of the inversion result  $\mathbf{x}_{LCS}^N$  after  $N=10000$  iterations.

Inversion result is shown on the Figure 6.9a, and the comparison of the result's spectrum against the original LCS-1 on the Figure 6.9b. RMS of the difference between the observed truncated field and forward calculated truncated field of the result  $\mathbf{x}_{LCS}^{N=10000}$  is 0.03938 nT.

## 6.5. Discussion

### 6.5.1. Performance of Inversion

A synthetic inversion case with averaged susceptibilities for oceanic and continental crust as an initial guess ( $\mathbf{x}_A^0$ ) showed that powers of spherical harmonic degrees for  $N=1000$  iterations are overall lower than for  $N=10000$  iterations (see Figure 6.8b).

A minimal value for the linear norm of projected gradient after  $N=10000$  iteration is approx.  $2157.838 \times 10^{-4}$  (iteration 9999), which is two magnitudes higher than the threshold estimated in the very first test.

A higher number of iterations appears to increase the number of artifacts in the inversion result (see Figure 6.6 for example), which can be attributed to the existence of short-wavelength anomalies (with wavelength approx. close to 1 degree) in the input that cannot be caused by  $2^\circ \times 2^\circ$  tesseroids. Thus, the issue is a regularization problem, which is not discussed here.

### 6.5.2. Use of a-Priori Model

Our results confirm that good a-priori model for long-wavelength anomalies is necessary for accurate results. Currently, the existing dataset that can be used as an initial guess for the inversion of real data is Hemant VIS-based model  $\mathbf{x}_H^0$ .

Since synthetic inversion for the initial guess which is different from the true model showed deviation in long-wavelength below degree  $n = 16$ , one cannot expect that long-wavelength sources were

recovered correctly in the inversion result (Figure 6.9). A similar conclusion was made in (Vervelidou and Lesur 2018).

This is especially evident for the inversion results where the initial model by Hemant and Maus (2005) does neither represent the detailed surface geology nor a realistic susceptibility model due to the absence of such information (e.g., parts of Africa and Antarctica). The inversion does change the initial guess and leads to a further refinement of the sources, but, apparently, the amplitude stays as low as possible to fit the short-wavelength.

The application to the Bangui anomaly (Figure 6.10 and Figure 6.11) shows how the inversion changes the initial susceptibility model by adjusting the local values. Clearly, the choice of the a priori information largely influences the inversion results. Therefore, defining the a priori model with uncertainties could lead to further improvement by adding a stochastic element to the inversion. However, such a model does not exist on a global scale.

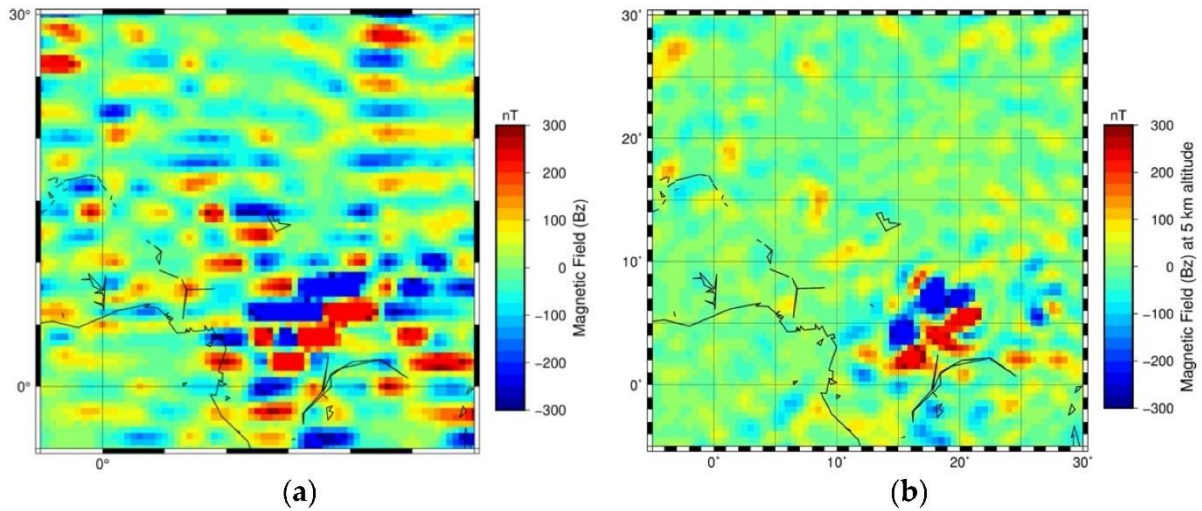


Figure 6.10: Magnetic field of tile inversion result and LCS-1 at the airborne altitude: (a) forward calculated field of the inversion result at 5km altitude. (b) LCS-1 calculate at 5km altitude.

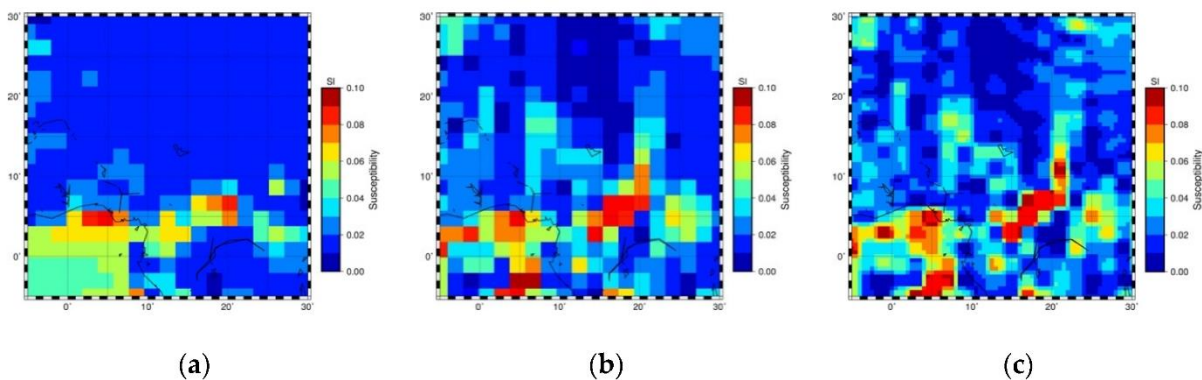


Figure 6.11: Susceptibility models for Bangui area in Africa: (a) Initial guess  $\mathbf{x}_H^0$ . (b) Inversion result  $\mathbf{x}_{LCS}^{N=10000}$ . (c) Tile inversion result with resolution of 0.5 degrees.

Therefore, an alternative would be to use actual rock susceptibility measurements and their statistical properties. Databases of such measurement exist for Norway ([Olesen et al. 2010](#)), Fennoscandia ([Korhonen et al. 1999](#)) and Canada ([Enkin et al. 2020](#)) and can be used to provide an initial guess of a mean susceptibility and its standard deviation. A refined inversion could be done for those areas to explore the influence by a priori information with more detail.

### 6.5.3. Layering of the Model

Another shortcoming of our current models is that the vertical structure of the crust is not well expressed by a single layer. Measurements from outcrops may not adequately represent the entire crust anomaly since the susceptibility of rocks beneath the surface might be different. Therefore, further developments could be adding more information on the crustal structure from seismic information or models like CRUST 1.0. For example, Hemant and Maus ([2005](#)) have based their model on a classification of the ratio of magnetization in the upper and lower crust. The lower crust is, in general, assumed to be less magnetic than the upper crust. However, the most prominent satellite lithospheric anomalies can be expected to have a significant contribution from the lower crust or even the upper mantle ([Idoko et al. 2019](#)). Therefore, one of the next steps should be to add the possibility of layering the crust and to modify the inversion for this. While this is already possible with the current set-up, one has to consider depth-weighting or regularization or the use of aeromagnetic data in the inversion.

### 6.5.4. Regularization

The other solution to help the inversion resolve long-wavelength sources more realistically is to make a stochastic inversion, which would control lower degree power spectra at each iteration. Such an approach would still require an initial guess for power spectra of lower degrees ([Thébault and Vervelidou 2015](#)), derived from the field of an a-priori initial susceptibility guess/model. Control over power spectra would result in the appearance of long-wavelength anomalies in the result, which would correspond to highlighted spherical harmonic degrees.

Such measures would impose implicit regularization on the inversion. Explicit regularization in the inversion, such as a way to guarantee smoothness of the result, may be detrimental to fitting a shorter wavelength. Figure 6.6 shows that the  $N = 10,000$  solution, which is less smooth than the  $N = 1000$  solution, fits the short-wavelength spectrum better. We do not discuss explicit regularization in the inversion further because we expect to use the tile-wise approach later to refine the result.

### 6.5.5. Application to Airborne Data—Proof of Concept

While there are many potential ways to enhance the analysis, the current model can already be used as a reference in modelling regional data. For areas on a regional or local scale, the current model can

be used for the surrounding areas to avoid edge effects, but might also serve as a first guess for the model domain.

A tile-wise approach can be applied, when we select a moving window-tile and calculate the field from the areas surrounding this tile using susceptibilities from the global inversion. Then, we can subtract this far-field effect from the observed field and repeat the inversion for this tile with higher resolution.

Usage of tesseroids as sources instead of dipoles allows scalability of the method, and this approach can be used for the inversion of airborne data. In addition, inversion results can be tested against airborne data, which can be helpful to refine inversion results and models in the future.

As a proof of concept, we demonstrate the results of the tile-wise inversion with grid and tesseroid model resolution of 0.5 degrees for the Bangui Anomaly area. We have chosen this area because it features the most prominent anomaly at satellite height. Although remanence was proposed as a primary source for this anomaly ([Ravat et al. 2002a](#)), that is not necessarily true and depends on the geophysical data used as a constraint. For the demonstration of the concept, the nature of the anomaly is secondary.

We used data without a remanent field from Figure 5.4b, and removed the forward calculated surrounding field as an input.  $\mathbf{x}_{LCS}^{N=10000}$  is used as an initial guess for tile inversion. The forward calculated field of the inversion result at the airborne altitude (5 km) is shown in Figure 6.10 against the original LCS-1 (up to 179°). One can see that the field on the airborne altitude was recovered through the inversion of the data on the satellite altitude, even though there are artifacts related to discretization (Figure 6.10b).

Figure 6.11 shows the process of refinement of the results for Bangui area. Figure 6.11a demonstrates the initial assumption  $\mathbf{x}_H^0$ , while Figure 6.11b shows the global inversion result with LCS-1 data (from Section 6.4.2). Lastly, Figure 6.11c shows the tile inversion for this area with the resulting Figure 6.11: Susceptibility models for Bangui area in Africa: (a) Initial guess  $\mathbf{x}_H^0$ . (b) Inversion result  $\mathbf{x}_{LCS}^{N=10000}$ . (c) Tile inversion result with resolution of 0.5 degrees.b as an initial assumption.

## 6.6. Conclusions

We developed an approach for global high-resolution inversion of satellite magnetic data using spherical harmonic models of tesseroids. Our method utilizes algorithms from the SHTools ([Wieczorek and Meschede 2018](#)) package to convert forward calculated grids of tesseroids into spherical harmonic models and Projected Gradient ([Lin 2007](#)) to perform the inversion.

Our approach is compared to classical spherical harmonic approaches that are very versatile and easily allows us to couple different geophysical, voxel-based approaches. For example, it can be easily linked

to the LitMod3D software (Fullea et al. 2009), which is a popular software for integrated geophysical and petrological modelling of the lithosphere.

Using the developed approach, we investigated caveats of the global magnetic inversion. One major finding was that selection of a-priori information, i.e., susceptibility distribution in the crust, significantly affect the long-wavelength part of the inversion results for a forward calculated magnetic field.

There are two possible ways to ensure more accurate inversion results. The first one is to enforce a particular power for lower degrees via stochastic inversion in order to fit some suggested low-degree power spectra. The other option is to use measured susceptibilities across the globe to set up a more accurate a-priori model. However, the global model presented in this paper can already serve as a background model for more detailed local modelling studies.

## Chapter 7

# Global magnetic susceptibility inversion and robustness estimation

### 7.1. Introduction

The total magnetization of a source can be divided into induced and remanent components. Due to the relatively weak geomagnetic field, the induced magnetization is proportional to the inducing field so that the magnetic susceptibility is considered to be a scalar quantity. In contrast, remanent magnetization is proportional to the ancient field at the rock formation or when a major modification took place ([Clark 1997](#)).

As a rule of thumb, crustal magnetization is generally assumed dominated by induced magnetization over the continents and remanent magnetization over the oceans ([Maus and Haak 2002](#)). The oceanic crust is more mafic than the continental crust in composition. As a result, there is magnetic susceptibility contrast between the continents and the oceans. Statistical analysis of satellite magnetic data shows a negative mean susceptibility contrasts of the oceans and the positive mean contrast within the continents ([Hinze et al. 1991](#)). Although there is relatively high remanent magnetization over the oceans, it is safe to ignore the contribution of remanent magnetization over the continents, especially in cratonic areas where the Königsberger ratio  $Q$ , which is defined as relative importance of remanent to induced magnetization ([Hinze et al. 1991; Arora et al. 2011](#)), can be considered as  $Q \ll 1$ . The susceptibility inversion should result in positive values over the continents and allow some negativity in the oceans.

Several results have been developed for the global induced magnetization estimation. A Standard Earth Magnetization Model (SEMM) was developed with an a priori continent-ocean contrast ([Purucker et al. 1998](#)). A simplified reference model SEMM-0 that a priori susceptibility values were assigned to continental and oceanic crust and remanent magnetization to Cretaceous Quiet Zones (KQZ) was modified to fit the satellite driven anomaly data from POGO and Magsat. The modified result is a vertical integrated susceptibility (VIS) which is defined as susceptibility times thickness. This model was updated by adding a remanent magnetization model and using new satellite data from the Ørsted satellite mission ([Purucker et al. 2002](#)).

Hemant and Maus ([2005](#)) developed a global magnetization model based on geological, petrological and seismic thickness information. This model was derived in two steps. First, the whole globe was divided into different geological regions and an average maximum susceptibility value was calculated and assigned to the individual regions. Then, the stratigraphical thickness from a seismic model, for each geological stratum within the vertical column, is multiplied by the average susceptibility of that

stratum. The crustal field from the VIS model was approximated by equivalent dipoles distributed at the Earth's surface. Although the predicted field of VIS model presents an overall agreement with CHAMP satellite data over the continent, there are discrepancies over oceanic regions and for certain areas on the continents, for example west Australia, south Africa and Antarctica. It may be due to either simplified dipole forward method or the a priori information used to derive the VIS model. Because the geological knowledge used to calculate average maximum susceptibility may reflect the magnetic properties of upper crust materials only. As a consequence, the VIS model suffers from a systematic bias as the susceptibility information of deep crustal structures are not taken in to account. Vervelidou and Thébault (2015) estimated the induced magnetization with the Revised Spherical Cap Harmonic Analysis (R-SCHA) technique. This approach calculated regional power spectrums of 2000 spherical caps distributed on the nodes of a global equal area grid with 15° radius respectively. As a result, the estimated vertical integrated magnetization was derived from the regional power spectrum. Although this method can provide global distribution of the induced magnetization information, the results are not equally reliable globally due to the inhomogeneous data quality in each spherical cap. Giving the availability of new satellite data (LCS-1) and the geology-based a priori susceptibility model from Hemant and Maus (2005), a global magnetic susceptibility model was developed. This chapter is a succession of the previous chapter, which aims to provide an approximately 1° resolution magnetic susceptibility model which is assumed to be purely induced.

## 7.2. Data and Methods

Forward calculation and inversion methods are the same as in the previous chapter. The only difference is that the sensitivity matrix now consists of the filtered Bz component of the individual tesseroids. In addition to that, the magnetic crust is defined by two layers, a sediment layer as upper boundary and the Moho discontinuity as bottom (Laske et al. 2013; Szwillus et al. 2019). They were discretized in roughly 1° (the median of 0.96°) equidistant tesseroids (Leopardi 2006; Baykiev et al. 2016). Since the inversion is for global induced susceptibility, the contribution of remanent magnetization was subtracted from the LCS-1 data (Masterton et al. 2013; Olsen et al. 2017). Together with the VIS model (Hemant and Maus 2005) and the geometry of the tesseroids (Laske et al. 2013; Szwillus et al. 2019), an a priori susceptibility model was calculated to serve as an initial guess for the iterative inversion method (Lin 2007).

The linear system  $Ax=b$  was solved iteratively with a projected gradient method. The sensitivity matrix  $A$ , which has a size of 45000 by 45000, consists of the Bz component of each tesseroid with respect to the distance between the satellite height 400 km and the tesseroids center point. The observables in  $b$  were calculated by subtracting the remanent magnetization field of the oceanic crust from the satellite field of LCS-1 at 400 km height (Figure 7.1). The sensitivity matrix  $A$  and the remanent

magnetization field of the oceanic crust were filtered using the software package SHTools to match the spectral range of LCS-1 of SH degree 15-185.

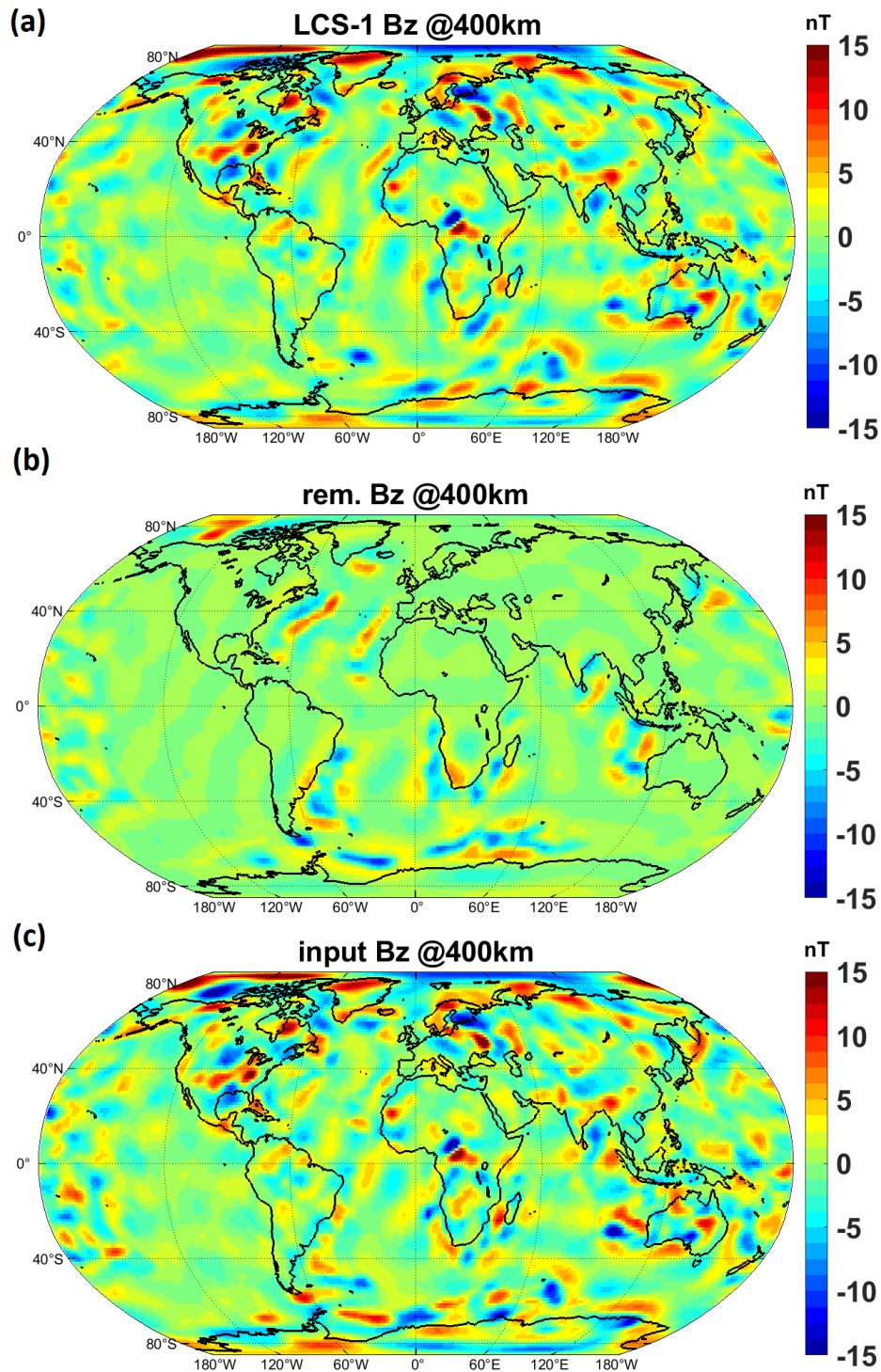


Figure 7.1: (a) LCS-1 Bz component calculated at 400 km (b) Bz component of the remanent magnetization at 400 km (c) subtract (b) from (a) as the contribution of the induced magnetization

### 7.3. Results

To illustrate the effectiveness of geologically determined VIS as an a priori information, the inversion was carried out with respect to four different scenarios where four distinct initial values (Figure 7.2)

were used to solve the linear system  $Ax=b$  described in the previous section. The initial guess of 0 and 0.1 were chosen to reflect two extreme cases of non-magnetism (e.g. typical sedimentary rocks) and high-magnetism (e.g. typical igneous rocks). Since there is a systematic difference between magnetic susceptibility in continents and oceans, 0.02 was assigned to the continents and 0.04 to the oceans as an initial guess (McEnroe et al. 2018; Purucker and McEnroe 2014). The last one was selected to be magnetic susceptibility calculated from VIS data and model geometry bounded by the bottom of the sedimentary layer and the Moho.

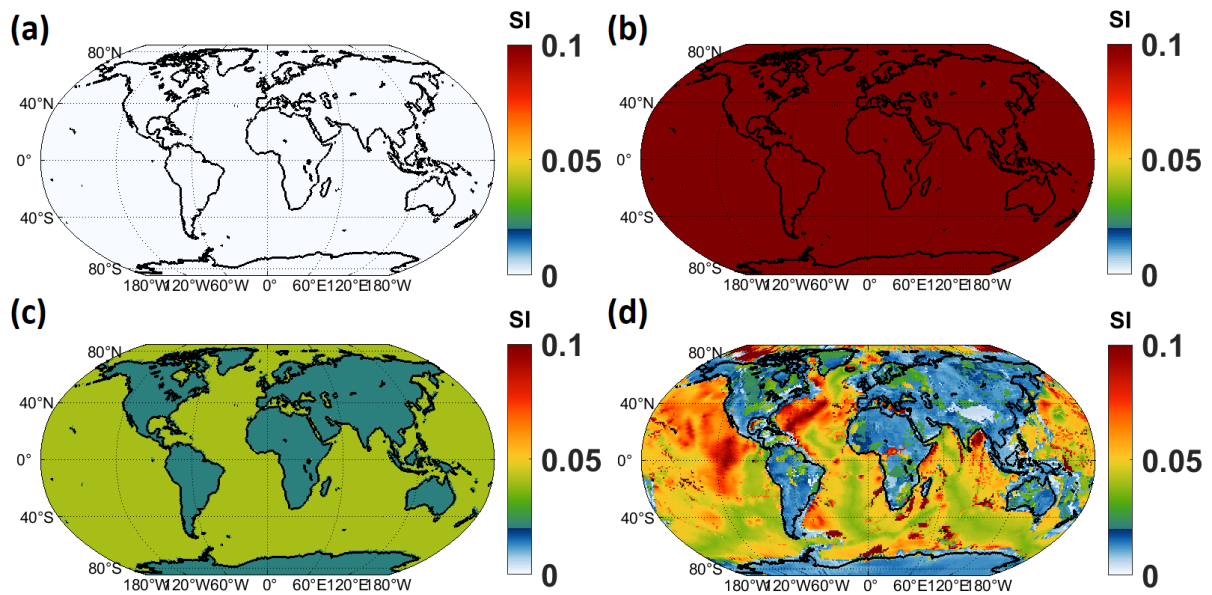


Figure 7.2: A priori for inversion. (a) initial values of zero (b) initial values of 0.1 (c) 0.02 for continents and 0.04 for oceans (d) magnetic susceptibility calculated from VIS data and model geometry

The RMS misfit map shows typical L-shaped curves that the misfit decreases very fast at the beginning and relative slow after thirty thousand iterations (Figure 7.3). Therefore, the inversion results of last twenty thousand iterations were chosen to calculate the mean susceptibility to represent the relatively same inversion results in terms of misfit level (Figure 7.4).

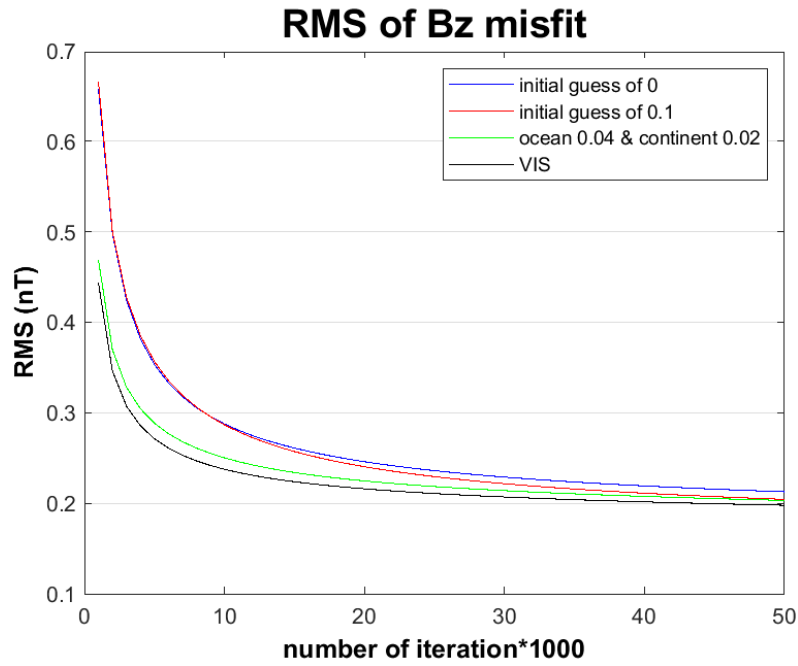


Figure 7.3: Root mean square (RMS) residuals between input data and predicted field at 400 km height

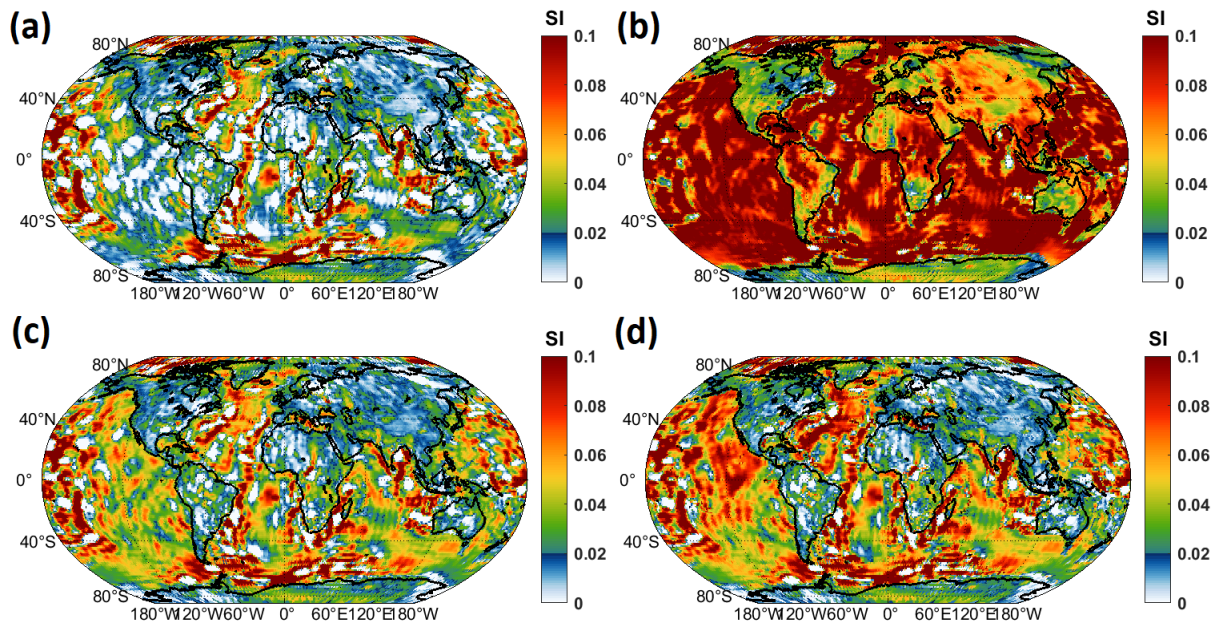


Figure 7.4: Average magnetic susceptibility (last twenty-thousand iterations) from inversion using different a priori information (a) initial values of zero (b) initial values of 0.1 (c) 0.02 for continents and 0.04 for oceans (d) magnetic susceptibility calculated from VIS data and model geometry

To assess the robustness of the inverted susceptibility, the standard deviation of the susceptibility at each grid point was calculated using the results from the last twenty thousand iterations. Although the last twenty thousand iterations show a relative same misfit level, the inverted susceptibilities over the continents are more robust than over the oceans except for the model with an a priori value of 0.1.

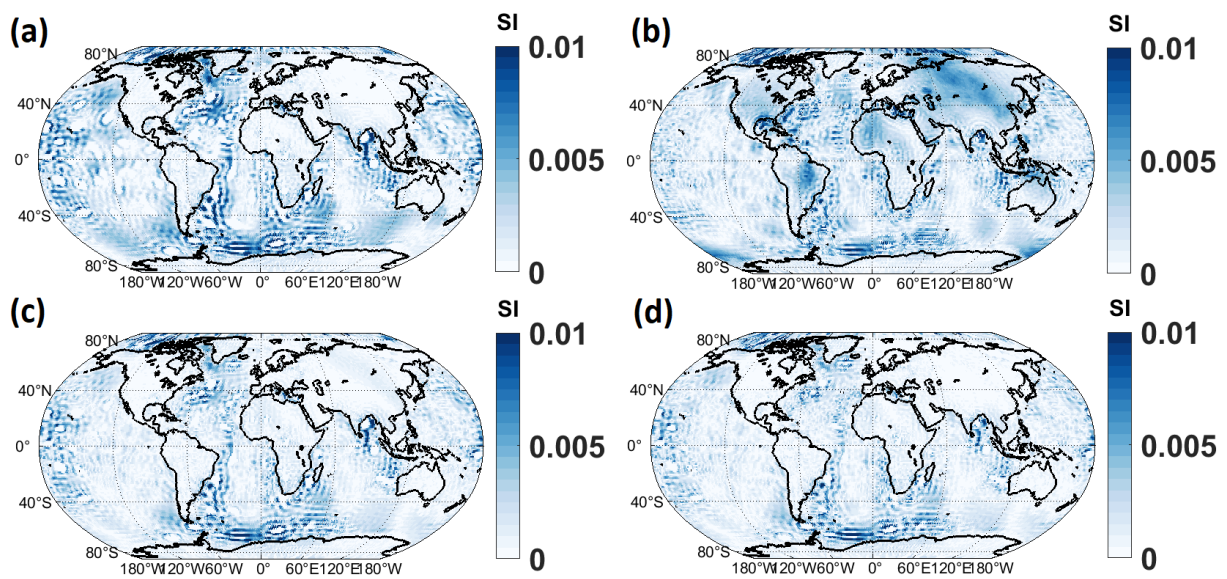


Figure 7.5: Standard deviation of magnetic susceptibility (last twenty-thousand iterations) from inversion using different a priori information (a) initial values of zero (b) initial values of 0.1 (c) 0.02 for continents and 0.04 for oceans (d) magnetic susceptibility calculated from VIS data and model geometry

To illustrate the inverted susceptibility result in a regional area, results over Australia, southern Africa and Antarctica are shown in Figure 7.6-Figure 7.9.

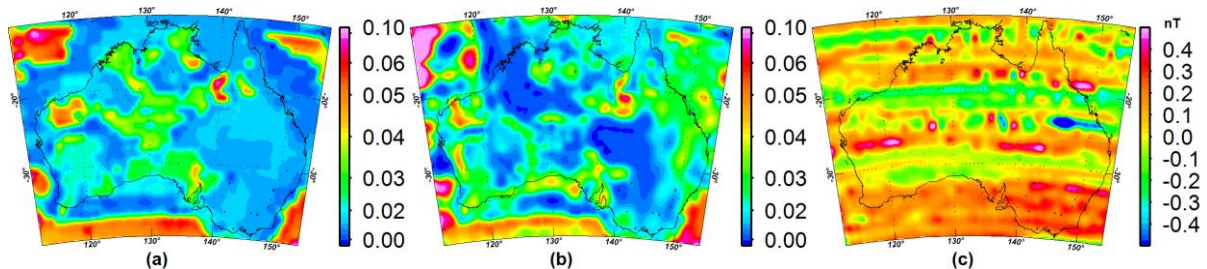


Figure 7.6: Comparison of initial susceptibility model and inverted mean susceptibility (last twenty-thousand iterations) over Australia. (a) magnetic susceptibility calculated from VIS data and model geometry (b) inverted susceptibility using (a) as a priori (c) misfit map

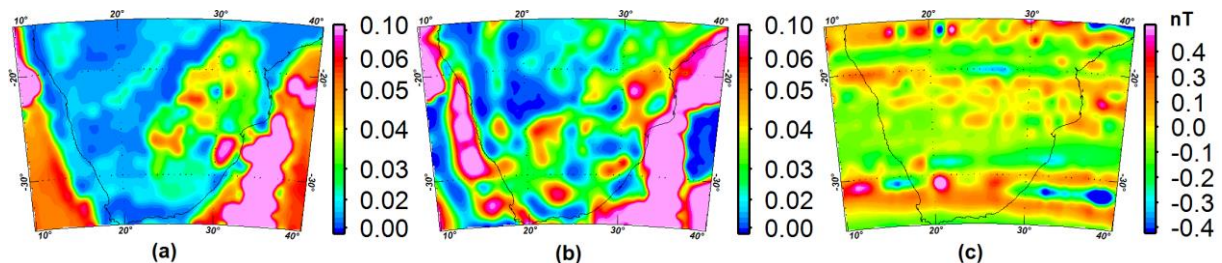


Figure 7.7: Comparison of initial susceptibility model and inverted mean susceptibility (last twenty-thousand iterations) over southern Africa. (a) magnetic susceptibility calculated from VIS data and model geometry (b) inverted susceptibility using (a) as a priori (c) misfit map

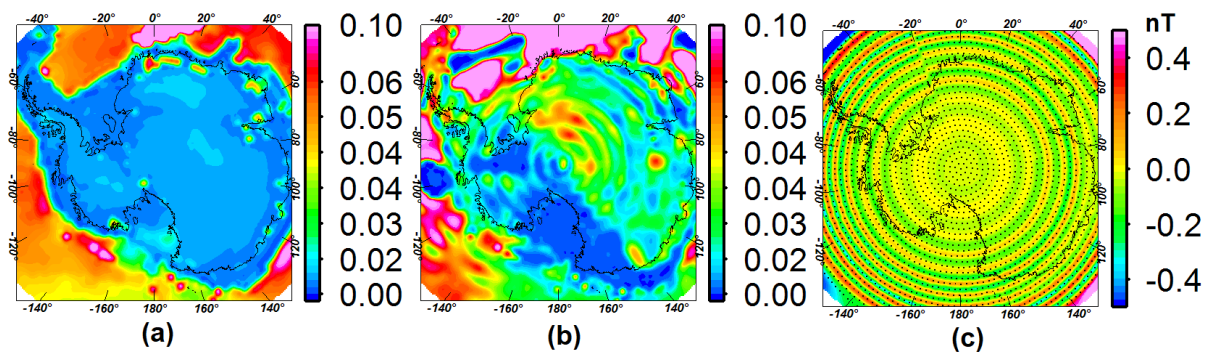


Figure 7.8: Comparison of initial susceptibility model and inverted mean susceptibility (last twenty-thousand iterations) over Antarctica. (a) magnetic susceptibility calculated from VIS data and model geometry (b) inverted susceptibility using (a) as a priori (c) misfit map (the center point of the sources shown as black dots)

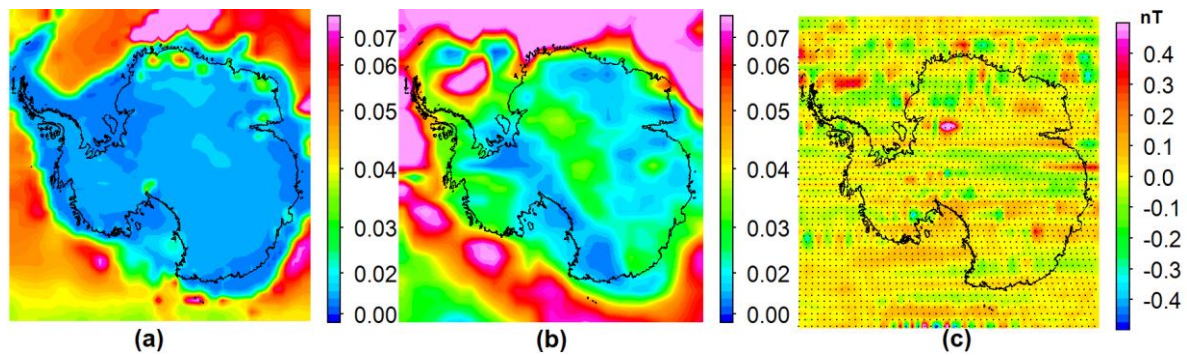


Figure 7.9: Comparison of initial susceptibility model and inverted mean susceptibility (last twenty-thousand iterations) over Antarctica which was rotated to the equator. (a) magnetic susceptibility calculated from VIS data and model geometry (b) inverted susceptibility using (a) as a priori (c) misfit map (the center point of the sources shown as black dots)

Finally, the inverted susceptibility values were linked together in a Gondwana framework (Figure 7.10). The magnetic susceptibility in the oceans is excluded and the neighboring continents of Antarctica through geological time are presented together with Antarctica using open-source software [GPlates](#).

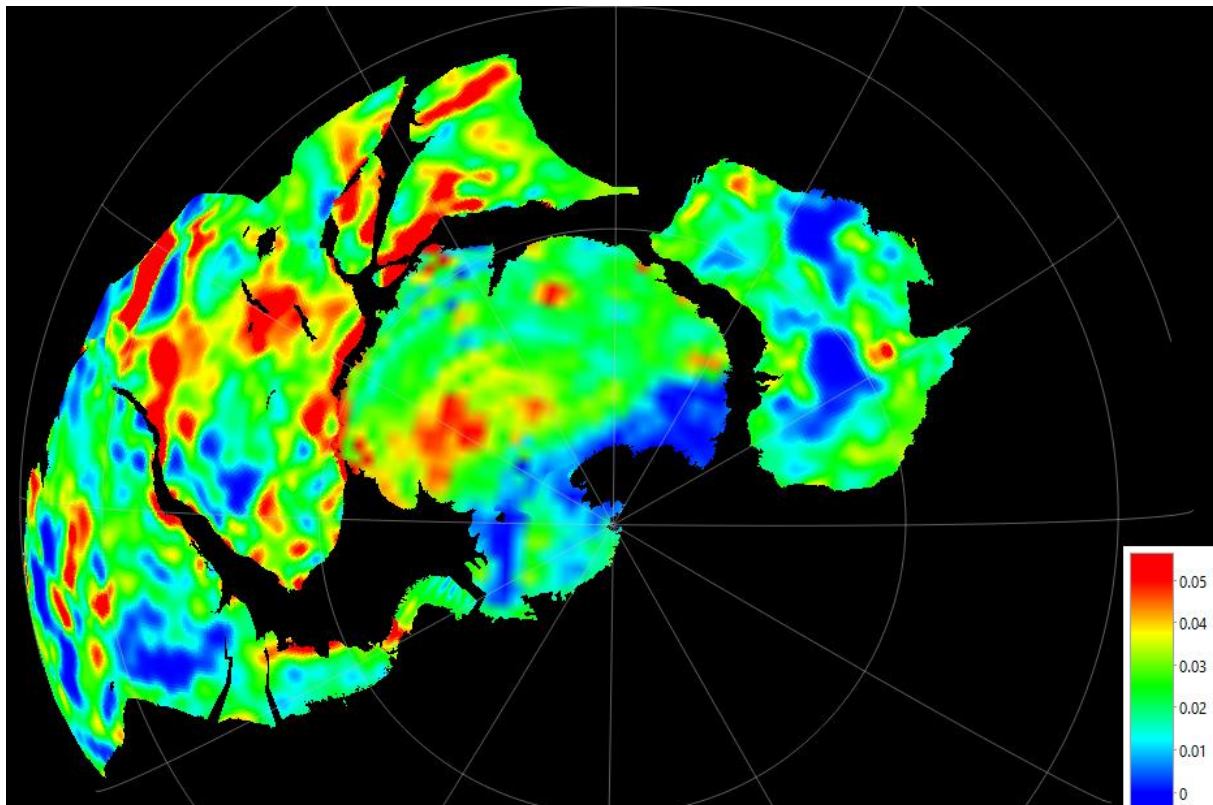


Figure 7.10: Plate-tectonic reconstruction at 166 Ma ago (inverted mean susceptibility)

#### 7.4. Discussion

The RMS value for the misfit between input data and predicted data at 400 km shows typical L-shaped curves and all 4 starting models reach a same level of misfit (with an RMS of ca. 0.2 nT). Due to the non-uniqueness in geophysical inversions, all 4 cases can explain the input data equally well in terms of data misfit. Therefore, a priori information is critical to reduce the non-uniqueness in the inversion and it has to be carefully chosen.

Constant values of 0 and 0.1 (case 1 and 2) seem to be too simple and not realistic since there is plenty of evidence to support the lateral variation of magnetics in the crust. Although the case 3 did not consider the lateral variation inside the continent or the ocean, it did allow for the systematic difference between the ocean and continent in magnetics. Interestingly, the result from case 3 has a good agreement in the overall patterns with case 4 which has a more sophisticated a priori model primarily derived from surface geology. In addition, the RMS misfit map also indicates that the VIS data serves as a better a priori information because it always leads to smaller RMS values than the other 3 cases. Furthermore, the minimum level of ca. 0.2 nT is consistent with the estimated data uncertainties for the North-South gradient of CHAMP and Swarm satellite data (Olsen et al. 2017, Fig 3). As shown in Figure 7.5, the variations of inverted susceptibilities over the continents are smaller than in the oceans, except for case 2 in Figure 7.5b. This is due to the fact that susceptibilities in the continents

are dominated by induced magnetization. Patterns of high variation in the ocean, which is presented in dark blue, are in good agreement with the patterns of the remanent magnetization field of the ocean (Figure 7.1b). This may imply that the oceanic remanent magnetic field model is too simple to represent its actual contribution to the crustal field. Due to the nature of the potential field, subtracting the contribution of the remanent magnetization mainly affects the result in oceanic area but gives more robust result over the continents.

The initial VIS model from Hemant and Maus [2005](#) is biased towards the upper crust because there is little direct information about the lower crust susceptibility. This model mathematically extrapolates the geology-based susceptibilities from upper crust to lower crust. Thus, the initial model mainly reflects the geological information of the shallow crust. A comparison between the inverted susceptibility and the initial susceptibility model shows that the magnitude of susceptibility values is in the same range but the patterns are different, except for some oceanic areas where the initial model might reflect the susceptibility of whole oceanic crust. The difference in patterns demonstrated in the three regional areas are shown in Figure 7.6-Figure 7.9.

For Australia, the VIS model shows high susceptibility values in the central part and relative low values in the eastern and south western part. However, inverted result shows two ultra-low susceptibility areas which are consistent with the patterns of the satellite data.

For southern Africa, the VIS model reflects a strong contrast between the continent and ocean. However, the inverted result only shows high contrast along the east coast. Over the continent, the inverted susceptibility map fails to reveal a regular pattern. Probably, this is the effect of remanent magnetization which is quite strong along the coastline and also extends further towards the continent (Figure 7.1b). Similarly, a high variation of inverted susceptibility can be seen in southern Africa (Figure 7.5d).

For Antarctica, the most interesting result emerged from the inversion. As shown in Figure 7.8, there is a systematic separation between East and West Antarctica that low susceptibility values appear in West Antarctica and relatively high values in East Antarctica. This contrast correlates well with a previous study of satellite gravity data ([Ebbing et al. 2018](#)). However, the inverted susceptibility map and misfit map show ring-like patterns which are correlated with the discretization of the magnetic sources (Figure 7.8b and c). To reduce this effect, the susceptibility inversion was carried out again with the same parameters where Antarctica was rotated to the equator (i.e. rotation about y axis by 90° with respect to ECEF coordinate system). As shown in Figure 7.9, the dramatic ringing patterns related to source discretization in polar area were completely changed. Consequently, Figure 7.9b should reflect the more reliable magnetic susceptibility patterns than Figure 7.8b for Antarctica.

For the Gondwana framework, in addition to the apparent susceptibility contrast between East and West Antarctica, there are some structures extended from coastal area to India and south Africa. There is no abrupt susceptibility jump cross Antarctica and Australia for the most part. However, there is an exception showing no direct connection between the ultra-low susceptibility structures across South Eastern Australia and West Antarctica. Although there is no visible connection between these two structures over the continents, the link between these two could hide in the ocean as shown in Figure 7.6b that the low susceptibility structure extends to the off-shore part of Southern Australia.

## 7.5. Conclusions

In this chapter, a global  $1^\circ$  induced susceptibility model was calculated with respect to the LCS-1 satellite model where the effect of remanent magnetization was subtracted. The Projected Gradient iterative inversion method was applied to assure positive susceptibility values. The usage of geology-based VIS data as an a priori outperforms the relatively simple starting models in terms of RMS misfit. The variation of the inversion result shows that inversion result in continental settings is quite robust due to the low standard deviation of the last twenty thousand iterations. The patterns of the high standard deviation in the oceans are consistent with the patterns of remanent magnetization field, which suggests that a high-resolution local inversion in continental areas is possible. The result in Antarctica demonstrates the usefulness of this susceptibility model that provides insight into interior structure of remote regions where it is difficult to conduct direct geophysical investigation.

## Chapter 8 Conclusions and Outlook

### 8.1. Summary

Due to the uniform global coverage and high accuracy, the magnetic crustal model (LCS-1) derived from satellite magnetic observations can provide a highly reliable long-wavelength reference model for crustal magnetic field. This thesis discussed several applications of satellite magnetic data. The aim of this thesis was to answer the three questions introduced in Chapter 1 :

- *Q1: Since the satellite data/models can provide a reference for reliable long-wavelength component of the crustal magnetic field, how can we make use of them to analyze and improve the long-wavelength part of the aeromagnetic compilations?*
- *Q2: Since the satellite data/models can provide a global-scale coverage of magnetic data, how can the present-day data help us to link the continents at geological time-scale?*
- *Q3: How can we derive a meaningful magnetic susceptibility distribution of the crust from the satellite data/models?*

These three questions correspond to three scientific papers. There are three supplementary chapters closely related to these three papers. The following conclusions are drawn on the basis of these six chapters:

- Since aeromagnetic data and satellite data are measured at significantly different height level (~100 m VS ~100 km), two sets of data attenuate disproportionately in spectral domain. Therefore, spectral methods are used to analyze and combine them together. Among them, the classical Spherical Harmonics is only suitable for global data sets due to the orthogonality of the basis functions. For regional data sets, conventional methods like Fourier domain filtering and Slepian functions suffer from spectral leakage from the high-frequency part of the broad-band signal into low-frequency part so that they fail to extract the same spectral information as Spherical Harmonics. As a result, they can only provide qualitative long-wavelength patterns compared to the satellite data. On the other hand, the new method described in Chapter 3 is a practical tool for analyzing spectral consistency between near-surface and satellite data because this physics-based method makes it possible to decompose these two sets of data into the spherical harmonic domain. By utilizing this method, the regional spherical harmonic power spectrum was analyzed for three consecutive versions of magnetic anomaly maps of Australia. The result confirmed the previous estimation about the spectral improvement of the 4th generation of magnetic anomaly map of Australia by the individual AWAGS (Australia Wide Airborne Geophysical Survey) data. It showed that the “spectral gap” between 3rd generation and 4th generation was in the range of spherical harmonic degree 40-110 (corresponding to spatial resolution of 180-500 km), whereas the previous rough estimation was in the range of 100-500 km. In addition,

the long-wavelength difference between LCS-1 and AWAGS contribution suggested that there is a systematic pattern related to the positions of the ground-based magnetic stations which can be explained by inconsistent diurnal correction for AWAGS data. Furthermore, the long-wavelength part of the magnetic compilation of Australia still could be improved by satellite data because satellite data can provide more consistent data in accuracy and coverage than AWAGS data.

- Since strength and direction of the core field vary by location, the response of same magnetic material at different location would be different. To normalize the effect of the spatial variation of the core field, the reduction to the pole (RTP) transformation can be used. As a result, RTP transformed magnetic data directly reflect the crustal magnetic sources without mixing with the dependence of magnetic data on the core field direction and strength. Technically, due to the high demand for computer power (mainly memory), RTP transformation of LCS-1 data was carried out in tile-wise manner. The BiCGSTAB iterative method applied to a normal equation  $A^T Ax = A^T b$  resulted in a plausible result with the misfit to the three vector components of LCS-1 data being negligible in the tiles and relatively small along the tile boundaries. The reduction to the pole LCS-1 data can provide a link between historically adjacent continents in the Gondwana frame. It becomes important when there are no aeromagnetic data to link the Indian-Antarctic connection. Consequently, the RTP corrected LCS-1 data suggest that there is a continuation of the Indian geological provinces under the Antarctic ice. Furthermore, together with long-wavelength corrected aeromagnetic data using the method introduced in Chapter 3, they will lay the base for further studies of geological interpretation for regional structures.

- The major aim of magnetic data processing is to convert them to magnetic sources' parameter (i.e. magnetic susceptibility) for further geological interpretation. In this thesis, two globally induced susceptibility models were derived from LCS-1 satellite magnetic in 1° and 2° resolution, respectively. The strategies behind these two inversion results (1° and 2° resolution) are fundamentally the same. A tesseroïd-based algorithm was used for magnetic forward modeling regarding the sphericity of the surface. A positive-constrained iterative method, namely projected gradient, was adopted for inversion. For the 2° case, the inversion result has a very low misfit level and spectrally agrees very well with the LCS-1 model. It implies that the inversion result can provide a global reference model for induced susceptibility. For the 1° case, the inversion result shows that this susceptibility model might be more robust for continental areas due to the low variability in the iterative steps. It indicates that the effect of remanence magnetization appears to be limited to oceans. Furthermore, it is possible to neglect this effect in regional areas in continents for high-resolution susceptibility inversion. Take, for example, the region of Antarctica, where the 1° inversion shows a significant magnetic difference between West and East Antarctica.

## 8.2. Possible future tasks

- For regional spherical harmonic analysis, the magnetic anomaly data of aeromagnetic compilations are assumed to be harmonic, which means that, one component of the crustal field points in the direction of main field. However, it is a simplified situation to guarantee an easy-to-handle linear system. In actuality, it is a non-linear inversion problem. Although this simplification gives a satisfactory result for Australia, it is better to include the non-linear effect for future studies for other areas.
- Regarding the reduction to the pole correction, although the misfit along tile boundaries is relatively small, it can introduce a systematic distortion to the RTP data. This is inevitable for tile-wise inversion. However, merging all the tiles into one big sensitivity matrix is also not practical because it requires a huge amount of memory to store the dense sensitivity matrix. One possible way to mitigate this problem is to implement sparsification to the dense sensitivity matrix. Due to the observed magnetic field being inversely proportional to the cube of the distance to the sources, the contribution of the far away sources can be discarded. Therefore, using a certain threshold for distance, the dense sensitivity matrix can be converted to a sparse matrix without becoming physically implausible. In addition, sparsification also can be used for regional spherical harmonic analysis.
- For globally induced susceptibility inversion, the model geometry is fixed by two boundaries, which are the bottom of the sediment layer and the layer of the Moho discontinuity. As many researchers argued, the Moho is not necessary the bottom of the crustal magnetic sources. However, it is not possible to determine the magnetism of the crustal sources without defining a reasonable model geometry because the magnetic rocks are not distributed everywhere in Earth's interior. The conventional inversion methods have difficulties to simultaneously invert the magnetic parameters and the depth to the magnetic bottom due to the non-uniqueness of the inversion problem. Fortunately, it is possible to bridge the gap between the geothermal observation and magnetic bottom via the Curie temperature of the characteristic iron-bearing rocks. In this circumstances, stochastic inversion approaches are suitable to incorporate a prior information in terms of model and data probabilities in the inversion process. Stochastic inversion approaches can deal with multi-parameter inversion and also estimate the influence of the error inherited from observables. Because stochastic inversion approaches naturally account for the existence of the multiple solutions to the inverse problem and can provide posterior uncertainty analysis. In addition, it allows to integrate the known constrains into the inversion problem effectively. As a result, we can make the best of all possible information (i.e. observables, constraints, error and a priori model) using one stochastic inversion framework which is more flexible. Therefore, stochastic approach is a promising direction to continue the regional susceptibility inversion. With the rise of computational resources, robust and geologically meaningful multi-scale and high-resolution models will become achievable, which take advantage of combining satellite and aeromagnetic data in whole spectrum.

## Appendix

### Appendix I

The magnetic dipole is the elementary building block of magnetic sources. The scalar potential  $\Omega$  of a magnetic dipole is given by (e.g., [Blakely 1996](#)):

$$\Omega(P) = -\frac{u_0}{4\pi} \vec{m} \cdot \nabla_P \left( \frac{1}{d(P, Q)} \right). \quad (\text{A-1})$$

where  $u_0$  is the magnetic permeability of free space;  $\vec{m}$  is the dipole moment and  $d(P, Q)$  is the Euclidean distance between the dipole's center  $Q$  and the observation/calculation point  $P$ . If only induced magnetization is considered, the dipole moment  $\vec{m}$  can be written

$$\vec{m} = \vec{M}V = \chi \vec{H}V = \chi \frac{\vec{B}_c}{u_0} V. \quad (\text{A-2})$$

where  $\chi$  is the magnetic susceptibility;  $\vec{B}_c$  is the inducing field that that is the core field of the earth's magnetic field;  $V$  is the volume of the magnetic source. Substitution of the  $\vec{m}$  into the equation of dipole scalar field gives

$$\Omega(P) = -\frac{\chi V}{4\pi} \vec{B}_c \cdot \nabla_P \left( \frac{1}{|\vec{r} - \vec{s}|} \right). \quad (\text{A-3})$$

where  $\vec{s}$  is directed from Earth's center to the source point  $Q$  and  $\vec{r}$  is to the calculation point  $P$  respectively.  $\vec{B}_c$  can be expanded in the series of spherical harmonics at the source point  $Q$  in local north-east-down coordinate system, that is,

$$\vec{B}_c = \begin{cases} B_c^x = \sum_{n=1}^N \sum_{m=0}^n \left( \frac{a}{S} \right)^{n+2} (g_n^m \cos m\varphi + h_n^m \sin m\varphi) \left[ \frac{d}{d\theta} S_n^m(\cos \theta) \right] \\ B_c^y = \sum_{n=1}^N \sum_{m=0}^n \left( \frac{a}{S} \right)^{n+2} m (g_n^m \sin m\varphi - h_n^m \cos m\varphi) \left[ \frac{1}{\sin \theta} S_n^m(\cos \theta) \right] \\ B_c^z = -\sum_{n=1}^N \sum_{m=0}^n \left( \frac{a}{S} \right)^{n+2} (n+1) (g_n^m \cos m\varphi + h_n^m \sin m\varphi) S_n^m(\cos \theta) \end{cases} \quad (\text{A-4})$$

where  $a$  is the radius of Earth's magnetic reference sphere (6371.2 km);  $g_n^m, h_n^m$  are the SH coefficients describing the core field up to degree  $n$  and order  $m$ ;  $\varphi, \theta$  are the longitude and colatitude of the source point  $Q$  and  $S_n^m(\cos \theta)$  is the Schmidt quasi-normalized spherical harmonics of degree  $n$  and order  $m$ .

To derive spectral representation of  $\Omega(P)$ , the inverse distance between two vectors  $\vec{r}$  and  $\vec{s}$  needs to be expressed in SH expansion. This relation can be given by Spherical Harmonic Addition Theorem (Brooks 2013 B.7). The addition theorem states

$$\begin{aligned} \frac{1}{|\vec{r} - \vec{s}|} &= \sum_{n=0}^{\infty} \sum_{m=-n}^n \frac{4\pi}{2n+1} \frac{s^n}{r^{n+1}} Y_n^m(\theta_r, \varphi_r) Y_n^m(\theta_s, \varphi_s)^* \\ &= \sum_{n=0}^{\infty} \sum_{m=-n}^n \frac{4\pi}{2n+1} \frac{s^n}{r^{n+1}} Y_n^m(\theta_r, \varphi_r) (-1)^m Y_n^{-m}(\theta_s, \varphi_s) \end{aligned} \quad (\text{A-5})$$

where  $Y_n^m$  denotes complex spherical harmonics and the superscript \* means its complex conjugate. The relation between real spherical harmonics and their complex analogues are given by

$$Y_n^m = \begin{cases} (y_n^{|m|} - iy_n^{-|m|})/\sqrt{2} & (m < 0) \\ y_n^0 & (m = 0) \\ (-1)^m (y_n^{|m|} + iy_n^{-|m|})/\sqrt{2} & (m > 0) \end{cases} \quad (\text{A-6})$$

where  $y_n^m$  denotes real spherical harmonics. Substituting the complex spherical harmonics with the real form gives

$$\frac{1}{|\vec{r} - \vec{s}|} = \begin{cases} \sum_{n=0}^{\infty} \sum_{m=-n}^n T_n \frac{1}{2} (y_n^{|m|}(\theta_r, \varphi_r) - iy_n^{-|m|}(\theta_r, \varphi_r)) (-1)^m (-1)^m (y_n^{|m|}(\theta_s, \varphi_s) + iy_n^{-|m|}(\theta_s, \varphi_s)) & (m < 0) \\ \sum_{n=0}^{\infty} \sum_{m=-n}^n T_n y_n^0(\theta_r, \varphi_r) y_n^0(\theta_s, \varphi_s) & (m = 0) \\ \sum_{n=0}^{\infty} \sum_{m=-n}^n T_n \frac{1}{2} (-1)^m (y_n^{|m|}(\theta_r, \varphi_r) + iy_n^{-|m|}(\theta_r, \varphi_r)) (-1)^m (y_n^{|m|}(\theta_s, \varphi_s) - iy_n^{-|m|}(\theta_s, \varphi_s)) & (m > 0) \end{cases} \quad (\text{A-7})$$

$$T_n = \frac{4\pi}{2n+1} \frac{s^n}{r^{n+1}} \quad (\text{A-8})$$

It is obvious that the imaginary part of the expansion disappears for same  $|m|$  so that only real spherical harmonics stay, that is,

$$\frac{1}{|\vec{r} - \vec{s}|} = \begin{cases} \sum_{n=0}^{\infty} \sum_{m=-n}^n T_n \frac{1}{2} (y_n^{|m|}(\theta_r, \varphi_r) y_n^{|m|}(\theta_s, \varphi_s) + y_n^{-|m|}(\theta_r, \varphi_r) y_n^{-|m|}(\theta_s, \varphi_s)) & (m < 0) \\ \sum_{n=0}^{\infty} \sum_{m=-n}^n T_n y_n^0(\theta_r, \varphi_r) y_n^0(\theta_s, \varphi_s) & (m = 0) \\ \sum_{n=0}^{\infty} \sum_{m=-n}^n T_n \frac{1}{2} (y_n^{|m|}(\theta_r, \varphi_r) y_n^{|m|}(\theta_s, \varphi_s) + y_n^{-|m|}(\theta_r, \varphi_r) y_n^{-|m|}(\theta_s, \varphi_s)) & (m > 0) \end{cases} \quad (\text{A-9})$$

The real spherical harmonics here are

$$y_n^m = \begin{cases} (-1)^m \sqrt{2} \sqrt{\frac{2n+1}{4\pi} \frac{(n-|m|)!}{(n+|m|)!}} P_n^{|m|}(\cos \theta) \sin(|m|\varphi) & (m < 0) \\ \sqrt{\frac{2n+1}{4\pi}} P_n^{|m|}(\cos \theta) & (m = 0) \\ (-1)^m \sqrt{2} \sqrt{\frac{2n+1}{4\pi} \frac{(n-|m|)!}{(n+|m|)!}} P_n^{|m|}(\cos \theta) \cos(|m|\varphi) & (m > 0) \end{cases} \quad (\text{A-10})$$

where  $P_n^m$  is the associated Legendre functions of degree  $n$  and order  $m$ . Finally,  $\frac{1}{|\vec{r}-\vec{s}|}$  can be written in the Schmidt quasi-normalized real spherical harmonics

$$\frac{1}{|\vec{r}-\vec{s}|} = \sum_{n=0}^{\infty} \sum_{m=0}^n \frac{s^n}{r^{n+1}} S_n^m(\cos \theta_r) S_n^m(\cos \theta_s) \cos(m\varphi_r - m\varphi_s) \quad (\text{A-11})$$

The gradient operator is to be taken with respect to the source coordinates in order to express the dipole field in the coordinates of the calculation point. The relationship between the gradient with respect to the source and with respect to the calculation point is that

$$\nabla_P \left( \frac{1}{|\vec{r}-\vec{s}|} \right) = -\nabla_Q \left( \frac{1}{|\vec{r}-\vec{s}|} \right) \quad (\text{A-12})$$

In spherical coordinates, the gradient of  $\frac{1}{|\vec{r}-\vec{s}|}$  with respect to the source is given by

$$\nabla_Q \left( \frac{1}{|\vec{r}-\vec{s}|} \right) = \begin{cases} \frac{1}{s} \frac{\partial}{\partial \theta_s} \left( \frac{1}{|\vec{r}-\vec{s}|} \right) \\ \frac{1}{s \sin \theta_s} \frac{\partial}{\partial \varphi_s} \left( \frac{1}{|\vec{r}-\vec{s}|} \right) \\ \frac{\partial}{\partial s} \left( \frac{1}{|\vec{r}-\vec{s}|} \right) \end{cases} \quad (\text{A-13})$$

$$\nabla_Q \left( \frac{1}{|\vec{r}-\vec{s}|} \right) = \begin{cases} \frac{1}{r^2} \sum_{n=0}^{\infty} \sum_{m=0}^n \left( \frac{s}{r} \right)^{n-1} S_n^m(\cos \theta_r) \frac{\partial S_n^m(\cos \theta_s)}{\partial \theta_s} \cos(m\varphi_r - m\varphi_s) \\ \frac{1}{\sin \theta_s r^2} \sum_{n=0}^{\infty} \sum_{m=0}^n \left( \frac{s}{r} \right)^{n-1} m S_n^m(\cos \theta_r) S_n^m(\cos \theta_s) \sin(m\varphi_r - m\varphi_s) \\ \frac{1}{r^2} \sum_{n=0}^{\infty} \sum_{m=0}^n \left( \frac{s}{r} \right)^{n-1} n S_n^m(\cos \theta_r) S_n^m(\cos \theta_s) \cos(m\varphi_r - m\varphi_s) \end{cases} \quad (\text{A-14})$$

The scalar potential  $\Omega$  of a magnetic dipole can be given in Schmidt quasi-normalized real spherical harmonics by setting

$$\Omega(r, \varphi_r, \theta_r) = \sum_{n=1}^N \sum_{m=0}^n (\mathcal{G}_n^m \cos m\varphi_r + \mathcal{H}_n^m \sin m\varphi_r) S_n^m(\cos \theta_r) \quad (\text{A-15})$$

$$g_n^m = \frac{\chi V}{4\pi r^2} \sum_{n=0}^{\infty} \sum_{m=0}^n \left(\frac{S}{r}\right)^{n-1} \left[ B_c^x \cos(m\varphi_s) \frac{\partial S_n^m(\cos \theta_s)}{\partial \theta_s} - \frac{m B_c^y}{\sin \theta_s} \sin(m\varphi_s) S_n^m(\cos \theta_s) + n B_c^z \cos(m\varphi_s) S_n^m(\cos \theta_s) \right]$$

$$h_n^m = \frac{\chi V}{4\pi r^2} \sum_{n=0}^{\infty} \sum_{m=0}^n \left(\frac{S}{r}\right)^{n-1} \left[ B_c^x \sin(m\varphi_s) \frac{\partial S_n^m(\cos \theta_s)}{\partial \theta_s} + \frac{m B_c^y}{\sin \theta_s} \cos(m\varphi_s) S_n^m(\cos \theta_s) + n B_c^z \sin(m\varphi_s) S_n^m(\cos \theta_s) \right]$$

Hence, the scalar potential  $\Omega$  of a magnetic dipole is expressed in spherical harmonic domain. Therefore, the SH coefficients regarding to one dipole can be directly calculated from its magnetic parameter which is  $\chi V$ . Consequently, magnetic parameters from inversion result can be converted to the SH coefficients so that the classical spherical harmonic analysis can be utilized in regional area.

## Appendix II

Krylov subspace methods represent one of the most important classes of iterative methods for solving large-scale linear systems  $Ax = b$  (e.g. [Saad 2003](#)). Krylov methods are based on projection of the residual  $v$  on to m-dimensional vector space, which is the Krylov subspace  $k_m(A, v)$ . A Krylov subspace solver starts with an initial guess  $x_0$  and generates a sequence of approximate solutions  $x_m$  in the Krylov subspace  $k_m(A, v)$ ,

$$x_m - x_0 \in k_m(A, v) = \text{span}\{v, Av, A^2v, \dots, A^{m-1}v\}, v = b - Ax_0 \quad (\text{A-16})$$

where  $x_0$  is an initial guess. Residuals of the iterative process satisfy the Petrov-Galerkin condition

$$b - Ax_m \perp \mathcal{L}_m \quad (\text{A-17})$$

where  $\mathcal{L}_m$  is an m-dimensional subspace related to the Krylov subspace  $k_m(A, v)$  or  $k_m(A^T, v)$ . As a result, the choices for  $\mathcal{L}_m$  lead to different families of Krylov subspace methods, which are  $\mathcal{L}_m = k_m(A, v)$ ,  $\mathcal{L}_m = Ak_m(A, v)$  and  $\mathcal{L}_m = k_m(A^T, v)$ .

Among various Krylov subspace iterative methods, the conjugate gradient algorithm (CG) is the oldest and most popular method that is a special case for  $\mathcal{L}_m = k_m(A, v)$ . However, the GG algorithm is only suitable for solving symmetric positive definite linear systems.

By contrast, the generalized minimal residual method (GMRES) and the biconjugate gradient method (BiCG) are two well-known generalized variants for solving nonsymmetric linear systems using  $\mathcal{L}_m = Ak_m(A, v)$  and  $\mathcal{L}_m = k_m(A^T, v)$  respectively. The GMRES method minimizes the residual by first constructing an orthonormal basis (dimension of m+1) using the Arnoldi process and then updating the solution by solving an (m+1) \* m least-squares problem. However, it becomes impractical when it converges slowly. Because the work per iteration increases as the number of iterations m increases. Alternatively, the BiCG method does not minimize the residual but uses the Lanczos biorthogonalization process to maintain the three-term recurrence so that the work per iteration does not change. In other words, BiCG has the potential to be faster than GMRES in total work. However, one is required to solve the original linear system  $Ax = b$  and a dual linear system  $A^T x^* = b^*$  at the

same time because BiCG uses both  $A$  and its transpose  $A^T$  simultaneously to update the new solution. Normally, we are not interested in the solution to  $A^T x^* = b^*$  and prefer to avoid the transpose of  $A$ . In this case, the biconjugate gradient stabilized method (BiCGSTAB) is a suitable approach, which is a transpose-free and more smoothly convergent variant of BiCG. Therefore, the BiCGSTAB method is computationally convenient for solving large-scale nonsymmetric linear systems (Table A-1).

Table A-1: Pseudo code for the biconjugate gradient stabilized method (BiCGSTAB)

---

Algorithm: BiCGSTAB

---

1.  $r_0 := b - Ax_0, (r_0, r_*) \neq 0$
2.  $p_0 := r_0$
3. For  $m = 0, 1 \dots$
4.  $\alpha_m := (r_m, r_*) / (Ap_m, r_*)$
5.  $s_m := r_m - \alpha_m Ap_m$
6.  $\omega_m := (As_m, s_m) / (As_m, As_m)$
7.  $x_{m+1} := x_m + \alpha_m p_m + \omega_m s_m$
8.  $r_{m+1} := s_m - \omega_m As_m$
9.  $\beta_m := \frac{\alpha_m (r_{m+1}, r_*)}{\omega_m (r_m, r_*)}$
10.  $p_{m+1} := r_{m+1} + \beta_m p_m - \beta_m \omega_m Ap_m$
11. Endfor

---

However, the BiCGSTAB method may suffer from low convergence rates and might stagnate or even break down due to the Lanczos biorthogonalization process (Sleijpen et al. 1994; Sleijpen and van der Vorst 1995; Ghai et al. 2019). Generally, this is closely related to the spectral properties of the linear system which is ill-conditioned. To have better performance of the iteration method, a preconditioner is usually needed to improve the efficiency of the algorithm (Benzi 2002). The aim of utilizing a preconditioner is to transform the original linear system into a different linear system that has a better convergence rate. The new system can be derived by multiplying the original linear system with a preconditioner matrix  $P$ ,

$$PAx = Pb \tag{A-18}$$

which has the same solution as the original system  $Ax = b$  and a smaller condition number than the original linear system (Chen 2005).

Generally, a preconditioner should be a good approximation of the original coefficient matrix  $A$  and the inverse must be easier to calculate. However, there is a trade-off between the cost of constructing and applying the preconditioner. In other words, we have to balance the amount of resources in terms

of runtime reduction in convergence and additional storage in memory. In practice, therefore, a sparse approximation of the original matrix is used for constructing the preconditioner. The incomplete-LU (ILU) and Cholesky factorization are two well-known sparse approximation preconditioners. The diagonal of the original coefficient matrix also can be an option because of its simplicity and readily availability.

In the context of magnetic inversion, the stagnation of the BiCGSTAB method did happen in the equatorial area. For this instance, a target area (-30°W, -15°E, 0°S, 15°N) in 0.25° resolution with 10° extension was selected to each edge to carry out the preconditioned BiCGSTAB method with 50 iterations.

As seen from the forward modeling, the coefficient matrix  $A$  is a dense matrix. ILU factorization for this dense matrix  $A$  is impractical because a meaningful sparsification for this matrix  $A$  is unknown. Nonetheless, three types of diagonal sparse approximation (diagonal, block tridiagonal and block pentadiagonal) of the dense matrix  $A$  were tested as a preconditioner. These positions in the matrix  $A$  are the main contributions of the magnetic sources due to the inverse proportionality to the cubed distance. However, only the diagonal preconditioner improved the convergence of the original stagnated problem (Table A-2). Yet, in terms of misfit, it is still not the ideal preconditioner for the inverse problems in this thesis.

Table A-2: Preconditioned BiCGSTAB

Preconditioner	identity	diagonal	tridiagonal	pentadiagonal
Runtime (s)	22.9	24.7	39.1	39.7
Relative residual	1	0.064	1	1

The transpose matrix  $A^T$  is not considered as a typical preconditioner for the iteration method. Nevertheless, the transpose matrix may improve the spectral properties of the original linear problem. When  $A$  is nonsymmetric, we can solve the equivalent symmetric positive definite (SPD) system, that is

$$A^T A x = A^T b \tag{A-19}$$

Although it is not an efficient way to solve the original linear system, it does prevent the stagnation of BiCGSTAB method in our case. Note that the new linear system is SPD so that the CG method is also applicable. Interestingly, the BiCGSTAB method still outperformed the CG method in terms of relative residual by one order of magnitude with maximum iteration number of 50 (Table A-3).

Therefore, the BiCGSTAB method was applied to the normal equation,  $A^T Ax = A^T b$ , to solve the non-constrained original inverse problem.

Table A-3: Comparison of BiCGSTAB and CG method in  $A^T Ax = A^T b$  system

	CG	BiCGSTAB
Runtime (s)	117.2	129.6
Relative residual	0.0011	0.00022

## References

- Aitken, A.R.A.; Betts, P. G.; Young, D. A.; Blankenship, D. D.; Roberts, J. L.; Siegert, M. J. (2016): The Australo-Antarctic Columbia to Gondwana transition. In *Gondwana Research* 29 (1), pp. 136–152. DOI: 10.1016/j.gr.2014.10.019.
- Aitken, Alan Robert Alexander; Young, D. A.; Ferraccioli, Fausto; Betts, Peter Graham; Greenbaum, Jamin S.; Richter, Thomas G. et al. (2014): The subglacial geology of Wilkes Land, East Antarctica. In *Geophysical Research Letters* 41 (7), pp. 2390–2400. DOI: 10.1002/2014GL059405.
- Allredge, L. R. (1981): Rectangular harmonic analysis applied to the geomagnetic field. In *Journal of Geophysical Research: Solid Earth* 86 (B4), pp. 3021–3026.
- Arkani-Hamed, J.; Strangway, D. W. (1985): Lateral variations of apparent magnetic susceptibility of lithosphere deduced from Magsat data. In *J. Geophys. Res.* 90 (B3), pp. 2655–2664.
- Arora, Kusumita; Cazenave, A.; Engdahl, Eric Robert; Kind, Rainer; Manglik, Ajay; Roy, Sukanta et al. (2011): *Encyclopedia of solid earth geophysics*: Springer Science & Business Media.
- Bankey, Viki; Cuevas, Alejandro; Daniels, David L.; Finn, Carol A.; Hernandez, Israel; Hill, Patricia L. et al. (2002): *Magnetic anomaly map of North America*. US Geological Survey.
- Baranov, Vladimir (1957): A new method for interpretation of aeromagnetic maps. Pseudo-gravimetric anomalies. In *Geophysics* 22 (2), pp. 359–382.
- Baykiev, Eldar; Ebbing, Jörg; Brönnner, Marco; Fabian, Karl (2016): Forward modeling magnetic fields of induced and remanent magnetization in the lithosphere using tesseroids. In *Computers & geosciences* 96, pp. 124–135.
- Benzi, Michele (2002): Preconditioning techniques for large linear systems. A survey. In *Journal of computational Physics* 182 (2), pp. 418–477.
- Bhattacharyya, B. K. (1965): Two-dimensional harmonic analysis as a tool for magnetic interpretation. In *Geophysics* 30 (5), pp. 829–857.
- Bhattacharyya, Bo Ko; Chan, K. C. (1977): Reduction of magnetic and gravity data on an arbitrary surface acquired in a region of high topographic relief. In *Geophysics* 42 (7), pp. 1411–1430.
- Blakely, Richard J. (1996): *Potential theory in gravity and magnetic applications*: Cambridge university press.
- Boger, Steven D. (2011): Antarctica — Before and after Gondwana. In *Gondwana Research* 19 (2), pp. 335–371. DOI: 10.1016/j.gr.2010.09.003.

- Bouysson, P. (2010): Geological Map of the World. Commission for the Geological Map of the World, scales: 1: 50,000,000 and 1: 25,000,000.
- Briaux, Anne; Patriat, Philippe; Tapponnier, Paul (1993): Updated interpretation of magnetic anomalies and seafloor spreading stages in the South China Sea. Implications for the Tertiary tectonics of Southeast Asia. In *Journal of Geophysical Research: Solid Earth* 98 (B4), pp. 6299–6328.
- Brooks, Robert L. (2013): The fundamentals of atomic and molecular physics: Springer.
- Brozena, J. M.; Mader, G. L.; Peters, M. F. (1989): Interferometric Global Positioning System. Three-dimensional positioning source for airborne gravimetry. In *Journal of Geophysical Research: Solid Earth* 94 (B9), pp. 12153–12162.
- Burton-Johnson, Alex; Dziadek, Ricarda; Martin, Carlos; Halpin, Jacqueline A.; Whitehouse, Pippa L.; Ebbing, Jörg et al. (2020): Antarctic geothermal heat flow. Future research directions [SCAR-SERCE White Paper]. SCAR-SERCE.
- Cain, J. C.; Sweeney, R. E. (1973): The POGO data. In *Journal of Atmospheric and Terrestrial Physics* 35 (6), pp. 1231–1247.
- Cain, Joseph C.; Wang, Zhigang; Kluth, Christopher; Schmitz, Dave Ray (1989): Derivation of a geomagnetic model to  $n = 63$ . In *Geophysical Journal International* 97 (3), pp. 431–441.
- Chen, Ke (2005): Matrix preconditioning techniques and applications: Cambridge university press (19).
- Clark, D. A. (1997): Magnetic petrophysics and magnetic petrology. Aids to geological interpretation of magnetic surveys. In *AGSO Journal of Australian Geology and Geophysics* 17, pp. 83–104.
- Corner, B.; Groenewald, P. B. (1991): Gondwana reunited. In *S. Afr. Trans. Nav. Antarkt.* 21 (2), pp. 173–183.
- Council for Geoscience (2019): Total Magnetic Field Intensity Map of the Republic of South Africa. Available online at <https://www.geoscience.org.za/index.php/2019-03-13-12-40-41/publications/284-geophysical-data>.
- Dampney, C. N. G. (1969): The equivalent source technique. In *Geophysics* 34 (1), pp. 39–53.
- Driscoll, James R.; Healy, Dennis M. (1994): Computing Fourier transforms and convolutions on the 2-sphere. In *Advances in applied mathematics* 15 (2), pp. 202–250.
- Dyment, J.; Arkani-Hamed, J. (1998): Contribution of lithospheric remanent magnetization to satellite magnetic anomalies over the world's oceans. In *Journal of Geophysical Research: Solid Earth* 103 (B7), pp. 15423–15441.

- E. Thébault; J. J. Schott; M. Manda (2006): Revised spherical cap harmonic analysis (R-SCHA). Validation and properties. In *Journal of Geophysical Research: Solid Earth* 111 (B1). DOI: 10.1029/2005JB003836.
- Ebbing, Jörg; Gernigon, Laurent; Pascal, Christophe; Olesen, Odleiv; Osmundsen, Per Terje (2009): A discussion of structural and thermal control of magnetic anomalies on the mid-Norwegian margin. In *Geophysical Prospecting* 57 (4), pp. 665–681. DOI: 10.1111/j.1365-2478.2009.00800.x.
- Ebbing, Jörg; Haas, Peter; Ferraccioli, Fausto; Pappa, Folker; Szwillus, Wolfgang; Bouman, Johannes (2018): Earth tectonics as seen by GOCE-Enhanced satellite gravity gradient imaging. In *Scientific reports* 8 (1), pp. 1–9.
- Enkin, Randolph J.; Hamilton, Tark S.; Morris, William A. (2020): The Henkel Petrophysical Plot. Mineralogy and Lithology from Physical Properties. In *Geochemistry, Geophysics, Geosystems* 21 (1), e2019GC008818.
- Ervin, C. Patrick (1976): Reduction to the magnetic pole using a fast Fourier series algorithm. In *Computers & geosciences* 2 (2), pp. 211–217.
- Ferraccioli, F.; Jones, P. C.; Curtis, M. L.; Leat, P. T. (2005): Subglacial imprints of early Gondwana break-up as identified from high resolution aerogeophysical data over western Dronning Maud Land, East Antarctica. In *Terra Nova* 17 (6), pp. 573–579. DOI: 10.1111/j.1365-3121.2005.00651.x.
- Ferraccioli, Fausto; Armadillo, Egidio; Jordan, Tom; Bozzo, Emanuele; Corr, Hugh (2009): Aeromagnetic exploration over the East Antarctic Ice Sheet. A new view of the Wilkes Subglacial Basin. In *Tectonophysics* 478 (1-2), pp. 62–77. DOI: 10.1016/j.tecto.2009.03.013.
- Ferraccioli, Fausto; Finn, Carol A.; Jordan, Tom A.; Bell, Robin E.; Anderson, Lester M.; Damaske, Detlef (2011): East Antarctic rifting triggers uplift of the Gamburtsev Mountains. In *Nature* 479 (7373), pp. 388–392. DOI: 10.1038/nature10566.
- Ferre, Eric C.; Friedman, Sarah A.; Martin-Hernandez, Fatima; Feinberg, Joshua M.; Till, Jessica L.; Ionov, Dmitri A.; Conder, James A. (2014): Eight good reasons why the uppermost mantle could be magnetic. In *Tectonophysics* 624, pp. 3–14.
- Finlay, Christopher C.; Olsen, Nils; Kotsiaros, Stavros; Gillet, Nicolas; Tøffner-Clausen, Lars (2016): Recent geomagnetic secular variation from Swarm and ground observatories as estimated in the CHAOS-6 geomagnetic field model. In *Earth Planet Sp* 68 (1), p. 112.
- Finn, Caro I.; Moore, David; Damaske, Detlef; Mackey, Timothy (1999): Aeromagnetic legacy of early Paleozoic subduction along the Pacific margin of Gondwana. In *Geology* 27 (12), pp. 1087–1090. DOI: 10.1130/0091-7613(1999)027<1087:ALOEPS>2.3.CO;2.

- Forsberg, Rene; Olesen, Arne V.; Ferraccioli, Fausto; Jordan, Tom A.; Matsuoka, Kenichi; Zakrajsek, Andres et al. (2018): Exploring the Recovery Lakes region and interior Dronning Maud Land, East Antarctica, with airborne gravity, magnetic and radar measurements. In *Geological Society, London, Special Publications* 461 (1), pp. 23–34. DOI: 10.1144/SP461.17.
- Franklin, R.; Milligan, P. R. (2010): Magnetic Anomaly Map of Australia, 5th edition, 1:5 million scale, 2010: Commonwealth of Australia (Geoscience Australia). Available online at <http://pid.geoscience.gov.au/dataset/ga/70282>, <https://researchdata.andis.org.au/magnetic-anomaly-map-scale-2010>, checked on 9/12/2019.
- Fregoso, Emilia; Gallardo, Luis A. (2009): Cross-gradients joint 3D inversion with applications to gravity and magnetic data. In *Geophysics* 74 (4), L31–L42.
- Freund, Roland W.; Golub, Gene H.; Nachtigal, Noël M. (1992): Iterative solution of linear systems. In *Acta numerica* 1, pp. 57–100.
- Fromm, Winfield E. (1952): The Magnetic Airborne Detector. In L. Marton (Ed.): *Advances in Electronics and Electron Physics*, vol. 4: Academic Press, pp. 257–299. Available online at <http://www.sciencedirect.com/science/article/pii/S006525390861080X>, checked on 9/11/2019.
- Fullea, J.; Afonso, Juan Carlos; Connolly, J. A. D.; Fernandez, Manel; García-Castellanos, Daniel; Zeyen, H. (2009): LitMod3D. An interactive 3-D software to model the thermal, compositional, density, seismological, and rheological structure of the lithosphere and sublithospheric upper mantle. In *Geochemistry, Geophysics, Geosystems* 10 (8).
- Gaina, Carmen; Werner, Stephanie C.; Saltus, Richard; Maus, Stefan (2011): Circum-Arctic mapping project. New magnetic and gravity anomaly maps of the Arctic. In *Geological Society, London, Memoirs* 35 (1), pp. 39–48.
- Ghai, Aditi; Lu, Cao; Jiao, Xiangmin (2019): A comparison of preconditioned Krylov subspace methods for large-scale nonsymmetric linear systems. In *Numerical Linear Algebra with Applications* 26 (1), e2215.
- Golub, Gene H.; van der Vorst, Henk A. (1997): Closer to the solutions. Iterative linear solvers. In *The state of the art in numerical analysis*, pp. 63–92.
- Golynsky, A.; Jacobs, J. (2001): Grenville–Age versus Pan–African Magnetic Anomaly Imprints in Western Dronning Maud Land, East Antarctica. In *The Journal of Geology* 109 (1), pp. 136–142. DOI: 10.1086/317964.

Golynsky, A. V.; Ferraccioli, Fausto; Hong, J. K.; Golynsky, D. A.; Frese, R. R. B. von; Young, D. A. et al. (2018): New magnetic anomaly map of the Antarctic. In *Geophysical Research Letters* 45 (13), pp. 6437–6449.

Golynsky, Alexander; Chiappini, Massimo; Damaske, Detlef; Ferraccioli, Fausto; Finn, Carol A.; Ishihara, Takemi et al. (2006): ADMAP—a digital magnetic anomaly map of the Antarctic. In : *Antarctica*: Springer, pp. 109–116.

Götze, H.-J.; Lahmeyer, Bernd (1988): Application of three-dimensional interactive modeling in gravity and magnetics. In *Geophysics* 53 (8), pp. 1096–1108.

Hahn, A.; Ahrendt, H.; Meyer, J.; Hufen, J.-H. (1984): A model of magnetic sources within the Earth's crust compatible with the field measured by the satellite Magsat. In *Geologisches Jahrbuch. Reihe A, Allgemeine und regionale Geologie BR Deutschland und Nachbargebiete, Tektonik, Stratigraphie, Paläontologie* (75), pp. 125–156.

Haines, G. V. (1985): Spherical cap harmonic analysis. In *Journal of Geophysical Research: Solid Earth* 90 (B3), pp. 2583–2591.

Hamoudi, Mohamed; Thébaud, E.; Lesur, Vincent; Manda, M. (2007): GeoForschungsZentrum Anomaly Magnetic MAp (GAMMA). A candidate model for the world digital magnetic anomaly map. In *Geochemistry, Geophysics, Geosystems* 8 (6).

Heiland, Carl August (1942): Geophysics in War. In *American Journal of Physics* 10 (3), pp. 127–134.

Hemant, K.; Maus, S. (2005): Geological modeling of the new CHAMP magnetic anomaly maps using a geographical information system technique. In *Journal of Geophysical Research: Solid Earth* 110 (B12).

Hemant, Kumar (2003): Modelling and interpretation of global lithospheric magnetic anomalies. Doctoral dissertation. Deutsches GeoForschungsZentrum GFZ Potsdam.

Hemant, Kumar; Thébaud, Erwan; Manda, Mioara; Ravat, Dhananjay; Maus, Stefan (2007): Magnetic anomaly map of the world. Merging satellite, airborne, marine and ground-based magnetic data sets. In *Earth and Planetary Science Letters* 260 (1-2), pp. 56–71.

Hinze, W. J.; Frese, R. R. B. von; Ravat, D. N. (1991): Mean magnetic contrasts between oceans and continents. In *Tectonophysics* 192 (1-2), pp. 117–127.

Idoko, Chijioke M.; Conder, James A.; Ferré, Eric C.; Filiberto, Justin (2019): The potential contribution to long wavelength magnetic anomalies from the lithospheric mantle. In *Physics of the Earth and Planetary Interiors* 292, pp. 21–28.

- Jokat, Wilfried; Boebel, Tobias; König, Matthias; Meyer, Uwe (2003): Timing and geometry of early Gondwana breakup. In *J. Geophys. Res.* 108 (B9), p. 91. DOI: 10.1029/2002JB001802.
- Kennicutt, Mahlon C.; Bromwich, David; Liggett, Daniela; Njåstad, Birgit; Peck, Lloyd; Rintoul, Stephen R. et al. (2019): Sustained Antarctic Research. A 21st Century Imperative. In *One Earth* 1 (1), pp. 95–113. DOI: 10.1016/j.oneear.2019.08.014.
- Korenaga, J.; Holbrook, W. S.; Kent, G. M.; Kelemen, P. B.; Detrick, R. S.; Larsen, H.-C. et al. (2000): Crustal structure of the southeast Greenland margin from joint refraction and reflection seismic tomography. In *Journal of Geophysical Research: Solid Earth* 105 (B9), pp. 21591–21614.
- Korhonen, Juha V.; Koistinen, Tapio; Elo, Seppo; Saavuori, H.; Kaariainen, J.; Nevanlinna, Heikki et al. (1999): Preliminary magnetic and gravity anomaly maps of the Fennoscandian shield 1: 10 000 000. In *SPECIAL PAPER-GEOLOGICAL SURVEY OF FINLAND*, pp. 173–180.
- Kotsiaros, Stavros; Olsen, Nils (2014): End-to-End simulation study of a full magnetic gradiometry mission. In *Geophysical Journal International* 196 (1), pp. 100–110.
- Kunagu, Praveen; Balasis, Georgios; Lesur, Vincent; Chandrasekhar, E.; Papadimitriou, C. (2013): Wavelet characterization of external magnetic sources as observed by CHAMP satellite. Evidence for unmodelled signals in geomagnetic field models. In *Geophysical Journal International* 192 (3), pp. 946–950.
- Langel, Robert; Ousley, Gilbert; Berbert, John; Murphy, James; Settle, Mark (1982): The MAGSAT mission. In *Geophysical Research Letters* 9 (4), pp. 243–245.
- Langel, Robert A. (1990): Global magnetic anomaly maps derived from POGO spacecraft data. In *Physics of the Earth and Planetary Interiors* 62 (3-4), pp. 208–230.
- Langel, Robert A.; Hinze, William J. (1998): The magnetic field of the Earth's lithosphere. The satellite perspective: Cambridge university press.
- Laske, Gabi; Masters, Guy; Ma, Zhitu; Pasyanos, Mike (2013): Update on CRUST1.0—A 1-degree global model of Earth's crust. In : *Geophys. Res. Abstr.*, vol. 15, p. 2658.
- Leopardi, Paul (2006): A partition of the unit sphere into regions of equal area and small diameter. In *Electronic Transactions on Numerical Analysis* 25 (12), pp. 309–327.
- Lesur, V.; Vervelidou, F. (2020): Retrieving lithospheric magnetization distribution from magnetic field models. In *Geophysical Journal International* 220 (2), pp. 981–995.

- Lesur, Vincent; Hamoudi, Mohamed; Choi, Yujin; Dyment, Jérôme; Thébaud, Erwan (2016): Building the second version of the world digital magnetic anomaly map (WDMAM). In *Earth, Planets and Space* 68 (1), p. 27.
- Lesur, Vincent; Jackson, Andrew (2000): Exact solutions for internally induced magnetization in a shell. In *Geophysical Journal International* 140 (2), pp. 453–459.
- Lesur, Vincent; Maus, Stefan (2006): A global lithospheric magnetic field model with reduced noise level in the Polar Regions. In *Geophysical Research Letters* 33 (13). DOI: 10.1029/2006GL025826.
- Li, Chun-Feng; Lu, Yu; Wang, Jian (2017): A global reference model of Curie-point depths based on EMAG2. In *Scientific reports* 7, p. 45129.
- Li, Yaoguo; Oldenburg, Douglas W. (2001): Stable reduction to the pole at the magnetic equator. In *Geophysics* 66 (2), pp. 571–578.
- Li, Yaoguo; Oldenburg, Douglas W. (2010): Rapid construction of equivalent sources using wavelets. In *Geophysics* 75 (3), L51–L59.
- Li, Z. X.; Evans, D.A.D.; Murphy, J. B. (2016): *Supercontinent Cycles Through Earth History*. 424 volumes: Geological Society of London.
- Lin, Chih-Jen (2007): Projected gradient methods for nonnegative matrix factorization. In *Neural computation* 19 (10), pp. 2756–2779.
- Lindeque, Ansa; Wit, Maarten J. de; Ryberg, Trond; Weber, Michael; Chevallier, Luc (2011): DEEP CRUSTAL PROFILE ACROSS THE SOUTHERN KAROO BASIN AND BEATTIE MAGNETIC ANOMALY, SOUTH AFRICA. AN INTEGRATED INTERPRETATION WITH TECTONIC IMPLICATIONS. In *South African Journal of Geology* 114 (3-4), pp. 265–292. DOI: 10.2113/gssajg.114.3-4.265.
- Maré, L. P.; Thomas, R. J. (1997): Palaeomagnetism and aeromagnetic modelling of the Mesoproterozoic Ntimbankulu pluton, Kwazulu-Natal, South Africa. Mushroom-shaped diapir? In *Journal of African Earth Sciences* 25 (4), pp. 519–537. DOI: 10.1016/s0899-5362(97)00107-3.
- Martos, Yasmina M.; Catalán, Manuel; Jordan, Tom A.; Golynsky, Alexander; Golynsky, Dmitry; Eagles, Graeme; Vaughan, David G. (2017): Heat flux distribution of Antarctica unveiled. In *Geophysical Research Letters* 44 (22), 11,417–11,426.
- Masterton, S. M.; Gubbins, D.; Müller, R. D.; Singh, K. H. (2013): Forward modelling of oceanic lithospheric magnetization. In *Geophysical Journal International* 192 (3), pp. 951–962.
- Maus, S. (2010): Magnetic field model MF7: CIRCLES, Colo.[Available at [www. geomag. us/models/MF7. html.](http://www.geomag.us/models/MF7.html)].

- Maus, S.; Haak, V. (2003): Magnetic field annihilators. Invisible magnetization at the magnetic equator. In *Geophysical Journal International* 155 (2), pp. 509–513.
- Maus, S.; Yin, F.; Lühr, H.; Manoj, C.; Rother, M.; Rauberg, J. et al. (2008): Resolution of direction of oceanic magnetic lineations by the sixth-generation lithospheric magnetic field model from CHAMP satellite magnetic measurements. In *Geochemistry, Geophysics, Geosystems* 9 (7).
- Maus, Stefan; Haak, Volker (2002): Is the long wavelength crustal magnetic field dominated by induced or by remanent magnetisation. In *J. Ind. Geophys. Union* 6 (1), pp. 1–5.
- Maus, Stefan; Lühr, Hermann; Balasis, Georgios; Rother, Martin; Mandea, Mioara (2005): Introducing POMME, the POtsdam Magnetic Model of the Earth. In : *Earth Observation with CHAMP*: Springer, Berlin, Heidelberg, pp. 293–298.
- Mayhew, M. A. (1982): Application of satellite magnetic anomaly data to Curie isotherm mapping. In *J. Geophys. Res.* 87 (B6), pp. 4846–4854.
- Mayhew, M. A.; Johnson, B. D.; Langel, R. A. (1980): An equivalent source model of the satellite-altitude magnetic anomaly field over Australia. In *Earth and Planetary Science Letters* 51 (1), pp. 189–198.
- McEnroe, Suzanne A.; Robinson, Peter; Church, Nathan; Purucker, Michael (2018): Magnetism at depth. A view from an ancient continental subduction and collision zone. In *Geochem. Geophys. Geosyst.* 19 (4), pp. 1123–1147.
- Mendonça, Carlos Alberto; Silva, João B. C. (1993): A stable truncated series approximation of the reduction-to-the-pole operator. In *Geophysics* 58 (8), pp. 1084–1090.
- Meyer, B.; Chulliat, A.; Saltus, R. (2017): Derivation and Error Analysis of the Earth Magnetic Anomaly Grid at 2 arc min Resolution Version 3 (EMAG2v3). In *Geochem. Geophys. Geosyst.* 18 (12), pp. 4522–4537. DOI: 10.1002/2017GC007280.
- Meyer, J.; Hufen, J.-H.; Siebert, M.; Hahn, A. (1983): Investigations of the internal geomagnetic field by means of a global model of the Earth's crust. In *Journal of Geophysics* 52 (1), pp. 71–84.
- Mieth, Matthias; Jacobs, Joachim; Ruppel, Antonia; Damaske, Detlef; Läufer, Andreas; Jokat, Wilfried (2014): New detailed aeromagnetic and geological data of eastern Dronning Maud Land. Implications for refining the tectonic and structural framework of Sør Rondane, East Antarctica. In *Precambrian Research* 245, pp. 174–185. DOI: 10.1016/j.precamres.2014.02.009.

Mieth, Matthias; Jokat, Wilfried (2014): New aeromagnetic view of the geological fabric of southern Dronning Maud Land and Coats Land, East Antarctica. In *Gondwana Research* 25 (1), pp. 358–367. DOI: 10.1016/j.gr.2013.04.003.

Milano, Maurizio; Fedi, Maurizio; Fairhead, J. Derek (2019): Joint analysis of the magnetic field and total gradient intensity in central Europe. In *Solid Earth* 10 (3), pp. 697–712. DOI: 10.5194/se-10-697-2019.

Milligan, P. R.; Franklin, R.; Ravat, D. (2004): A new generation magnetic anomaly grid database of Australia (MAGDA). In *Preview* 113, pp. 25–29.

Milligan, P. R.; Minty, B. R. S.; Luyendyk, T.; Lewis, A. (2001): Comparisons of total magnetic intensity grids, combined using GRIDMERGE, with two independent datasets. In *Geoscience Australia Record* 43.

Milligan, P. R.; Nakamura, A. (2015): Total Magnetic Intensity (TMI) Grid of Australia 2015 - sixth edition: Geoscience Australia. Available online at <http://dx.doi.org/10.4225/25/5625EAFE3F2A8>, <https://researchdata.anders.org.au/total-magnetic-intensity-sixth-edition>, checked on 9/12/2019.

Milligan, Peter; Minty, Brian; Richardson, Murray; Franklin, Ross (2009): The Australia-wide airborne geophysical survey-accurate continental magnetic coverage. In *ASEG Extended Abstracts 2009* (1), pp. 1–9.

Minty, Brian R. S.; Milligan, Peter R.; Luyendyk, Tony; Mackey, Timothy (2003): Merging airborne magnetic surveys into continental-scale compilations. In *Geophysics* 68 (3), pp. 988–995.

Mueller, Christian Olaf; Jokat, Wilfried (2019): The initial Gondwana break-up. A synthesis based on new potential field data of the Africa-Antarctica Corridor. In *Tectonophysics* 750, pp. 301–328. DOI: 10.1016/j.tecto.2018.11.008.

Müller, R. Dietmar; Sdrolias, Maria; Gaina, Carmen; Roest, Walter R. (2008): Age, spreading rates, and spreading asymmetry of the world's ocean crust. In *Geochemistry, Geophysics, Geosystems* 9 (4).

Müller, R. Dietmar; Zahirovic, Sabin; Williams, Simon E.; Cannon, John; Seton, Maria; Bower, Dan J. et al. (2019): A Global Plate Model Including Lithospheric Deformation Along Major Rifts and Orogens Since the Triassic. In *Tectonics* 38 (6), pp. 1884–1907. DOI: 10.1029/2018TC005462.

Murthy, S. Ananda. (2017): PROJECT. IGCP-628 THE GONDWANA MAP.

Nabighian, Misac N.; Grauch, V. J.S.; Hansen, R. O.; LaFehr, T. R.; Li, Y.; Peirce, Jonathan W. et al. (2005): The historical development of the magnetic method in exploration. In *Geophysics* 70 (6), 33ND-61ND.

- Nataf, Henri-Claude; Ricard, Yanick (1996): 3SMAC. An a priori tomographic model of the upper mantle based on geophysical modeling. In *Physics of the Earth and Planetary Interiors* 95 (1-2), pp. 101–122.
- Neubert, Torsten; Manda, M.; Hulot, G.; Frese, R. von; Primdahl, Fritz; Jørgensen, John Leif et al. (2001): Ørsted satellite captures high-precision geomagnetic field data. In *Eos, Transactions American Geophysical Union* 82 (7), pp. 81–88.
- Núñez Demarco, P.; Prezzi, C.; Sanchez Bettucci, L. (2021): Review of Curie point depth determination through different spectral methods applied to magnetic data. In *Geophysical Journal International* 224 (1), pp. 17–39.
- Olesen, O.; Brønner, M.; Ebbing, J.; Gellein, J.; Gernigon, L.; Koziel, J. et al. (2010): New aeromagnetic and gravity compilations from Norway and adjacent areas. Methods and applications. In : Geological Society, London, Petroleum Geology Conference series, vol. 7: Geological Society of London, pp. 559–586.
- Oliveira Jr, Vanderlei C.; Barbosa, Valéria C. F.; Uieda, Leonardo (2013): Polynomial equivalent layer. In *Geophysics* 78 (1), G1–G13.
- Olsen, Nils; Ravat, Dhananjay; Finlay, Christopher C.; Kother, Livia K. (2017): LCS-1. A high-resolution global model of the lithospheric magnetic field derived from CHAMP and Swarm satellite observations. In *Geophysical Journal International* 211 (3), pp. 1461–1477.
- Parker, Robert L.; Klitgord, Kim D. (1972): Magnetic upward continuation from an uneven track. In *Geophysics* 37 (4), pp. 662–668.
- Paterson, Norman R.; Reeves, Colin V. (1985): Applications of gravity and magnetic surveys. The state-of-the-art in 1985. In *Geophysics* 50 (12), pp. 2558–2594.
- Paxman, Guy J. G.; Jamieson, Stewart S. R.; Ferraccioli, Fausto; Jordan, Tom A.; Bentley, Michael J.; Ross, Neil et al. (2019): Subglacial Geology and Geomorphology of the Pensacola-Pole Basin, East Antarctica. In *Geochem. Geophys. Geosyst.* 20 (6), pp. 2786–2807. DOI: 10.1029/2018GC008126.
- Percival, P.J (2013): Digital files for the Index of airborne geophysical surveys. thirteenth edition. Geoscience Australia. Available online at <https://ecat.ga.gov.au/geonetwork/srv/eng/catalog.search#/metadata/74891>, updated on 12/25/2020, checked on 12/25/2020.
- Petkovic, P.; Milligan, P. (2002): Magnetic anomaly grid of the Australian region, 3.1.[Digital Dataset]. In *Geoscience Australia, Canberra ACT*.

Pilkington, Mark; Roest, Walter R. (1996): An assessment of long-wavelength magnetic anomalies over Canada. In *Canadian Journal of Earth Sciences* 33 (1), pp. 12–23.

Pollett, Alicia; Hasterok, Derrick; Raimondo, Tom; Halpin, Jacqueline A.; Hand, Martin; Bendall, Betina; McLaren, Sandra (2019): Heat Flow in Southern Australia and Connections With East Antarctica. In *Geochem. Geophys. Geosyst.* 20 (11), pp. 5352–5370. DOI: 10.1029/2019GC008418.

Purucker, M. E.; McEnroe, S. A. (Eds.) (2014): Estimating susceptibility and magnetization within the Earth's continental crust. *Petrophysical and Satellite approaches* (2014).

Purucker, Michael; Langlais, Benoit; Olsen, Nils; Hulot, Gauthier; Manda, Mioara (2002): The southern edge of cratonic North America. Evidence from new satellite magnetometer observations. In *Geophysical Research Letters* 29 (15), 56-1-56-4.

Purucker, Michael E.; Langel, Robert A.; Rajaram, Mita; Raymond, Carol (1998): Global magnetization models with a priori information. In *Journal of Geophysical Research: Solid Earth* 103 (B2), pp. 2563–2584.

Ravat, D.; Hildenbrand, T. G.; Roest, W. (2003): New way of processing near-surface magnetic data. The utility of the Comprehensive Model of the magnetic field. In *The Leading Edge* 22 (8), pp. 784–785.

Ravat, D.; Wang, B.; Wildermuth, E.; Taylor, Patrick T. (2002a): Gradients in the interpretation of satellite-altitude magnetic data. An example from central Africa. In *Journal of Geodynamics* 33 (1-2), pp. 131–142.

Ravat, D.; Whaler, K. A.; Pilkington, M.; Sabaka, T.; Purucker, M. (2002b): Compatibility of high-altitude aeromagnetic and satellite-altitude magnetic anomalies over Canada. In *Geophysics* 67 (2), pp. 546–554.

Ravat, Dhananjay; Korhonen, Juha (2010): A Preliminary, Full Spectrum, Magnetic Anomaly Grid of the United States with Improved Long Wavelengths for Studying Continental Dynamics. In : EGU General Assembly Conference Abstracts, vol. 12, p. 15500.

Reford, M. S.; Sumner, J. S. (1964): Aeromagnetism. In *Geophysics* 29 (4), pp. 482–516.

Riedel, S.; Jokat, W.; Steinhage, D. (2012): Mapping tectonic provinces with airborne gravity and radar data in Dronning Maud Land, East Antarctica. In *Geophysical Journal International* 189 (1), pp. 414–427. DOI: 10.1111/j.1365-246X.2012.05363.x.

Roberts, Paul H.; Glatzmaier, Gary A. (2000): Geodynamo theory and simulations. In *Reviews of modern physics* 72 (4), p. 1081.

S. Maus; U. Barckhausen; H. Berkenbosch; N. Bournas; J. Brozena; V. Childers et al. (2009): EMAG2. A 2-arc min resolution Earth Magnetic Anomaly Grid compiled from satellite, airborne, and marine magnetic measurements. In *Geochemistry, Geophysics, Geosystems* 10 (8). DOI: 10.1029/2009GC002471.

Saad, Yousef (2003): Iterative methods for sparse linear systems: SIAM.

Sabaka, Terence J.; Tøffner-Clausen, Lars; Olsen, Nils; Finlay, Christopher C. (2020): CM6. A comprehensive geomagnetic field model derived from both CHAMP and Swarm satellite observations. In *Earth, Planets and Space* 72 (1), pp. 1–24.

Scheiber-Enslin, Stephanie; Ebbing, Jörg; Webb, Susan J. (2014): An integrated geophysical study of the Beattie Magnetic Anomaly, South Africa. In *Tectonophysics* 636, pp. 228–243. DOI: 10.1016/j.tecto.2014.08.021.

Searle, R. C.; Keeton, J. A.; Owens, R. B.; White, R. S.; Mecklenburgh, R.; Parsons, B.; Lee, S. M. (1998): The Reykjanes Ridge. Structure and tectonics of a hot-spot-influenced, slow-spreading ridge, from multibeam bathymetry, gravity and magnetic investigations. In *Earth and Planetary Science Letters* 160 (3-4), pp. 463–478.

Silva, João B. C. (1986): Reduction to the pole as an inverse problem and its application to low-latitude anomalies. In *Geophysics* 51 (2), pp. 369–382.

Simons, Frederik J.; Dahlen, F. A. (2006): Spherical Slepian functions and the polar gap in geodesy. In *Geophysical Journal International* 166 (3), pp. 1039–1061.

Simons, Frederik J.; Dahlen, F. A.; Wicczorek, Mark A. (2006): Spatiospectral concentration on a sphere. In *SIAM review* 48 (3), pp. 504–536.

Sleijpen, Gerard L. G.; Fokkema, Diederik R. (1993): BiCGstab (ell) for linear equations involving unsymmetric matrices with complex spectrum. In *Electronic Transactions on Numerical Analysis* 1, pp. 11–32.

Sleijpen, Gerard L. G.; van der Vorst, Henk A. (1995): Maintaining convergence properties of BiCGstab methods in finite precision arithmetic. In *Numerical algorithms* 10 (2), pp. 203–223.

Sleijpen, Gerard L. G.; van der Vorst, Henk A.; Fokkema, Diederik R. (1994): BiCGstab (l) and other hybrid Bi-CG methods. In *Numerical algorithms* 7 (1), pp. 75–109.

Sneeuw, N.; van Gelderen, M. (1997): The polar gap. In : Geodetic boundary value problems in view of the one centimeter geoid: Springer, pp. 559–568.

- Stål, Tobias; Reading, Anya M.; Halpin, Jacqueline A.; Whittaker, Joanne M. (2019): A Multivariate Approach for Mapping Lithospheric Domain Boundaries in East Antarctica. In *Geophys. Res. Lett.* 46 (17-18), pp. 10404–10416. DOI: 10.1029/2019GL083453.
- Stettler, E. H.; Fourie, C. J.S.; Cole, P. (2000): Total Magnetic Field Intensity Map of the Republic of South Africa: Council for Geoscience (South Africa).
- Stockmann, Reto; Christiansen, Freddy; Olsen, Nils; Jackson, Andrew (2015): POGO satellite orbit corrections. An opportunity to improve the quality of the geomagnetic field measurements? In *Earth, Planets and Space* 67 (1), pp. 1–10.
- Swanson-Hysell, N. L.; Kilian, T. M.; Hanson, R. E. (2015): A new grand mean palaeomagnetic pole for the 1.11 Ga Umkondo large igneous province with implications for palaeogeography and the geomagnetic field. In *Geophysical Journal International* 203 (3), pp. 2237–2247. DOI: 10.1093/gji/ggv402.
- Szwillus, Wolfgang; Afonso, Juan Carlos; Ebbing, Jörg; Mooney, Walter D. (2019): Global crustal thickness and velocity structure from geostatistical analysis of seismic data. In *Journal of Geophysical Research: Solid Earth* 124 (2), pp. 1626–1652.
- Szwillus, Wolfgang; Ebbing, Jörg; Holzrichter, Nils (2016): Importance of far-field topographic and isostatic corrections for regional density modelling. In *Geophysical Journal International* 207 (1), pp. 274–287.
- Tarlowski, C.; McEwin, A. J.; Reeves, C. V.; Barton, C. E. (1996): Dewarping the composite aeromagnetic anomaly map of Australia using control traverses and base stations. In *Geophysics* 61 (3), pp. 696–705.
- Tarlowski, C.; Simonis, F.; Whitaker, A.; Milligan, P. (1992): The magnetic anomaly map of Australia. In *Exploration Geophysics* 23 (1-2), pp. 339–341.
- Thébault, E.; Vervelidou, Foteini (2015): A statistical spatial power spectrum of the Earth's lithospheric magnetic field. In *Geophysical Journal International* 201 (2), pp. 605–620.
- Thébault, Erwan; Finlay, Christopher C.; Beggan, Ciarán D.; Alken, Patrick; Aubert, Julien; Barrois, Olivier et al. (2015): International geomagnetic reference field. The 12th generation. In *Earth, Planets and Space* 67 (1), p. 79.
- Thébault, Erwan; Purucker, Michael; Whaler, Kathryn A.; Langlais, Benoit; Sabaka, Terence J. (2010): The magnetic field of the Earth's lithosphere. In *Space Science Reviews* 155 (1-4), pp. 95–127.

Thébault, Erwan; Vigneron, Pierre; Langlais, Benoit; Hulot, Gauthier (2016): A Swarm lithospheric magnetic field model to SH degree 80. In *Earth Planet Sp* 68 (1), p. 6339. DOI: 10.1186/s40623-016-0510-5.

Veevers, J. J. (2009): Palinspastic (pre-rift and -drift) fit of India and conjugate Antarctica and geological connections across the suture. In *Gondwana Research* 16 (1), pp. 90–108. DOI: 10.1016/j.gr.2009.02.007.

Vervelidou, Foteini; Lesur, Vincent (2018): Unveiling Earth's hidden magnetization. In *Geophysical Research Letters* 45 (22), 12,283–12,292.

Vervelidou, Foteini; Thébault, Erwan (2015): Global maps of the magnetic thickness and magnetization of the Earth's lithosphere. In *Earth, Planets and Space* 67 (1), p. 173.

Webb, Susan Jane (2009): The use of potential field and seismological data to analyze the structure of the lithosphere beneath southern Africa.

Weckmann, U.; Jung, A.; Branch, T.; Ritter, O. (2007): Comparison of electrical conductivity structures and 2D magnetic modelling along two profiles crossing the Beattie Magnetic Anomaly, South Africa. In *South African Journal of Geology* 110 (2-3), pp. 449–464. DOI: 10.2113/gssajg.110.2-3.449.

Waler, K. A.; Langel, R. A. (1996): Minimal crustal magnetizations from satellite data. In *Physics of the Earth and Planetary Interiors* 98 (3-4), pp. 303–319.

Wieczorek, Mark A.; Meschede, Matthias (2018): Shtools. Tools for working with spherical harmonics. In *Geochemistry, Geophysics, Geosystems* 19 (8), pp. 2574–2592.